1-1-2005

Determination of thickness and quality of refractory linings in industrial furnaces using acousto ultrasonic echo

Gary Walters
Ryerson University

DETERMINATION OF THICKNESS AND QUALITY OF REFRACTORY LININGS IN INDUSTRIAL FURNACES USING ACOUSTO ULTRASONIC-ECHO

By

Gary Walters

B.Eng. Civil Engineering, Ryerson University, Toronto, 2002

A thesis

presented to Ryerson University

in partial fulfillment of the

requirement for the degree of

Master of Applied Science

(Civil Engineering)

Toronto, Ontario, Canada, 2005

AUTHOR'S DECLARATION

I hereby declare that I am the sole author of this thesis.

I authorize Ryerson University to lend this thesis to other institutes or individuals for the purpose of scholarly research.

Author's signature ___ Date September 28, 2005

I further authorize Ryerson University to reproduce this thesis by photocopying or by other means, in total or in part, at a request of other institutions or individuals for the purpose of scholarly research.

Author's signature ___ Date September 28, 2005

BORROWER'S PAGE

Borrowers undertake to give proper credit for any use made of the thesis. Ryerson University requires the signatures of all persons using or photocopying this thesis. Please sign below and give address and date.

Name	Signature of Borrower	Address	Date
			Apr. 2008.

DETERMINATION OF THICKNESS AND QUALITY OF REFRACTORY LININGS IN INDUSTRIAL FURNACES USING ACOUSTO ULTRASONIC-ECHO

Gary Walters

Master of Applied Science, Department of Civil Engineering

RYERSON UNIVERSITY, Canada, 2005

ABSTRACT

Refractory linings in metallurgical furnaces undergo deterioration and wearing with time. The deterioration is caused mainly by thermo-mechanical mechanisms leading to cracks, chemical degradation and loss of heat transfer capability. Any sudden failure of the lining is dangerous and could affect the structural integrity of the furnace, leading to production loss and costly refurbishment.

Non-destructive Testing (NDT) and monitoring of the refractory lining would lead to better safety, longer use of the vessel, production optimization, controlled maintenance and increased production. Thickness measurements and monitoring of the refractory lining in operating furnaces is possible using Acousto Ultrasonic-Echo (AU-E) technique. This technique uses stress waves of both acoustic and ultrasonic ranges in order to determine thickness and integrity.

This thesis presents the details of AU-E technique in addition to laboratory measurements to determine parameters leading to the in-situ measurements. Finally, three case studies are presented to substantiate the theoretical and laboratory measurements.

PREFACE

This thesis is mainly based on the work done from January 2003 - to - June 2005, at the Division of Structural Engineering, Department of Civil Engineering at Ryerson University, Canada. The thesis is a study of the feasibility of using acousto ultrasonic-echo as a means for evaluating industrial furnace linings.

I would like to express my sincere gratitude and appreciation to my thesis advisors, Dr. Mohamed Lachemi and Dr. Afshin Sadri, for their guidance, support and patience during the development of this thesis. At every turn, they enthusiastically supported me and were a key role in the success of my completion of this thesis.

Furthermore, I would to thank the following individuals for their input and expertise in their respected areas: Harvey Pellegrini, Bill Lambros, Dr. Medhat Shehata, Dr. Lamya Amleh, Syed Ali Kashif and Dalton Fowler. I would also like to thank Andec International Services for the donation of equipment and expertise needed for this project and Materials and Manufacturing Ontario for the funding for this project.

Finally, special gratitude goes to my family.

DEDICATION

To those who guide me on my path

TABLE OF CONTENTS

LIST OF TABLES

LIST OF FIGURES

NOTATION AND ABBREVIATIONS

Bi = Biot Number

C_B = P-wave speed for build-up (m/s)

C_M = Measured wave speed (m/s)

C_P = Compressive or Primary (P) wave speed (m/s)

c_p = Specific heat (J/kg•K)

C_{P1} = Incident P-wave speed (m/s)

C_{P2} = Reflected/Refracted P-wave speed (m/s)

C_R = Rayleigh wave speed (m/s)

C_S = Shear or Secondary (S) wave speed (m/s)

C_{S1} = Reflected S-wave speed (m/s)

C_{S2} = Refracted S-wave speed (m/s)

C_{TH} = Theoretical wave speed (m/s)

D = Diameter (m)

D/B = Depth to width ratio for rectangular cross-section

E_{DYN} = Dynamic modulus of elasticity (GPA)

E_o = Modulus of elasticity at room temperature (GPA)

E_x = Average modulus of elasticity with respect to temperature (GPA)

err = Acceptable difference between true and sample mean

F = Fourier number

f = Frequency (Hz)

f_{MAX} = Maximum useful frequency (Hz)

f_B = Frequency contribution of build-up (Hz)

f_R = Frequency contribution of refractory (Hz)

f_T = Total frequency (Hz)

G_{DYN} = Dynamic shear modulus (GPA)

h = Heat transfer coefficient (W/m^2•K)

i_1 = Source current in Amps

i_2 = Induced current in Amps

i_P = Incident angel of P-wave

k = Thermal conductivity (K•W/m)

L = Length or thickness (m)

N = Number of analog data samples

N_1 = Input number of turns in the transformer coil

N_2 = Output number of turns in the transformer coil

n = number of samples

q" = Heat flux (W/m^2)

R_P = Reflected angel of P-wave

r_P = Refracted angel of P-wave

R_S = Reflection angel of S-wave

r_P = Refracted angel of S-wave

SR = Sampling rate (Hz)

T = Thickness (m)

T_1 = Initial boundary temperature (°C)

T_2 = Final boundary temperature (°C)

T_B = Thickness of build-up (m)

T_c/T_i = ratio of boundary temperatures in a thermal gradient

t = time (seconds)

t_C = contact time (seconds)

x_1 = Depth of initial boundary temperature (m)

x_2 = Depth of final boundary temperature (m)

Z = Acoustic impedance

$z_{\alpha/2}$ = Confidence interval for normally distributed data

α = Dimensionless temperature correction for materials

α_B = Temperature correction for build-up material

α_R = Temperature correction for refractory material

α_{TH} = Thermal diffusivity (m^2/s)

β = Shape factor

Δf = Frequency resolution (Hz)

ΔT = Temperature gradient

Δt = Time interval between samples (μs)

Φ = Flux

λ = wavelength (m)

υ_{DYN} = Dynamic Poisson's ratio

ρ = Density (kg/m^3)

σ = standard deviation of the mean

σ_R = Magnitude of reflected wave

σ_i = Magnitude of incident wave

σ_T = Magnitude of transmitted wave

Chapter 1
Introduction

1.1 Introduction

Refractory linings in metallurgical furnaces undergo deterioration and wearing with time and are often the governing factor in the service life of the vessel. Deterioration is caused mainly by thermo-mechanical stresses and chemical attack resulting in loss of heat transfer capability, cracking and loss of load bearing ability. Deterioration begins immediately after start up and progresses continuously throughout the life of the furnace. Failure of the lining is dangerous and refurbishment of any sudden failure is expensive in terms of production losses, materials and manpower.

Many industrial processes require a heating stage in the manufacturing of the final product. Depending on the process, temperatures can reach as high as 1500°C or higher in some cases. To resist these extreme temperatures refractory materials are used to insulate the chamber from the outside environment. There are many different types of materials that can resist high temperatures but the focus of the research done here is on materials, which include refractory ceramics (refractory bricks) and refractory cements (castables).

Non-destructive Testing (NDT) is best suited for monitoring the refractory lining for two main reasons. NDT can be done in some cases while the furnace is still in operation without an interruption to the production schedule. NDT can be performed from the outside of the vessel allowing operator safety during the evaluation. Traditional methods of evaluating furnaces, such as coring and visual inspections may cause damage to the structure, are inaccurate and testes are not repeatable, which can be limited and hazardous. Ultimately, NDT of furnace vessels would lead to increased safety in the plant environment by avoiding hazards associated with failure of the lining such as the release of dangerous gasses or spillage of molten metal. NDT evaluation would also lead to longer use of the vessel and production optimization.

A summary of some NDT methods used for evaluating civil engineering structures is shown in Figure 1.1. The figure identifies different techniques and highlights the information gathered from each method.

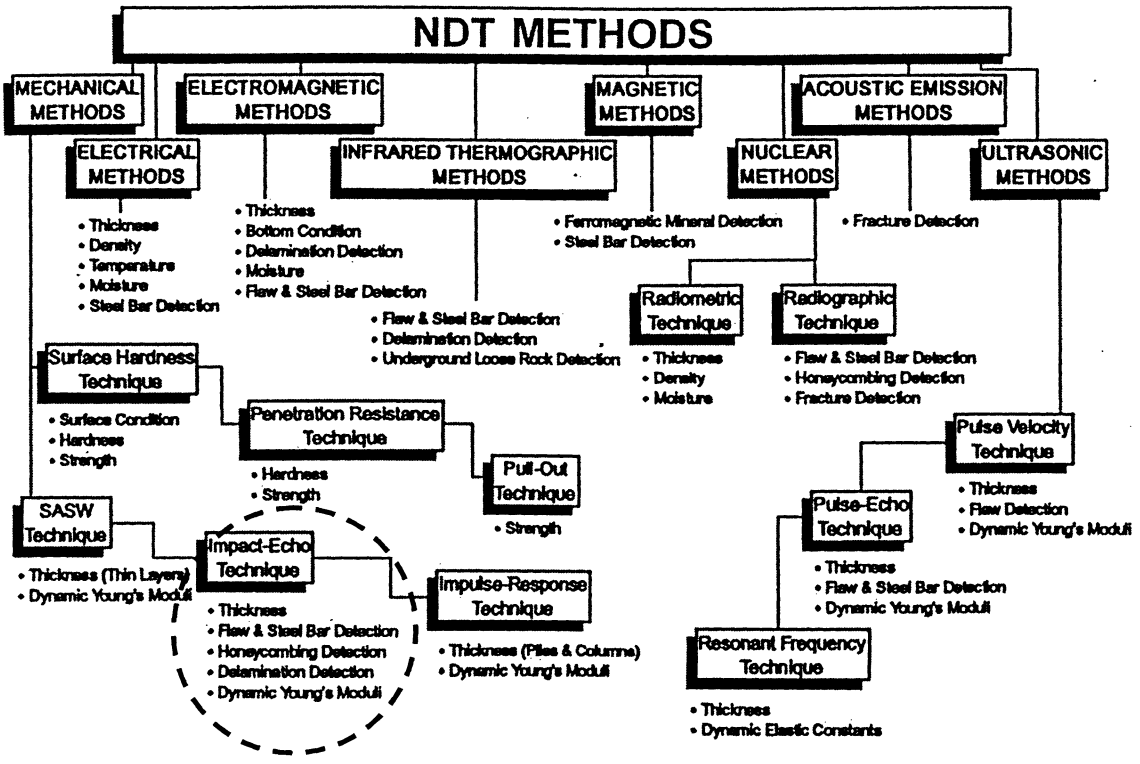

Figure 1.1: Summary of NDT Techniques (Sadri, 1996)

The methods emphasised in this discussion focus on the testing of materials in furnace applications only, although many other NDT techniques exist. Understanding the information provided by the various techniques for evaluating furnace linings and their limitations is essential when choosing an NDT method. Monitoring of the refractory lining in operating furnaces is possible using the Acousto Ultrasonic-Echo (AU-E) technique, which is a modification to the impact echo technique highlighted in Figure 1.1. The differences between the impact echo technique to the AU-E technique is that AU-E uses a broader range of frequencies and accounts for the temperature changes within the material. The understanding that these modifications were necessary was first realized by ANDEC International Services in 1997.

The following sections describe NDT techniques used for evaluating the linings of industrial furnaces along with the limitations of each method. This will emphasize the reasons for AU-E technique as being the most feasible method for evaluating online industrial furnaces.

1.2 NDT Techniques For Industrial Furnaces

As outlined in the Figure 1.1, there are many types of NDT techniques. This section will briefly outline the techniques used for evaluating industrial furnace linings along with the disadvantages of each.

1.2.1 Infrared Thermographic Techniques

Thermographic or infrared imaging involves displaying differences in heat via colour contouring on a picture or monitor screen and is useful for detecting near surface and shallow delaminations. The technique is based on the principle that subsurface anomalies in a material affect heat flow through that material (Malhotra and Carnio, 1991). These changes in heat flow, cause localized differences in surface temperatures. For furnace linings in general, thin areas or cracks propagating perpendicular to the testing surface, appear as hot spots by the thermal imaging and is illustrated by Figure 1.2.

Various types of materials have different insulating abilities or thermal conductivities. In addition, different types of material defects have different thermal conductivity values. Sound material should have the least resistance to conduction of heat. Therefore, where cracks within the lining run parallel to the testing surface or there is separation of the lining layers, these areas will show up as cold spots from the thermographic analysis.

Differentiation between the two scenarios for furnace lining evaluation is difficult whereby a surface may produces comparatively cooler areas due to a large thickness or may produces comparatively cooler areas due to separation within the lining.

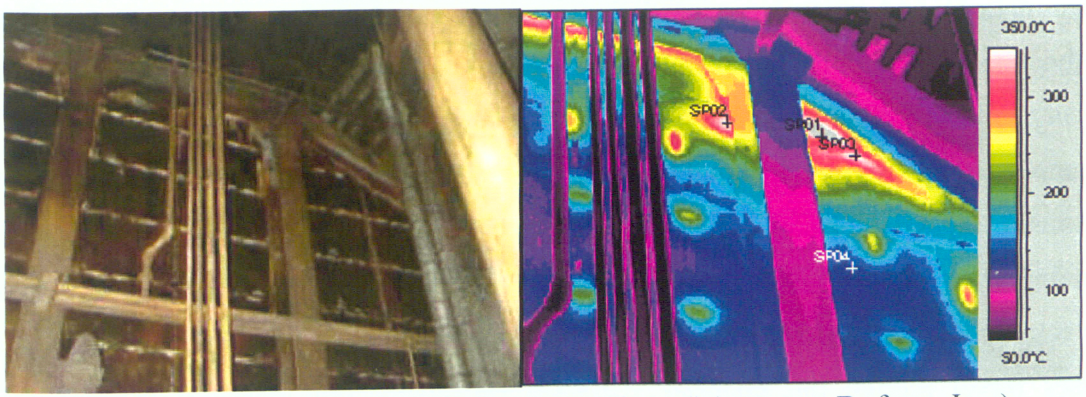

Figure 1.2: Furnace shell Showing "Hot Spots" (courtesy Dofasco Inc.)

1.2.2 Thermal Flux Technique

Refractory lining thickness can be calculated using the standard one-dimensional heat transfer relationship (Incropera and Dewitt, 1990):

$$q'' = k\frac{\Delta T}{L} \tag{1.1}$$

where; q'' is the heat flux (W/m^2), k is the thermal conductivity ($K^{\bullet}W/m$), ΔT is the temperature gradient and L is the length or thickness of the lining. The temperature gradient is determined over a small area using embedded thermocouples to establish a generalized heat flux value. The heat flux along with other known parameters is then applied to other areas for the furnace for establishing thickness measurements.

Heat flux techniques have been the conventional method for estimating refractory thickness in furnace applications. However, the heat flux measurements could result in inaccurate thickness estimations. The factor contributing the most to this error is what is known as contact resistance. Typically, refractory linings have cracks or joints along the length of the wall section. These discontinuities create a sharp change in the temperature gradient introducing large errors when using Equation 1.1 (Incropera and Dewitt, 1990). Furthermore, the equation is only valid for steady state conduction, which is not always the case in furnace applications. The shells of the furnace are water-cooled or air-cooled introducing what is known as a convection effect. This fluid interaction produces further changes in the temperature gradient and increases the possibility of errors.

1.2.3 Radar Methods

Short-pulse radar is a useful and rapid NDT technique mainly for detection of delaminations and other types of defects in concrete and masonry structures. Radar methods use waves in the electromagnetic spectrum in the range of 20 MHz - 1GHz. The frequency is critical when dealing with different types of materials and structures. In principle, the microwave strikes an interface between two materials of different dielectric constants and reflects some of the energy back to the source, while transmitting the remaining energy. The transmitted energy reaches a second interface of different dielectric constants and reflects energy through the material back to the source. As the pulses travel though the material, different reflections will occur at interfaces that

represent different dielectric properties. Each reflected electromagnetic pulse arrives back at the receiving antenna at a different time that is governed by the depth of the corresponding reflecting interface and the dielectric constant of the material (Malholtra and Carnio, 1991). This information can easily be displayed graphically showing depth of the interfaces at a specific location.

The limitation of this method for evaluating furnace linings is the steel shell encasing the refractory material. The metal of the shell will completely reflect the beam energy back to the source and will not penetrate into the successive layers of the lining. This technique does have potential for evaluating the furnace lining during a shutdown from the interior of the furnace. However, this can only be performed on non-metallic production processes.

1.2.4 Magnetic Methods

The technique uses the fundamental relationship between magnetic fields and electrical currents. A wire coiled around a metal core with electrical current passing through the wire will produce a magnetic field. The opposite will occur by placing a wire coil in the proximity of a magnetic field to generate an electrical current. A common application of this principle is a transformer and a typical set-up is shown in Figure 1.3. The magnetic field or electrical output is a function of the core size and number of coils.

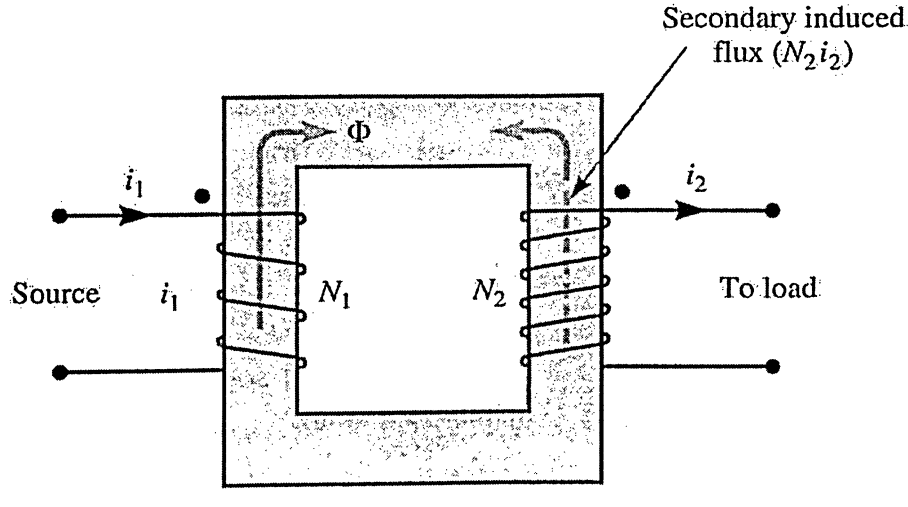

Figure 1.3: Simple Transformer Set-up (Boctor et al, 1997)

By changing the core size, the output current can be measured and is the basic principle behind a covermeter. Based on how much current change is detected, quantitative measurements can be obtained as to the amount of metal present or the distance to the metal object (Libby, 1971). This technique can evaluate a furnace lining during a shutdown from the interior of the furnace and like the radar methods can only be performed on non-metallic production processes. For this application, similar to short-pulse radar, the furnace should be off-line and cold

1.2.5 Stress Wave Techniques

The stress wave propagation techniques are a series of NDT methods utilizing the stress wave propagation principles to evaluate various structures. Amongst stress wave propagation techniques the most common ones are ultrasonic pulse-echo, ultrasonic through transmission (or pulse-velocity), impulse response and impact echo. The basic set-up has a transmitter that generates a stress wave, a receiver that detects or picks up the signal and a computer that can translate the signals into usable information.

The ultrasonic pulse-velocity technique is characterised by the magnitude of the frequencies used in the testing stage. All frequencies above 20 kHz can be considered as an ultrasonic frequency, or above the audible sound range. In practice, ultrasonic instrument functions for refractory material are in the range of 20 kHz to 250 kHz for non-destructive testing purposes (Sadri, 1996). The stress wave is generated using a piezoelectric transducer. The travel time through the specimen is affected based on the material properties such as elasticity and density. A complex array of transmitters and receivers are used to generate areas of high and low wave velocities (tomography). The areas of low velocity could be interpreted as anomalous areas. A major drawback of the technique is that the transmitter-receiver must be placed at opposite faces of the structure. For furnace applications, the opposite face or inside face of the lining is inaccessible. In addition, couplant is needed which is typically not suitable for the high temperatures involved in evaluating furnaces.

Ultrasonic Pulse-echo is usually a fixed frequency, narrowband generator-receiving system. The principle stress wave monitored in this technique is the P-wave, which propagates into the object and undergoes multiple reflections between the test

surface and the internal defects or the opposite boundary of the test object. By monitoring the vertical surface displacements caused by the arrival of the multiple P-wave reflections (echoes), the depth of the reflecting surface can be determined (Sadri, 1996). Drawbacks include the need of couplant to aid in transmitting the high frequency signals and the narrow bandwidth restricts the technique to evaluating a narrow window or thickness region

The impact echo technique utilizes a broadband receiving system and uses acoustic and ultrasonic frequencies simultaneously. The principle stress wave monitored in this technique is the again the P-wave. The signals are analysed in both time and frequency domains and is capable of detecting multiple sized flaws at various depths. The signal is generated by an impact using a spherical impactor of known diameter. The main drawback of the technique is that high frequencies are difficult to produce causing shallow delaminations to go undetected which varies depending on material properties.

The impulse response technique is a derivative of the impact echo technique whereby the impact energy is extracted form the response of the structure. This normalizes the response from impact to impact. The resonant frequencies are utilized for the evaluation of the structure like the impact echo technique however, with the impact echo technique the amplitude of the response is ignored from reading to reading.

Applications of stress wave propagation can be divided into two main categories. Material quality can be comparatively measured (i.e. wave speeds, attenuation, etc.) or the mechanical properties of a material can be determined using mathematical relationships (i.e. dynamic modulus of elasticity). A more extensive explanation of stress waves and the AU-E technique is outlined in Chapter 2.

1.3 Properties of Refractory Materials

A refractory or refractoriness describes any material that can withstand high temperatures or a corrosive environment, while the properties of the material remaining somewhat stable under these conditions. Some refractory applications include lining; blast furnaces, reheat furnaces, ladles, rotary kilns and chemical reactors. For each application, the refractory is different in order to accommodate the various working stresses the material endures while in service. For example, a blast furnace refractory lining must resist

corrosive gasses as well as high temperatures compared to an electrical arc furnace that has a less reactive gaseous environment. The refractory linings in rotary kilns are subjected to a high degree of cyclic loading which calls for a material with a low elasticity in order to better cope with the changing stresses.

Some problems encountered from damaged refractories have resulted in the release of molten metal into the work environment creating an extreme hazard. Other safety risks include roof areas especially after the furnace has cooled and contracted. Roof linings remain a critical area for refractory evaluation due to the tensile stresses at these locations. Like all coarse grain materials, refractories are weaker in tension compared to their compressive strength. Other high-risk areas include reaction zones and accretion locations in the furnace.

Refractories can be classified in different ways. They can be classed by property such as high strength, high melting point or low thermal conductivity. They can also be classified according to the manufacturing methods such as pressing or firing temperature. Finally, refractories can be classified by mineralogical composition. This is the most convenient way to identify the refractory types and is shown in the Figure 1.4.

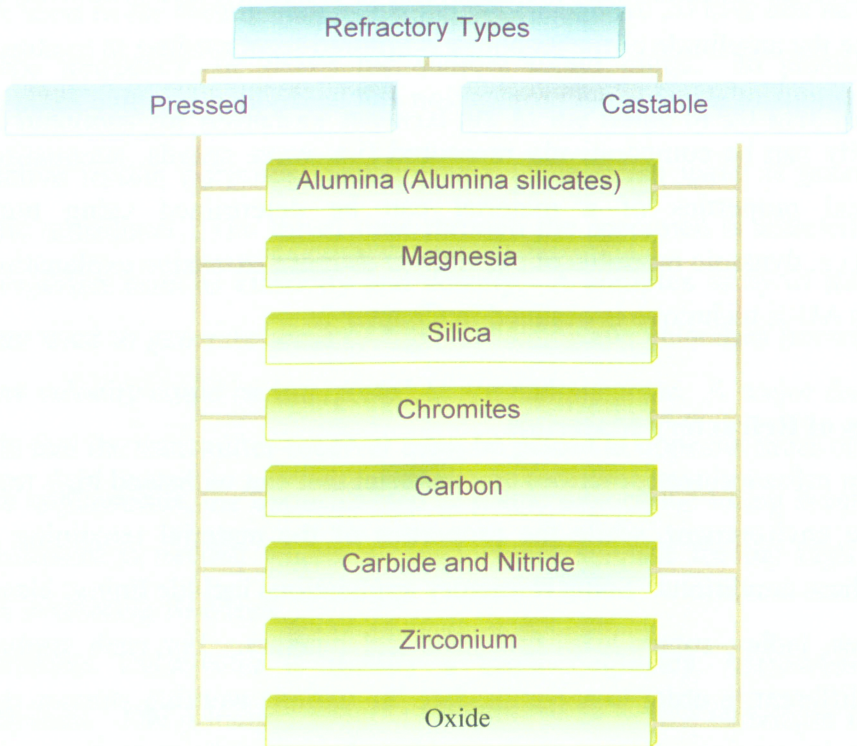

Figure 1.4: Refractory Types

Refractory materials can be divided into two main categories namely refractory alloys and refractory ceramics. Refractory alloys share similar properties with refractory ceramics such as low chemical reactivity and high heat resistance. Furnace linings are made with refractory ceramics, which are comparatively lower in cost and generally have better insulating properties than refractory metals. Refractory ceramic subcategories are manufactured bricks or cast in place. The manufactured bricks are cast and pressed into specific shapes and are of higher quality than the cast in place materials. The advantage of cast in place refractories is applications where molten metal is susceptible to penetrating spaces between individual manufactured bricks. Complex geometries call for cast in place refractories to be used for applications such as rotary kilns. The manufactured bricks use pressing techniques and far less water or plasticizer, which accounts for the increase in quality.

All refractories must be fired or sintered after the moulds or forms are removed. The firing procedure is a very important step of the manufacturing process and produces the desired properties of the refractory for service conditions. During the firing stage of sintering, different physiochemical processes are undergone by the refractory through the heating process. Depending on the refractory type, different heating rates need to be considered as well as soak time at specific temperatures. For example, a temperature may be reached where a phase change occurs in one of the material constituents forming a new microstructure. The temperature may be lowered to allow crystallization to occur and then further heating may then continue. The firing stage of the production process is an area of an intense research in the refractory industry. The firing temperature and soak duration can alter the properties of a refractory material and can add to the variability between samples. The dependence of the modulus of elasticity is plotted against firing temperatures in Figure 1.5.

As shown in Figures 1.5, an increase in firing temperature produces an increase in modulus of elasticity for this material. A similar trend is observed with the modulus of rupture of a material (Cutard et al., 2004).

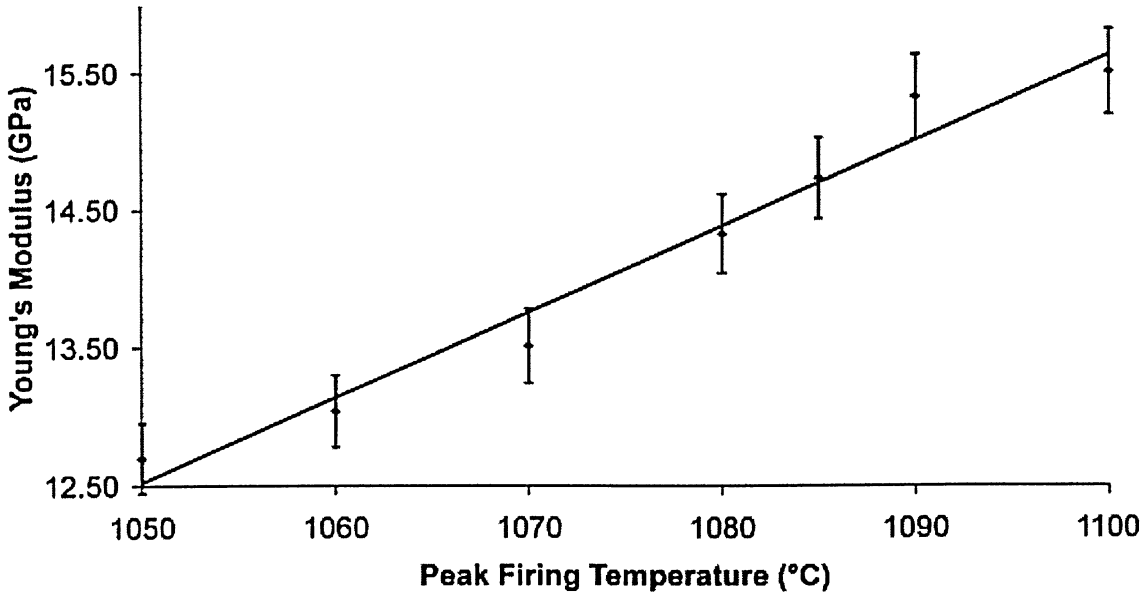

Figure 1.5: Modulus of Elasticity versus Firing Temperature (Aston et al., 2001)

The chemical processes that occur during the sintering stage include the burning of organic impurities, decomposition of carbonates and sulphates and the removal of chemically bonded water. Phase changes occur and break down certain products to form new compounds with new crystal microstructures that produce the desired material properties of the refractory.

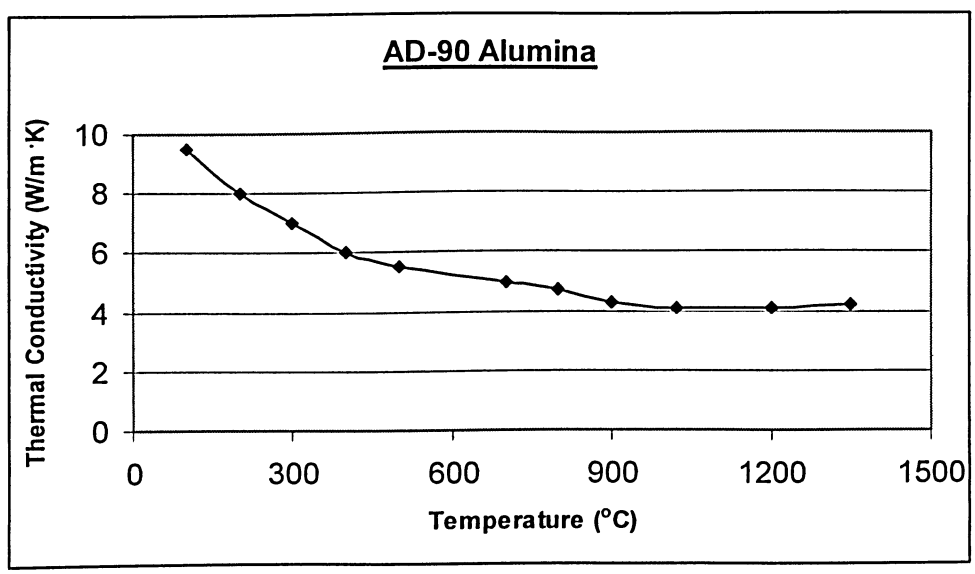

Figure 1.6: Temperature Dependence of Thermal Conductivity for an Alumina Refractory (Hemrick et al., 2003)

1.4 Behaviour of Refractory Materials at High Temperatures

For evaluating refractory linings in an industrial furnace, the behaviour of the material at high temperature is crucial. The thermal conductivity of a refractory varies with temperature. This produces non-linear temperature gradients. An example of the thermal conductivity versus temperature for an alumina brick is shown in Figure 1.6.

Figure 1.7 shows a general illustration for elastic behaviour of a material versus temperature. Typically, the modulus of elasticity decreases with an increase in temperature. In addition, as the temperature increases the Poisson's ratio increases. With an increase in temperature, a number of phenomena occur directly influencing the elastic properties. Materials tend to become more ductile which means that the strain increases under the same load. The load carrying capacity is also reduced. Increased ductility also produces higher strains in the radial direction, which accounts for the increase in the Poisson's ratio. The temperature also changes the elastic-plastic threshold (Gandhi and Jayaram, 2002) and is of interest where fatigue is an issue. The dynamic modulus of elasticity also decreases with an increase in temperature (Fraizier et al, 2002 and Roebben et al, 2002). Similarly, the dynamic Poisson's ratio increases with an increase in temperature (Agosta et al., 2002).

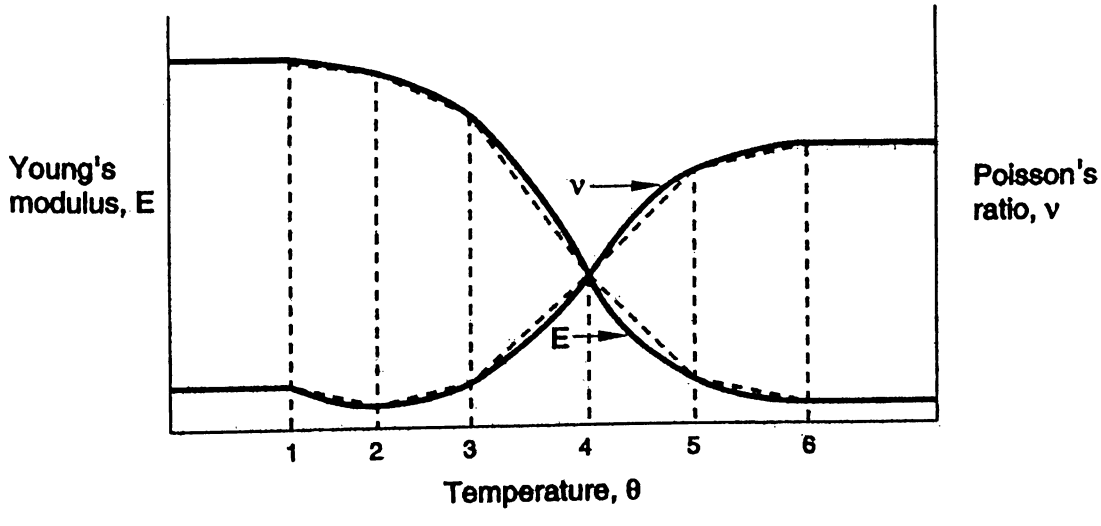

Figure 1.7: Elasticity and Poisson's Ratio vs. Temperature for a Generalized Material (Abaqus User's Manual Volume I, 2004)

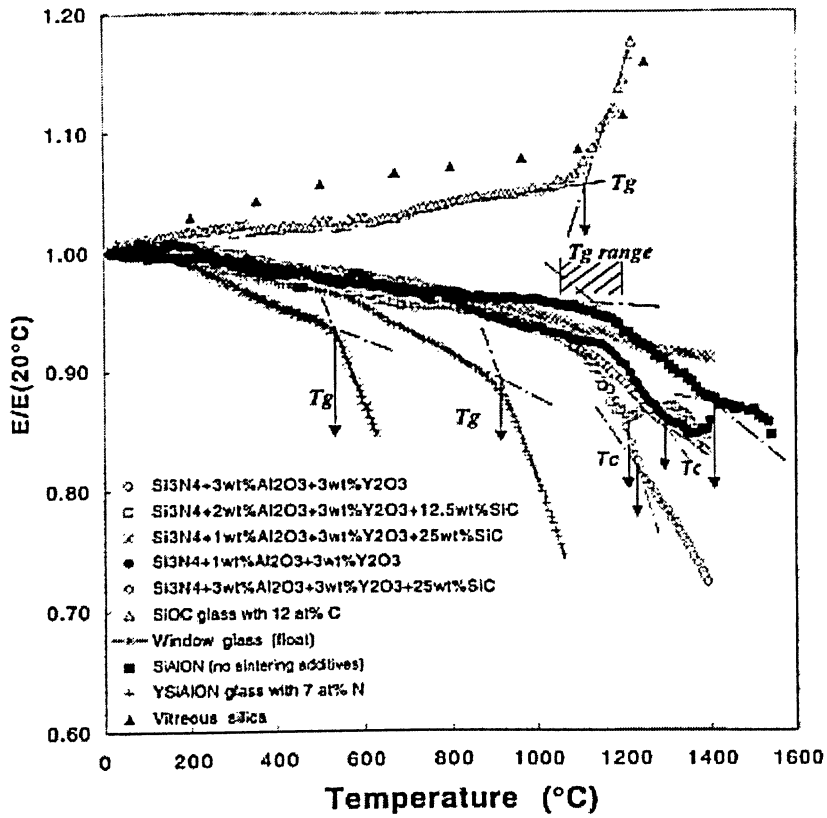

Figure 1.8: Modulus of Elasticity versus Temperature for Refractories Showing Phase Change (Rouxel et al, 2001)

Figure 1.8 shows the modulus of elasticity versus temperature for various refractory materials. The points on the curves marked *Tg* and *Tc* correspond to a glass transition and crystallization temperatures for the various materials. Each transition points marks a dramatic change in the elasticity. The top curve is noticeably different from the others. This particular material has an increase in the modulus of elasticity with an increase in temperature.

Dynamic elastic measurements of refractories rely on signal transmission through a material. These signals attenuate more rapidly as the temperature of the material increases (Gadaud and Pautrot, 2002; and Rebben et al., 2002). This is due to the higher kinetic energy of the particle motion interfering with the signal transmission. Input energy becomes a factor when attempting to measure the dynamic material properties at extremely high temperatures.

The heating of refractory materials produces other dynamic effects in a given sample. The frequency of vibration reduces (given the geometry does not change) as the temperature increases within a material (Daughton et al, 2003).

The cycling of high and low temperature creates a hysterises effect on the elasticity of a refractory material (Tessier-Doyen et al, 2004 and Cutard et al., 2004). This degradation is unavoidable and is difficult to estimate on an existing furnace structure. The hysteresis effect is due in part to the thermal shock coupled with the micro-cracking with successive heating and cooling cycles of the material. This results in reduced strength and lower elastic properties.

1.5 AU-E Correction For Temperature Change

To correct the dynamic measurements of the AU-E technique, a factor must be established to take into the account the changing material properties of refractories over a temperature gradient. The correction factor (α) is the ratio of elasticity under service conditions to the elasticity at room temperature. The elasticity under service conditions is a function of the temperature and thermal gradient along the length. Correcting for the temperature effect has the most influence on the accuracy of the AU-E technique making the technique the most feasible for evaluating the quality and thickness of furnace linings.

1.6 Research Objectives

The main objective of this thesis is to evaluate quantitatively the effect of the temperature correction factor on the accuracy of the acousto ultrasonic-echo technique. A methodology will be established to determine a correction factor (α) for the different refractory materials and a generalized equation will be derived.

1.7 Conclusion

Various NDT techniques are available for evaluating the refractory lining in industrial furnaces and have not proven very successful or can operate without interrupting the production schedule. For instance, thermal methods are subject to errors with poor evaluation of the temperature gradient. Radar and Magnetic methods can only evaluate the refractory linings from the inside of the vessel during a shutdown. The AU-E

technique can be performed from the exterior of the vessel while the furnace is still in operation. Some stress wave techniques such as impact echo or impulse response, can provide similar information of refractory linings. However, the AU-E technique is the more feasible due to the incorporation of the temperature correction. Ultrasonic methods provide limited information for furnace linings due to the ultimate frequency, sensitivity of the sensor needing couplant and the placement of the sensors is crucial in order to receive the transmitted signal.

1.8 Thesis Outline

The thesis is divided into 5 chapters. The present chapter describes the principal NDT techniques used to assess industrial furnace linings. An overview is provided of the properties of refractories and the behaviour of the materials at high temperatures.

Chapter 2 provides a more detailed discussion of the Acousto Ultrasonic-echo technique. This technique involves the application of stress wave theory and emphasis is placed on the derivation of the correction factor for the AU-E technique.

Chapter 3 covers the laboratory and field work investigations for this thesis. The laboratory phase consisted of heating and testing of refractory materials and concrete at various temperatures using the AU-E technique. Field work involved the investigation of two furnace roofs and the evaluation of a rotary kiln.

Chapter 4 discusses the analysis of results obtained from the laboratory and field work investigations. Results include the behaviour various materials at high temperatures and the derivation of α-factors

The focus of Chapter 5 is the conclusions of the study and introduces recommendations for further research.

Chapter 2

Acousto Ultrasonic-Echo Technique

2.1 Introduction

The acousto ultrasonic-echo technique is based on stress wave propagation in solids. Initially, this chapter focuses on the principles behind stress wave propagation and is followed by a discussion of the AU-E technique. Stress wave principles apply for all NDT stress wave techniques outlined in the previous chapter as well as for the AU-E technique.

2.2 Stress Wave Propagation in Solids

An elastic stress wave may be generated by exciting a physical body in some way. This may be done by impacting an external mass onto the medium producing either a plastic wave or an elastic wave depending on the magnitude of the impact. If the wave produces deformations in the plastic region, then the wave is considered to be a plastic wave. If the wave produces deformations within the elastic region, then the wave is said to be an elastic stress wave. For NDT stress wave techniques, the stress wave is well within the elastic range.

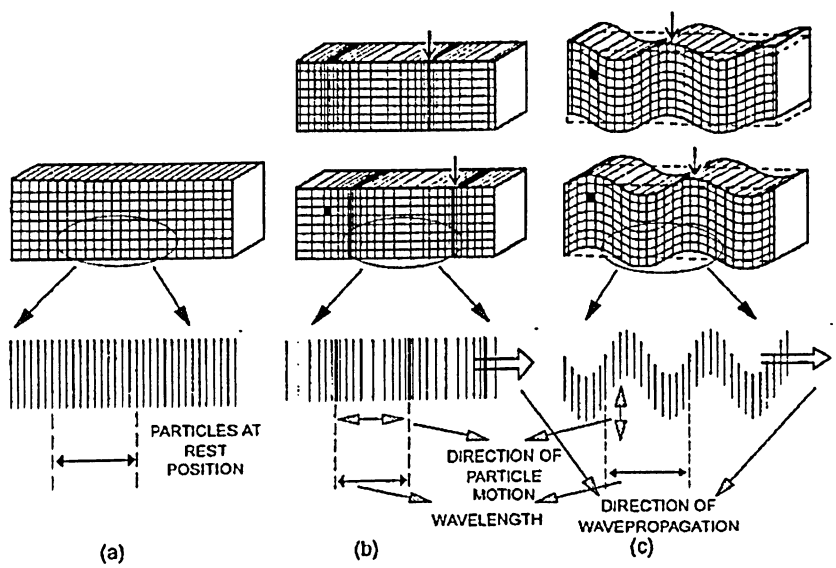

Figure 2.1: Motion of P-Waves and S-Waves (Sadri, 1996)

Stress waves cause mainly two types of deformations within a solid, compression and shear. Compression or longitudinal waves propagate in the direction of the applied load (Graff, 1991). These waves are also commonly referred to as P-waves and are illustrated in Figure 2.1(b). A shear or transverse wave moves through a medium with particle motion transverse to the propagation direction (Davis, 1988). These waves are also commonly referred to as S-waves shown in Figure 2.1(c).

Shear waves can be broken down into a horizontal component travelling parallel to the P-wave and a vertical component travelling perpendicular to the P-wave. The vertical or shear component will not travel through fluids due to low shear strength in this state. A third category of stress wave is the Rayleigh wave. This wave is a surface wave that originates at the loading source and travels along the surface or medium boundary (Doyle, 1997). These waves tend to dissipate quickly as they penetrate into the medium body.

The longitudinal wave speed for an isotropic material in an infinite elastic medium can be related to the density, dynamic elasticity and dynamic Poisson's ratio of a material by (Achenbach, 1973):

$$C_P = \sqrt{\frac{E_{DYN}(1-\upsilon_{DYN})}{\rho(1+\upsilon_{DYN})(1-2\upsilon_{DYN})}} \tag{2.1}$$

where; C_P is the P-wave speed, E_{DYN} is the dynamic modulus of elasticity, ρ is the density and υ_{DYN} is the dynamic Poisson's ratio. If the cross-sectional dimensions are small compared to the length, then the equation for the P-wave velocity can be simplified and is known as a guided wave (Sadri, 1996):

$$C_P = \sqrt{\frac{E_{DYN}}{\rho}} \tag{2.2}$$

The transverse wave speed for an isotropic material in an infinite elastic medium can be related to the density and shear modulus by (Achenbach, 1973):

$$C_S = \sqrt{\frac{G_{DYN}}{\rho}} \tag{2.3}$$

where; C_S is the S-wave speed, G_{DYN} is the dynamic shear modulus and ρ is the density. Equation 2.3 may be expressed in terms of dynamic modulus of elasticity and the dynamic Poisson's ratio:

$$C_S = \sqrt{\frac{E_{DYN}}{2\rho(1+\upsilon_{DYN})}} \tag{2.4}$$

The S-wave velocity is slower than the P-wave velocity, typically between 0.65 and 0.45 that of the P-wave (Sadri, 1996). Equation 2.5 can be used to determine the wave speed relationships.

$$\frac{C_S}{C_P} = \sqrt{\frac{(1-2\upsilon_{DYN})}{2(1-\upsilon_{DYN})}} \tag{2.5}$$

Equations 2.1 and 2.4 can be rearranged to expressed elasticity and Poisson's ratio as parameters of the longitudinal and shear wave velocities:

$$E_{DYN} = \rho C_S^2 \frac{4C_S^2 - 3C_P^2}{C_S^2 - C_P^2} \tag{2.6}$$

$$\upsilon_{DYN} = \frac{2C_S^2 - 3C_P^2}{2C_S^2 - 2C_P^2} \tag{2.7}$$

The surface wave speed can be approximated using the empirical relation given by Equation 2.7 (Sadri, 1996):

$$\frac{C_R}{C_S} = \frac{0.87 + 1.12\upsilon_{DYN}}{1+\upsilon_{DYN}} \tag{2.8}$$

where; C_R is the Rayleigh wave speed.

Typically, Equation 2.8 produces values between 0.9 and 0.92, showing that the speed of surface waves is the slowest of the three wave types. The above equations are valid only for isotropic materials in an infinite elastic medium. For an anisotropic material, the relationship between propagation direction and particle displacement is more complicated. Materials such as steel are isotropic but refractories display

anisotropic behaviour due to their non-homogenous matrices. The anisotropic properties are restricted locally due to individual grains in the microstructure. These local differences produce average mechanical properties in a particular direction. The above equations for isotropic materials may be used with an acceptable margin of error for non-homogeneous or anisotropic materials.

When a mechanical wave is generated in a furnace lining, it travels along the initial path until it reaches any boundary. This boundary confines the wave and a reflection will occur. A reflection and/or refraction can occur in an unbound or infinite solid at an interface between two solid materials. Reflections and refractions can also occur at a solid-fluid interface. Snell's Law states that at an interface of two mediums, the incident wave will refract towards the normal line moving from a lower density to a higher density medium (Serway, 1996). Figure 2.2 illustrates the interface of two different mediums.

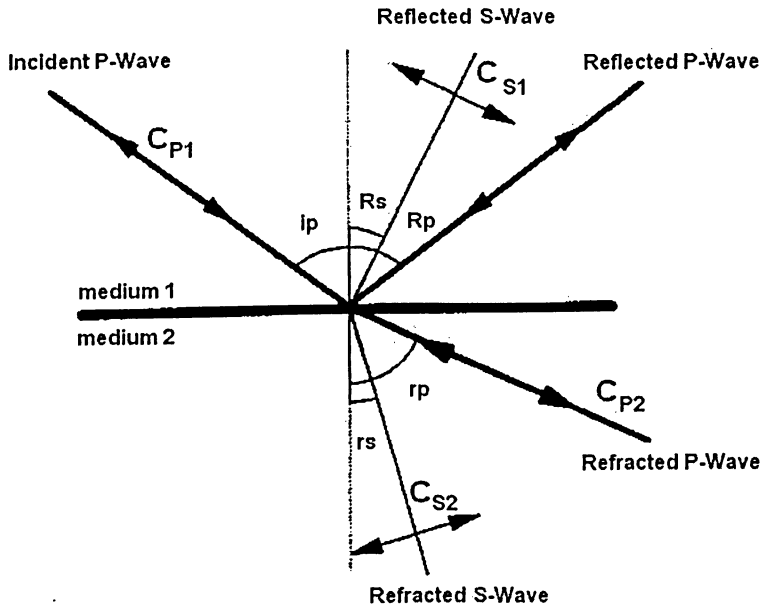

Figure 2.2: Behaviour of P-wave and S-wave at a media boundary (Sadri, 1996)

The waves can be described using Snell's Law and the various wave velocities as shown in Equation 2.9:

$$\frac{SIN(ip)}{C_{P1}} = \frac{SIN(Rp)}{C_{P1}} = \frac{SIN(Rs)}{C_{S1}} = \frac{SIN(rp)}{C_{P2}} = \frac{SIN(rs)}{C_{P2}} \qquad (2.9)$$

where; C_P and C_S are the P-wave and the S-wave respectively. The reflection/refraction angles are i_p, R_p, R_s, r_s and r_p. From Figure 2.2, medium 1 is considered the medium with the higher density due to the refracted wave having a larger angle (i.e.: $i_p < r_p$). Equation 2.9 is valid for any medium interaction. The reflection amplitude can be described in terms of impedance as given by Equation 2.10 (Pollard, 1977).

$$Z = \rho \cdot C_P \tag{2.10}$$

where; Z is the characteristic impedance of the material. The amplitudes of the incident and reflected stress waves will be at a maximum when the angle of incidence is zero degrees and can be related using Equation 2.11 (Tedesco et al, 1999).

$$\frac{\sigma_R}{\sigma_i} = \frac{Z_1 - Z_2}{Z_1 + Z_2} \tag{2.11}$$

where; Z_1 and Z_2 are the characteristic impedance of the two mediums and σ_R and σ_i are the magnitudes of the reflected and incident waves, respectively. The amplitudes of the refracted or transmitted waves can be related using Equation 2.12 (Tedesco et al, 1999):

$$\frac{\sigma_T}{\sigma_i} = \frac{2Z_2}{Z_1 + Z_2} \tag{2.12}$$

where; the magnitude of the transmitted wave is denoted σ_T and the magnitude of the incident wave is denoted by σ_i. The variables Z_1 and Z_2 are impedance characteristics of the two mediums. For a multi-layer case, enough input energy must be applied when the layers have progressively lower characteristic impedance since a higher fraction of the energy is reflected back to the source from each layer.

2.3 The Acousto Ultrasonic-Echo Technique

The AU-E technique is based on the stress wave propagation theory outlined in the previous section. The technique evaluates the reflections and refractions produced by the stress waves in order to convert the data into useful information. The basic setup for the technique is shown in Figure 2.3.

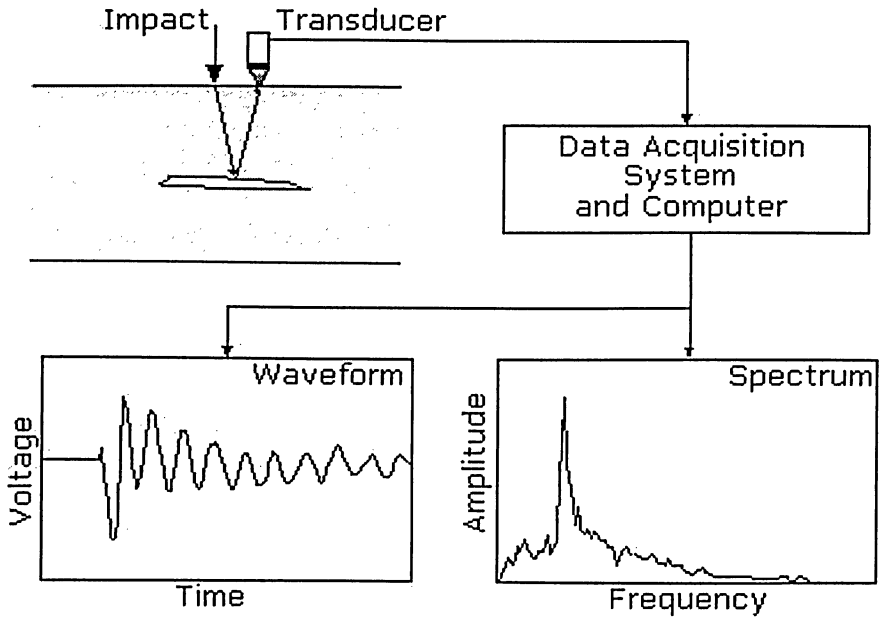

Figure 2.3: Acousto Ultrasonic-Echo Configuration

The stress wave is generated by a mechanical impact, usually a spherical object of known diameter. The wave travels into the material refracting and reflecting at all boundary interfaces and retuning to the surface. Reflections from different locations in the material return to the surface at different instances in time as surface displacements. These displacements or vibrations are captured with a piezoelectric sensor and are plotted by a digitizer in a time domain. A processing unit is used to convert the time domain data into a frequency domain by a fast Fourier transform (FFT). These frequencies are used in conjunction with the wave velocity of the material to determine the presence of flaws and discontinuities.

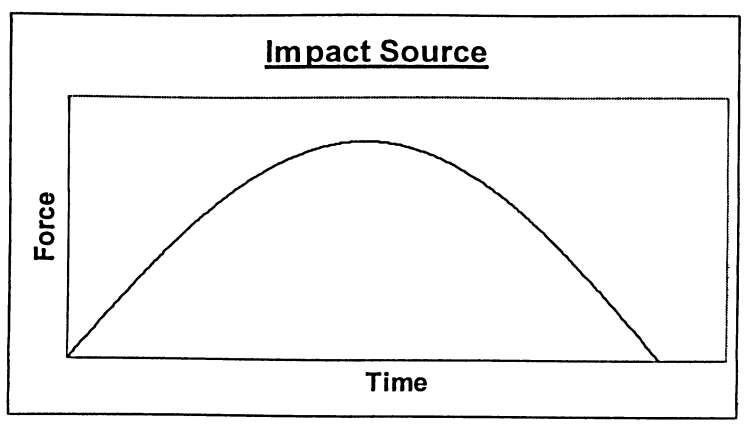

Figure 2.4: Impact Load

The impact source is a crucial aspect of the technique and must produce a spherical wave front. This is achieved with a spherical tipped impact load with a force magnitude shown in Figure 2.4. Characteristics of the impact source will produce various amplitudes and frequencies of the generated waves. The resulting stress wave is proportional to the maximum force generated by the impact and the contact time is a function of the sphere diameter. The contact time can be related to the sphere diameter by an empirical formula (Sansalone and Streett, 1997):

$$t_C = 0.0043D \tag{2.13}$$

where, t_C is the contact time in seconds and D is the diameter of the sphere in metres. Equation 2.13 is only valid for coarse-grained materials such as refractories or concrete.

Impact generated stress waves are composed of a broad band of frequencies with each frequency corresponding to a specific portion of the force time function shown in Figure 2.4. For lower range frequencies, the maximum useful frequency is proportional to the contact time (Sansalone and Streett, 1997):

$$f_{MAX} = \frac{1.25}{t_C} \tag{2.14}$$

Equation 2.13 can be substituted into Equation 2.14 yielding:

$$f_{MAX} = \frac{291}{D} \tag{2.15}$$

where; f_{MAX} is the frequency in Hz and D in the diameter of the sphere in meters. The impact produces a frequency spectrum ranging from zero up to the maximum frequency. Decreasing the diameter of the impact will increase the upper limit of the generated frequency spectrum. However, this reduces the amount of input energy applied to the system, which can attenuate within large depths.

The wavelength can be described by the relationship shown below:

$$\lambda = \frac{C_P}{f} \tag{2.16}$$

where; λ is the wavelength in meters and f is the frequency in Hz. The shortest wavelength must be less than the size of the smallest flaw that is desired for detection. Refractory materials are porous and posses micro-cracks. Micro-cracks and other small voids are distributed throughout a specimen and although contribute to a reduction in material strength, they do not compare to the effect of large cracks and delaminations. If flaws are smaller than the shortest wavelength generated, then the wave will travel through the medium as if it is continuous or homogeneous (Sansalone and Streett, 1997).

The displacements or vibrations produced by the excitation are detected using a piezoelectric sensor. Piezoelectricity is the property possessed by some materials to become electrically charged or generate a voltage when subjected to a mechanical stress. For furnace applications, only specific types of piezoelectric transducers can be used due to extreme sensitivity to heat.

The voltages generated by the piezoelectric sensor are captured using a data acquisition system to produce a time domain. The time domain is converted into a frequency domain via the fast Fourier transform (FFT). The fast Fourier transform is a stepwise mathematical solution to a Fourier transform integral. The FFT uses samples of data on the order of 2^x to display time domain data in terms of frequency and relative energy of the displacements. An example of two time domain data sets with the corresponding FFT spectrums are shown in Figure 2.5.

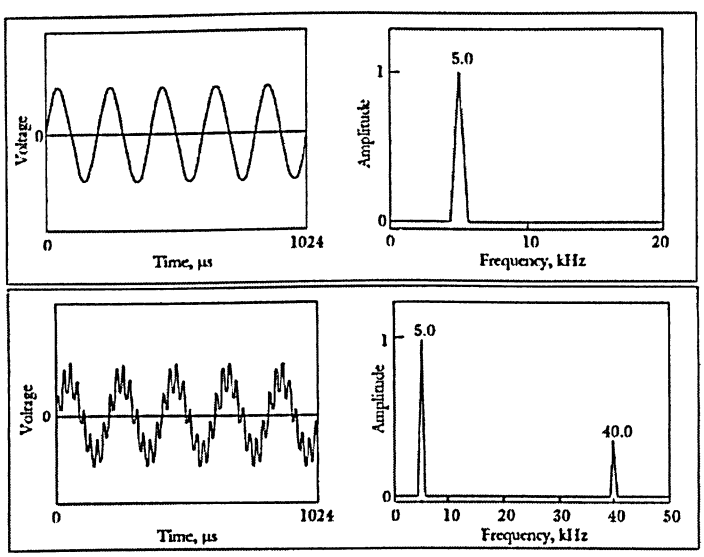

Figure 2.5: Effect of Sampling on Frequency Output (Sansalone and Street, 1997)

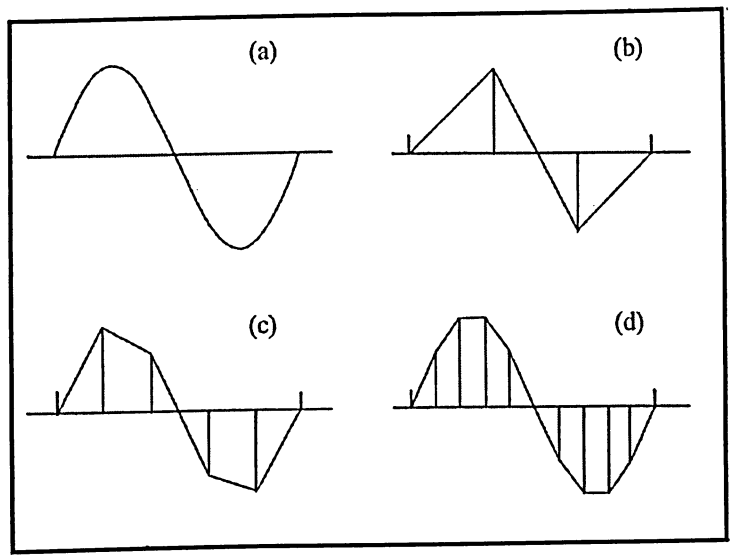

Figure 2.6: Sampling of a Perfect Wave (Sansalone and Street, 1997)

The time scale in which the resonance is recorded is in the order of microseconds. The data acquisition system collects voltage readings in time separated by a defined time interval. Conversion of analog signals to digital requires enough samples per second to be collected in order to reproduce a continuous representation of the motion. This is known as the sampling rate. An illustration of the sampling rate is depicted in Figure 2.6. Figure 2.6(a) shows a perfect sinusoidal wave in a given sample of time. Part (b) in the figure shows a four-point sampling of the sinusoidal wave. Part (c) shows six-point sampling and part (d) shows eleven-point sampling of the wave. Increasing the sampling rate increases the number of points captured in a given time frame. By increasing the sampling rate, higher frequencies can be captured as shown in the second illustration of Figure 2.5. The sampling rate is give by Equation 2.17.

$$\Delta t = \frac{1}{SR} \tag{2.17}$$

where; SR is the sampling rate in Hz and Δt is the time interval between points in microseconds. The sampling rate must be at least two times greater than the maximum frequency desired to be captured (Sansalone and Street, 1997). The resolution for the frequency domain can be calculated using Equation 2.18:

$$\Delta f = \frac{SR}{N} \tag{2.18}$$

where; Δf is the frequency resolution in Hz and N is the number of samples.

The fundamental equation for the AU-E technique was developed by (Sadri, 1997) at Andec International Services Corporation. Equation 2.19 is a modification to the impact echo relationship incorporating the temperature correction factor α, introduced in the previous chapter (Sadri, 1997):

$$f = \frac{\alpha\beta C_P}{2T} \tag{2.19}$$

where; f is the frequency as determined from the AU-E instrumentation, C_P, is the wave speed of the material, T is the thickness or depth of the reflecting surface corresponding to a particular frequency and β is the shape factor. The temperature effect is corrected by the α-factor and is a function of the elastic properties of the material. The generalized equation for the α-factor omitting the contribution of linear expansion is shown below:

$$\alpha = \frac{E_x}{E_o} \tag{2.20}$$

where;

$$E_x = \left(\frac{1}{T_2 - T_1}\right)\left(\frac{1}{x_2 - x_1}\right)\int\int E(T(x)dx)dT \tag{2.21}$$

where; E_x is the average modulus of elasticity with respect to temperature and depth, E_o is the modulus of elasticity at room temperature, T_1 and T_2 are the boundary temperatures and x_1 and x_2 are the boundary thicknesses of the temperature gradient. The double integral accounts for the temperature gradient depending on the depth. This is incorporated into the dependence of the modulus of elasticity on the temperature. The functions for the integral in Equation 2.21 can be determined experimentally. The function of the modulus of elasticity is generally complex and the integral can only be solved using numerical methods.

Multiple reflections of P-waves excite a particular mode of vibration in the specimen and displacements caused by this mode produce principle periodic patterns in the waveform (Sansalone and Streett, 1997). This acts to amplify the wave speed within a material. Finite element models have predicted the approximate wave speed for certain shapes and have been verified by experiments. The ratio of theoretical to actual wave speed is called the shape factor and is described by Equation 2.22.

$$\beta = \frac{C_M}{C_{TH}} \tag{2.22}$$

where; β is the shape factor, C_M is the measured or actual wave speed and C_{TH} is the theoretical wave speed as determined by Equation 2.1 or 2.2. Pre-determined shape factors are shown in Table 2.1.

Table 2.1 Shape Factors
(Sansalone and Streett, 1997)

Shape	β
Square	0.87
Cylinder	0.92
Plate	0.96

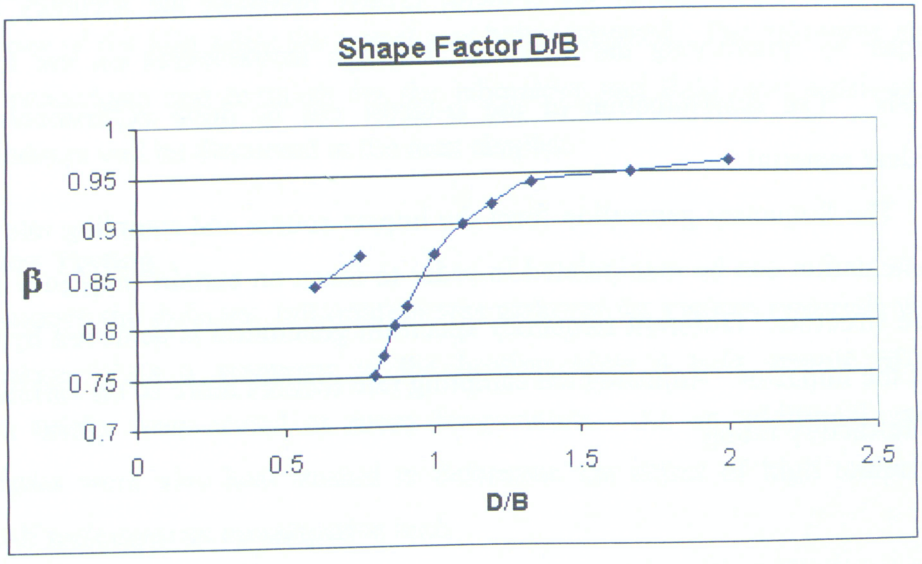

Figure 2.7: Shape Factor for a Rectangular Section (Sansalone and Streett, 1997)

When the cross-section is rectangular the depth to width ratio influences the shape factor. Figure 2.7 displays the shape factor for different depth to width ratios (D/B). The figure shows a discontinuity between when the D/B ratio approaches 0.75 and 0.8.

In many situations, the refractory lining evaluated by the AU-E technique in the furnace is composed of multiple materials each with their own distinct properties. This produces a complex resulting vibration and is handled by the multiplayer relationship.

$$f_T = \frac{1}{\frac{2T_1}{\alpha_1\beta_1 C_{P1}} + \frac{2T_2}{\alpha_2\beta_2 C_{P2}} + \ldots\ldots + \frac{2T_n}{\alpha_n\beta_n C_{Pn}}} \qquad (2.23)$$

The resultant frequency of vibration is the sum of the individual layer vibrational contributions. Each layer can have a unique wave speed and temperature correction.

2.4 Chapter Summary

The basis of the AU-E technique is the application of elastic stress wave propagation in solids. The reflections of the waves allow for detection of the discontinuities and flaws associated with damaged furnace lining material. Reflections will occur at material interfaces of different characteristic impedance such as solid/fluid or solid/solid interfaces. Input energy becomes a factor at high temperatures where the signal attenuates more rapidly.

The incorporation of the α-factor greatly increases the accuracy of the AU-E technique by quantifying the effect of the high temperatures on the furnace lining materials. The determination of the α-factor can be done experimentally for each individual material.

The frequency generation form the impact source and sampling rate of the AU-E instrumentation can be manipulated in order to focus on certain frequency ranges of the furnace structure. Different frequency spectrum generation is achieved by changing the size of the impactor. Adjusting the sampling rate focuses more so on various thicknesses of the refractory lining.

Chapter 3

Field Work and Laboratory Testing Setup

3.1 Introduction

This chapter outlines the methods and procedures for the various field work and laboratory experimentations conducted relating to this thesis. The laboratory testing includes the inspection of a bulk sample of newly manufactured refractory bricks that will eventually be used in an industrial furnace. The purpose of this test was to evaluate and quantify the variability of manufactured refractory materials. Further laboratory work included the heating and testing of various refractory materials at high temperatures. The heated refractory materials investigated were a 70% alumina brick, a 90% alumina brick, a fire brick and a castable refractory. For this investigation, high temperature effects were also examined for some concrete materials. To complement the heating of the refractory materials in the laboratory, finite element models were used to evaluate the effect of temperature dependent thermal properties on the temperature gradient.

Field work included the testing of two industrial furnace roof structures and a rotary kiln. Multiple inspections of the roof structures were carried out in order to determine the α-factor and the effect of a multi-layered scenario. The investigation of the rotary kiln provided an opportunity to verify the AU-E measurements using a covermeter from the interior of the kiln while the vessel was being repaired. The following sections describe the procedures and methods for the laboratory and field investigations. The results and findings will be discussed in the next chapter.

3.2 Laboratory Testing

In order to quantify the α-factor, information was gathered for various materials while at high temperatures. As a precursor to the heating trials a bulk sample of newly manufactured bricks were tested at room temperature. As an additional exercise, concrete samples were also heat treated to determine the effect of high temperatures using the AU-E technique an investigative tool.

3.2.1 Variability of Manufactured Samples

Although the properties of manufactured bricks are uniform in nature due to advancements in manufacturing techniques, the processes invariably produce variations in the resulting product. The sintering temperature can affect the material properties and it is difficult to ensure the temperature distribution in the sintering chamber is uniform and results in localized temperature variations. Newly manufactured 70% alumina refractory bricks were tested using the AU-E technique to quantify any differences form specimen to specimen.

The sample size for the investigation was initially unknown since the degree of the variation would govern the number of samples required to adequately represent the population. The desired level of confidence is 95% and the acceptable statistical error for the sample mean was arbitrarily chosen as 2%. Assuming a normal distribution curve, the number of samples required is represented by:

$$n = \left(\frac{z_{\alpha/2}\sigma}{err} \right)^2 \tag{3.1}$$

where; n is the sample size, $z_{\alpha/2}$ is the normally distributed confidence interval, err is the acceptable error and σ is the standard deviation of the mean. The sample size n and the standard deviation were calculated dynamically and entered into Equation 3.1 to check if an adequate number of samples were evaluated. The length of the samples was 380 mm. The sampling rate and data number used was 500 kHz and 2048 points respectively. The impactor size used was 3 mm in diameter.

3.2.2 Heat Treatment of Materials

Samples were heated in a kiln with a chamber volume of 90 cm^3 having an inner diameter of 45 cm and a chamber height of 57 cm. The controls on the kiln allowed for adjustable heating and cooling rates and could be programmed for specific soak times. The maximum recommended operating temperature by the manufacturer for the kiln is 1300°C. Samples of the materials were placed on an elevated platform such that top surfaces of the specimens were at the same elevation as the top of the kiln wall. A 25-mm thick insulating blanket, which could resist temperatures up to 1500°C was used to insulate the chamber of the kiln.

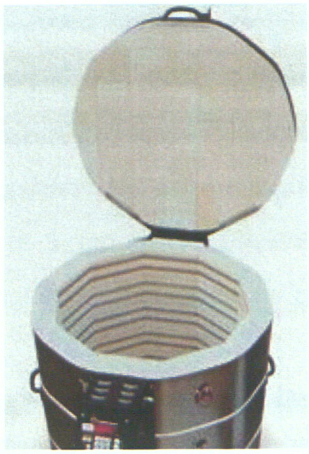

Figure 3.1: Kiln Assembly

Access holes were cut in the insulating blanket to allow the top surface of the samples to be exposed for testing using the AU-E technique. Two layers of the insulating blanket were used to cover the specimens within the kiln to reduce the heat loss. Figure 3.1 shows the kiln assembly used for heating the samples.

The AU-E instrument provided a frequency, which was used in Equation 2.19 along with a known geometry. To ensure that the geometry did not change, thermal shock was a key consideration. Thermal shock occurs in a material with the presence of a sharp thermal gradient. If the expansive strains under a thermal load exceed the allowable tensile stress, then the refractory material will begin to exhibit fractures. These fractures can be small scale such as micro-cracks or can be on a larger scale resulting in large structural cracks. Depending on the wavelength generated by the impact, certain size cracks can be ignored. As a precaution, the heating of the materials must be done slowly to ensure that large cracks due to thermal shock are avoided. An estimation of the time needed for the heat flow in a material is known as transient heat conduction.

A simplified dimensionless method can be used to calculate one-dimensional transient heat flow by using dimensionless factors knows as the Biot number and Fourier number. The Biot number is the ratio of thermal conductance at a surface to the thermal conductivity of a solid. The relationship for the Biot number is shown by Equation 3.2 (Incropera and De Witt, 1990):

$$Bi = \frac{hL}{k} \tag{3.2}$$

where; Bi is the Biot number and is dimensionless, h is the heat transfer coefficient ($W/m^{2\bullet}K$), k is the thermal conductivity ($W/m^{\bullet}K$) and L (m) is the length of the temperature gradient. The Fourier number is an indication of the speed of cooling or heating of a solid body. The relationship for the Fourier number is shown in Equation 3.3 (Bayley et al, 1972):

$$F = \frac{\alpha_{TD} t}{L^2} \tag{3.3}$$

where; F is the Fourier number and is dimensionless, α_{TD} is the thermal diffusivity (m^2/s), t is the heat transfer time (seconds) and L (m) is the length of the temperature gradient. Thermal diffusivity (α_{TD}) is the ability of a material to conduct thermal energy relative to its ability to store thermal energy (Incropera and De Witt, 1990). The relationship for thermal diffusivity is shown in Equation 3.4:

$$\alpha_{TD} = \frac{k}{\rho \cdot c_P} \tag{3.4}$$

where; α_{TD} is the thermal diffusivity (m^2/s) of a material, k is the thermal conductivity ($W/m^{\bullet}K$), ρ is the density (kg/m^3) and c_p is the specific heat ($J/kg^{\bullet}K$) of a material.

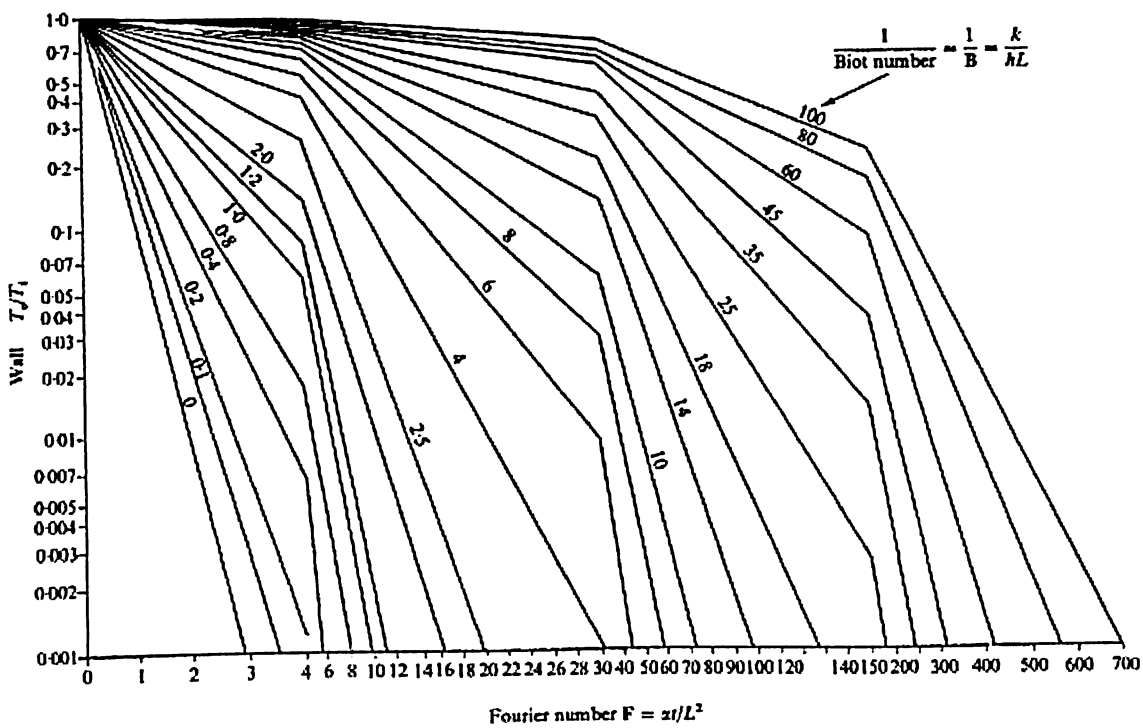

Figure 3.2: Biot and Fourier Number For 1–D Heat Conductance (Bayley et al, 1972)

Equations 3.2 through 3.4 can be used with Figure 3.2 to produce an estimate for the heating time of the sample materials. In the figure, the ratio T_c/T_i is the ratio of the respective boundary temperatures of the thermal gradient. Using material properties of a typical cast-in-place refractory, an estimate can be made to evaluate the time needed for the heat transfer to occur over a 1 cm differential element of material for a 100°C temperature gradient. The material properties are shown in Table 3.1.

Table 3.1: Typical Properties For Cast-In-Place Refractory

Property	Symbol	Value
Thermal Conductivity	k	1.48 W/m•K
Density	ρ	2290 kg/m^3
Specific Heat	c_p	0.88 J/kg•K
Length	L	0.01 m
Heat Transfer Coefficient (Free Gas)	h	25 W/m^2•K
Temperature Gradient	T_c/T_i	100°C/200°C

Using the values in Table 3.1 along with Equations 3.2 to 3.4 and Figure 3.2, yield an approximate heating time of 9 minutes for a 1 cm temperature gradient of 100°C. This is the theoretical time needed and does not take into account the resistance of thermal shock. Likely, the thermal shock will govern the heating time in most situations. The above method for transient heat conduction does not take into account thermal cracking and contact resistance. The transient heat conduction calculation does aid in the estimation of soak time needed to ensure the uniform temperature of a material at a specific temperature. As a guideline, soak time will be a minimum of 9 min/cm along the shortest physical cross-sectional dimension to the core of each refractory specimen. The increment will be 100°C for all temperature steps.

3.2.3 Heat Trials For Refractory Materials

Materials tested from industrial applications are a firebrick, a cast-in-place refractory and a 70% alumina brick. A 90% alumina brick was also tested. Table 3.2 provides a list of materials used in the kiln testing along with the calculated minimum soak times for each of the specimens.

Table 3.2: Material List for Heat Conditioning

Material Type	Number of Samples	(Length x Width x Height) mm	Testing Type	Minimum Soak Time
Fire Brick	3	64 x 113 x 229	NDT	30 min
90% Alumina Brick	3	75 x 113 x 229	NDT	35 min
70% Alumina Brick	3	150 x 115 x 380	NDT	52 min
Castable Refractory	3	150 x 190 x 175	NDT	68 min

Three samples of each refractory material were used for the heating trials. The temperature increments used was 100°C with AU-E readings taken at each increment. In an effort to avoid thermal shock effects, the heating rate used was 300°C/hr. For large scale industrial furnaces, the heating rate can be as low as 10°C/hr in which can take days to reach operating temperatures. Issues arise more from structural limitations than from material limitations. For the case of a stand-alone brick sample, a heating rate of 300°C/hr is within a safe regime.

Thermal shock can not be avoided when heating refractories or concretes because these materials are not purely elastic. Materials of comparatively higher strength in compression and in tension will have a higher resistance to thermal shock. Materials of comparatively lower elasticity will have a higher resistance to thermal shock by allowing more strain energy to be absorbed. The thermal expansion coefficient is a measure of the ratio of expansion to a change in temperature. Having this value comparatively lower will reduce thermal shock. Comparatively higher thermally conductive materials will also reduce thermal shock effects by reaching temperature equilibrium in a shorter time. Higher comparative porosity reduces strength and reduces thermal conductivity, which is detrimental to thermal shock resistance. However, large pour voids will limit crack propagation by intersecting fracture planes.

For cooling, the same rate of 300°C/hr was used to resist thermal cracking. In the case of cooling, the material is even more susceptible to cracking. This is due to the free surface of the material exposure to the cooler temperature. It may be easier to explain the heating process. While heating, although thermal shock is an issue, the mass of the solid

object tends to confine the expansive forces from within. In the case of cooling, the free surface of the specimen has little or no confinement.

The refractory specimens were tested using a 500 kHz sampling rate with 4096 data points. The impactor size used was 3 mm in diameter.

3.2.4 Heat Trials For Concrete Specimens

Along with the refractory materials, heat trials of various concrete samples were performed to evaluate the behaviour as a result of high temperature exposure. Table 3.3 provides a list of the concrete mixes used in the kiln heating trials. A larger number of samples were tested in the concrete heating trials due to the destructive nature that the high temperature effect will have on the samples. Two main objectives were sought in this section of testing; the behaviour of concrete materials at high temperatures and the residual properties of the material once cooled to room temperature. The overall performance between normal concrete and high strength concrete (self compacting concrete) at various exposure temperatures was compared. Fibre addition to the concrete mix was investigated to establish if any intergrity benefit was be made after high temperatue exposure.

Table 3.3: Materials Used for Concrete Heat Conditioning

Material Type	Samples	D x h (mm)	Type of Testing	Min. Soak Time (min)
Normal Strength Concrete (Mix 1)	19	ϕ100 x 200	NDT + Destructive	360
Normal Strength Concrete (Mix 2)	19	ϕ100 x 200	NDT + Destructive	360
Self Compacting Concrete (Mix A)	19	ϕ100 x 200	NDT + Destructive	360
Self Compacting Concrete (Mix A + Metal Fibres)	4	ϕ100 x 200	NDT + Destructive	360
Self Compacting Concrete (Mix B)	19	ϕ100 x 200	NDT + Destructive	360
Self Compacting Concrete (Mix B + Polypropylene Fibres)	8	ϕ100 x 200	NDT + Destructive	360

Four mix designs were considered in the experiment. Two normal strength concrete mixes and two high strength concrete mixes. The capacity of the mixer restricted the number of specimens that could be made in each batch. The fibres were only added to the high strength concrete mix. Four cylinders were made using steel fibres in Mix A and eight cylinders were made using polypropylene fibres in Mix B. The specimen size used were standard 100 mm diameter by 200 mm cylinders. The ends of each specimen was pollished using a grinder to produce a smooth flat surface for compression testing. This provides an excellent surface for the AU-E sensor although not a requirement. The static modulus of elasticity was determined and to avoid errors, the capping compound was not used. Each specimen was weighed prior to each test as well as after the heat treatment as long as the specimen remained intact.

The concrete specimens were cast and cured in a chamber which had at least 90% relative humidity and a temperature of 23°C for 28 days. Prior to the heat treatment, each sample was weighed and evaluated using the AU-E equipment. Volumetric calculations were performed using callipers accurate to one ten thousandths of a millimetre.

The maximum heating rate used for the concrete specimens was 300°C/hr up to the respective temperature for each trial. Once at the maximum temperature for the particular trial, the soak time for each sample was six hours. The temperature increment for each trial was 100°C up to a maximum temperature of 1000°C. An example of the temperature loading is shown in Figure 3.3 as recorded during the testing trials. From the figure, the initial heating rate was 300°C/hr, which corresponds to the slope leading up to approximately 600°C. Once the temperature of the kiln exceeds 600°C, the heat loss to the surrounding environment begins to influence the heating rate. This region of the heating curve is indicated by the dashed line between 600°C and 1000°C. Eventually, the target temperature was reached and a six hour soak time was used for each specimen shown by the plateau in Figure 3.3. The cooling rate of the chamber was also set to a maximum of 300°C/hr. Rapid heat loss to the environment was controlled by the instrumentation as shown by Figure 3.3 in the region between 1000°C and 600°C. Once at 600°C, the cooling rate dropped below the maximum rate due to the insulating ability of the kiln. This region is indicated by the dashed line at approximately the 12 hour mark in Figure 3.3.

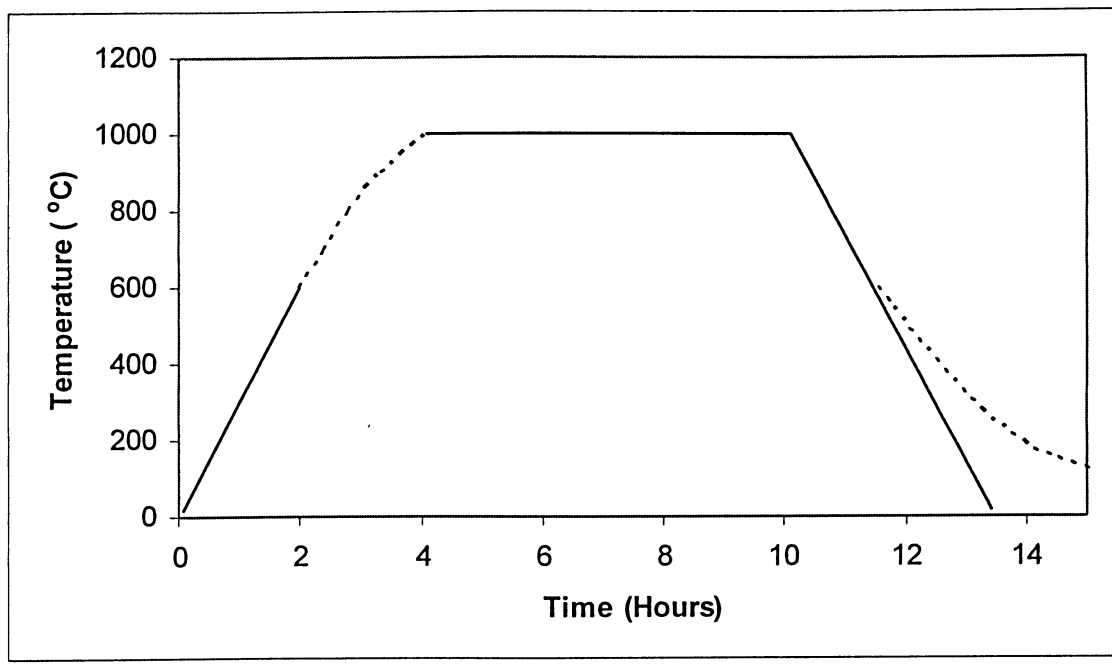

Figure 3.3: Thermal Loading and Soak Time for the 1000°C Trial

After the heat treatment, the samples were removed from the kiln and reweighed to determine the mass loss. AU-E measuremets were taken on the heat damaged samples for a comparison to the initial undamaged readings. The sampling rate used for the AU-E measuremets was 100 kHz with 1024 data points.

Residual properties of the concrete specimens were evaluated using compression testing to determine the static modulus of elasticity and to estimate the compressive strength. ASTM Standard C469-94 was followed for the compression testing. To obtain the static modulus of elasticity both the stress and strain was recorded with a loading rate of 241 ± 34 kPa/s as outlined by the ASTM standard. For this specimen size, the compression machine loading rate was 1.89 ± 0.27 kN/s.

At least one sample from each mix was tested at each temperature increment. Multiple samples were tested at the higher temperature settings due to limitations on liturature supporting the behaviour of concrete at the higher temperatures. The specimen temperature distribution is summerized in Table 3.4. Two samples were tested at room temperature using the AU-E technique followed by the compression testing to establish baseline properties. Successive samples were only tested using the AU-E technique at

room temperature to provide comparative estimations of the properties since the compression testing was performed after the heat treatment.

Table 3.4: Temperature Distribution for Concrete Specimens

Specimen Type	20 (°C)	100 (°C)	200 (°C)	300 (°C)	400 (°C)	500 (°C)	600 (°C)	700 (°C)	800 (°C)	900 (°C)	1000 (°C)	20 → 1000 (°C)
Mix 1	2	1	1	1	1	2	2	2	2	2	2	1
Mix 2	2	1	1	1	1	2	2	2	2	2	2	1
Mix A	2	1	1	1	1	2	2	2	2	2	2	1
Mix A Steel								1	1	1	1	
Mix B	2	1	1	1	1	2	2	2	2	2	2	1
MixB Polyprop.				1	1	1	1	1	1	1	1	

The main objective of the concrete heating trials was to obtain the residual properties of the concrete samples. In addition, one sample from each batch was tested while at each of the increment temperatures as indicated by the last column in Table 3.4. The procedure used was similar to that of the refractory testing outlined above. This information provided insight into the behaviour of concrete materials while at high temperatures.

3.3 Field Work

An application of the experimental findings was applied to three industrial furnaces. Two furnace roof structures were evaluated along with a rotary kiln. There are two major areas impacted by the information provided by the AU-E evaluations. The first area is the remaining lining quality and thickness for structural integrity and heat transfer considerations. AU-E technique is capable of identifying discontinuities and flaws. The second class of information is the wearing rate of the lining. The wear rate is determined through multiple inspections and can provide a physical implication of process conditions. Information of the wearing rate will ultimately have the greatest influence on the service life of the vessel.

3.3.1 Investigation of Furnace Roof #1

The refractory material used in the roof lining is a high alumina brick surrounded by a castable material. The roof itself has dimensions 47 m x 13 m. The structural system for the roof consists of a series of steel beams with adjoining sleepers at 300 mm spacing. The alumina bricks are used as anchor bricks and hang along the sleepers also at 300 mm spacing. The tight 300 x 300 mm centre to centre spacing is due to the weak tensile strength of the refractory. The side surfaces of the hanger bricks are perforated to increase the shear resistance between the castable and hanger brick interface. The weak link in the roof insulating system is the hanger brick itself. These bricks are most vulnerable to deterioration from thermal loading causing large stresses to develop during temperature fluctuations. The bricks also undergo deleterious changes in the microstructure above 1400°C which can occur at the hot-face and can eventually migrate with the onset of spalling.

The objective of the AU-E inspection was to determine the condition of the anchor bricks in order to provide a structural assessment of the roof insulating system. Figure 3.4 shows a dimensional sketch of the hanger brick. The overall length of the brick is 380 mm with a castable thickness of 230 mm from the hot-face of the brick.

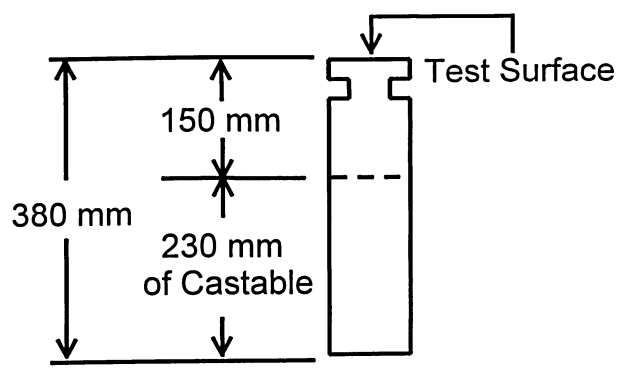

Figure 3.4: Dimensional Sketch of the Hanger Brick (70% Alumina)

Anchor bricks were assessed by quantifying the depth of cracks within the length of the specimen. Sufficient hanger brick material should remain intact along its length in order to provide adequate shear interaction at the castable interface. The testing surface is the exposed portion of the brick connected by mounting brackets to the sleeper beams. The

thickness of the sample refers to the distance from the testing surface down to the crack/discontinuity interface or in the case where there are no defects, the full length.

In order to increase the accuracy of the measurements, sections of the furnace were tested both on-line (hot) and off-line (cold) to evaluate the α-factor of the existing brick. The findings are also compared to the laboratory testing of the 70% Alumina samples in the kiln. The sampling rate and data number used for the roof inspection was 500 kHz and 2048 points respectively. The impactor size used was 3 mm in diameter.

3.3.2 Investigation of a Rotary Kiln

Rotary kilns are used in various process applications such as cement manufacturing and ceramic manufacturing. Typical temperatures inside a working kiln can reach upwards of 1500°C in the hot zone and consequently produce shell temperatures of 100-300°C. The refractory material used in the kiln was a cast in place high magnesia refractory with an original thickness of 250 mm. The rotary kiln dimensions were 4.9 m in diameter and a length of 60 m. Figure 3.5 shows an image of the rotary kiln investigated in this study.

Figure 3.5: Rotary Kiln

The main objective of this investigation was to evaluate the remaining thickness of refractory lining in a working rotary kiln so as to not interrupt production. A cast in place refractory relies on the heat generated from the kiln itself to sinter the green material.

The various layers of the refractory are sintered at different temperatures due to the temperature gradient and thus produce varying properties throughout the thickness.

The motion of the kiln produces a compression-relax cyclic load due to the turning action of the kiln. This fatigues the lining material over time. Other areas are vulnerable where the combustion process is occurring creating localized high temperatures. The test stations are situated lengthwise along the kiln in two rows at opposite sides to one another. These rows were arbitrarily named "A" and "B". The spacing between points on each of the testing rows is 2 m along the entire length of the kiln. An infrared temperature sensor was used to evaluate the shell temperature at each of the test locations in order to evaluate the temperature gradient.

Figure 3.6 illustrates the shell and refractory setup encountered while testing the kiln. A 50-mm steel shell covers the 250 mm of refractory material. The AU-E signals are sent through the steel shell and into the refractory. The readings were taken on the downside of revolution at locations where it was least likely to have mineral material on the opposite face of the refractory lining. Equation 2.23 was used for a minor correction incorporating the steel shell. The rotary kiln was shut down at a later date and the AU-E measurements were verified from the inside of the vessel using a covermeter. The sampling rate and data number used for the roof inspection was 500 kHz and 2048 points respectively. The impactor size used was 3 mm in diameter.

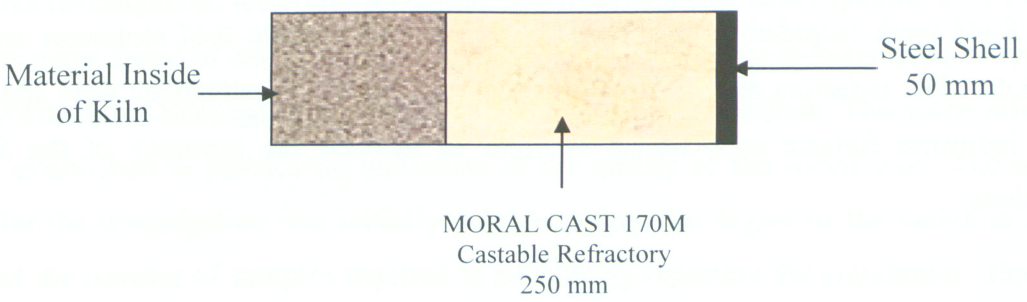

Figure 3.6: Kiln Wall Refractory Configuration

3.3.3 Investigation of a Furnace Roof #2

The final site investigation was conducted on a second furnace roof. The construction of the roof was slightly domed in shape consisting of 425 mm chrome-magnesium refractory bricks placed upright and adjacent to one another. The mid-span of the roof is also more susceptible to a sagging effect where build-up material may accumulate.

The objective of the AU-E inspection was to evaluate the condition of the refractory material in the roof and to quantify any build-up accumulation that may be present. Danger arises from the build-up material overloading the roof capacity. This is compounded with high temperature fluctuations causing cracking of the brick network. To quantify the build-up, multi-layer effects were considered in the evaluation at each station. Over 120 stations were evaluated in both time and frequency domains for the inspection. The sampling rate and data number used for the roof inspection was 500 kHz and 2048 points respectively. The impactor size used was 3 mm in diameter.

3.4 Chapter Summary

This chapter outlined the methods and procedures for the field work and laboratory experimentations conducted for the project. The laboratory testing included inspection of a bulk sample of newly manufactured bricks, testing of refractory specimens at high temperatures and the effect of high temperatures on concrete materials.

For the heating trials, consideration was made to avoid thermal shock within the materials and evaluation of the soak time was determined using transient heat flow methods. The heating trials provided stepwise evaluation of the α-factor.

Field work included the testing of two industrial furnace roof structures and a rotary kiln. The α-factors determined from the experimental investigations were applied to the industrial furnace applications in order to increase the accuracy of the field evaluations.

Chapter 4

Field Work and Laboratory Testing Results

4.1 Introduction

This chapter discusses the analysis and results of the various fieldwork and laboratory investigations outlined in the previous chapter. The experimental portion is discussed first. This included the evaluation of newly manufactured refractory bricks and the heating of various refractory and concrete materials. This is followed up with a small discussion using the finite element method to compute non-linear temperature gradients. Finally, the results for the experimental portion are applied to various in-situ applications.

4.2 Results of Laboratory Testing

The purpose of the laboratory work was to ultimately establish a temperature correction for the AU-E evaluation of industrial furnace linings. Evaluating the refractory materials at different temperatures in the kiln provided insight into the behaviour of the materials at a specific temperature. This allowed for a stepwise evaluation over a temperature gradient encountered in the field. As a supplementary investigation for the castable refractory materials, concrete samples were also tested at various temperatures using the AU-E technique.

4.2.1 Variability and Calculation Errors

For this investigation, the AU-E technique was used as a tool with Equation 2.19 to solve for the wave speed of newly manufactured alumina bricks. The α-factor used in this case is 1.0 due to the material being tested with no temperature gradient. The wave velocities were established to provide an indication of the quality of the specimens. The sample size for the investigation was initially unknown since the degree of the variation would impact the number of samples required to adequately represent the population. Equation 3.1 was used to determine the minimum number of samples required using a dynamic sample average and sample size. The desired level of confidence is 95% and the acceptable statistical error for the sample mean was chosen as 2% assuming normally distribution data.

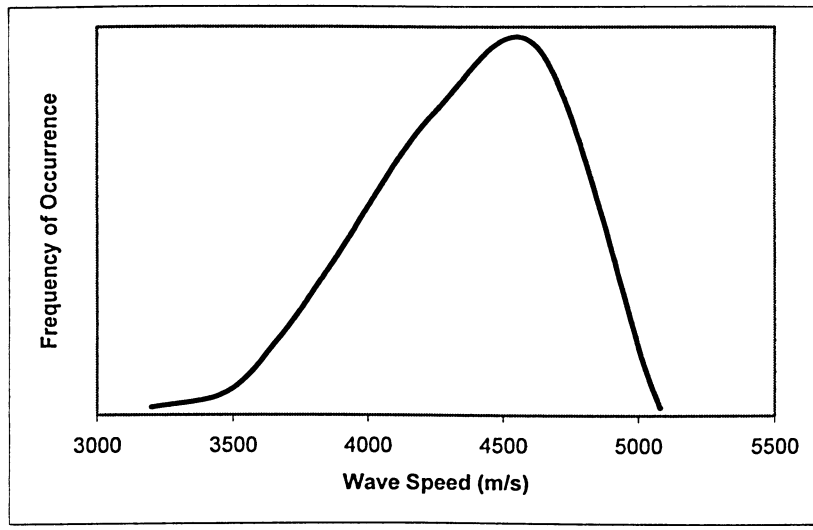

Figure 4.1: Wave Speed Distribution of Pallet Specimens

Figure 4.1 shows the different velocities and the occurrences for each value for a sample size of 325 bricks. The mean (m) and standard deviation (SD) for the sample population was 4370 m/s and 125 m/s respectively.

There are three main sources for the variation with in the samples namely; imperfections in the samples, different material properties and from the AU-E technique frequency resolution. The sampling rate and data number used here were 500 kHz and 2048 data points. This introduces a possible 144 Hz error which can be translated into a 126 m/s or 1.4% error at the 380 mm specimen depth. Using a typical maximum allowable engineering error of 5% based on Figure 4.1, the probability of having an error greater than this (including instrumentation error) is less than 4.8%. In terms of evaluating a furnace structure, the temperature correction factor α will bring the evaluation confidence level of a single reading to approximately 95%. By sampling multiple points on the furnace, the error generated by the variation in material properties can be ignored for this particular manufactured brick.

4.2.2 Heat Treatment of Refractory Materials

The AU-E technique was used to study the effects of the temperature in a controlled environment to aid in evaluating the α-factor in the field. The materials tested were a

firebrick, a cast-in-place refractory, a 70% alumina brick and a 90% alumina brick. The wave speed for each sample was monitored with changing temperature conditions.

The AU-E signals were analysed in both the time and frequency domain to monitor this wave speed change during the heating trials. The time domain provided insight into the attenuation or damping of the signal as the temperature increased. The attenuation coefficient is a measure of the decay of the stress wave or the decay of the free vibration within the sample (Thomas et al., 1999). Figure 4.2 shows an example of a time domain signal with the accompanying attenuation curve. Along with this, a typical frequency response is shown for a change in temperature. As the decay of the signal increases, the accompanying attenuation coefficient increases. The two main factors influencing the attenuation of a signal in any solid material is the degree of internal friction and the temperature. The internal friction includes physical attributes such as micro-cracking, the porosity of a material and slip plains or grain boundaries. The attenuation is eventually dissipated as heat (Kolsky, 1963). Increasing the temperature of the specimen will add to the kinetic energy of the matrix particles and interfere with the transmission of a propagating signal. This results in an energy dispersion phenomenon and thus increases the attenuation.

Typically, a shift in the frequency domain occurred indicating a change in material properties as the temperature increased. Figure 4.2 b) illustrates the possible shift in the frequency domain. The frequencies were input into Equation 2.19 to calculate the wave speed for each sample at different temperatures.

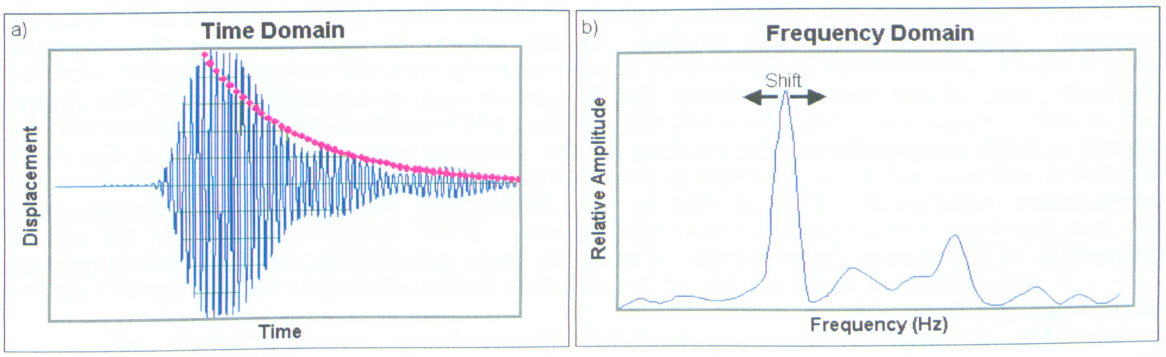

Figure 4.2: a) Time Domain Signal with Accompanying Attenuation Coefficient
b) Typical Frequency Response to Changing Temperature
(Thomas et al., 1999)

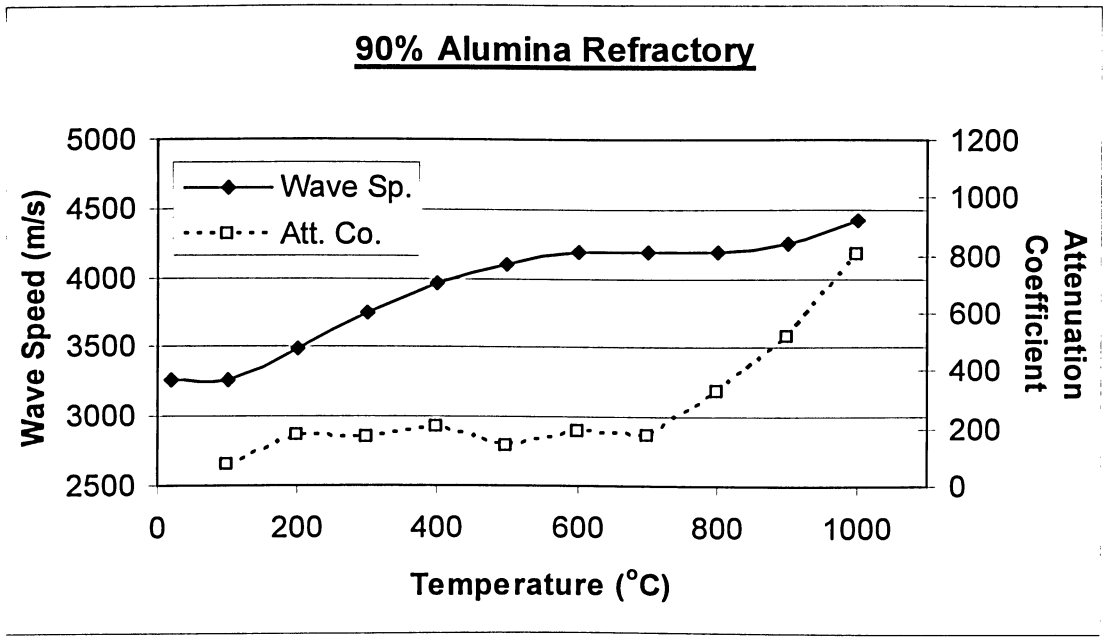

Figure 4.3: Wave Speed and Attenuation vs Temperature for 90% Al Specimen

Figure 4.3 displays the results for the 90% alumina specimens. The figure shows both the wave speed with respect to temperature along with the attenuation coefficient with respect to temperature. The wave speed increased with an increase in temperature. Chemically, there is little activity at the lower temperatures however; the data indicates the most activity in the leading up to 500°C. The manufacturing process yields this characteristic behaviour of certain high alumina refractories.

The sintering process, which can begin at temperatures as low as 900°C and can be as high as 1500°C for some materials, is responsible for the refractoriness of the material. Sintering forms the ceramic bonds, which in turn increase the strength, elasticity, etc. of the material. Since the formation and re-crystallization of the matrix occurs at high temperatures, the cooling of the material can sometimes affect the room temperature behaviour. This is due to the differential thermal expansion/contraction properties of the matrix constituents. There are three possibilities in the cooling process as outlined in Figure 4.4.

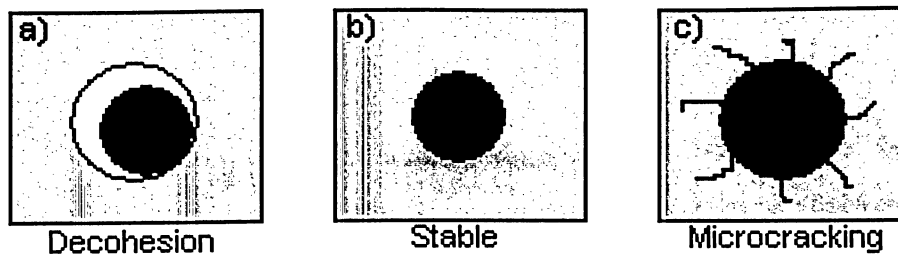

Figure 4.4: Thermal Expansion/Contraction Differences With Cooling

Figure 4.4 a) depicts the scenario where the individual grains have a higher coefficient of thermal expansion than the rest of the matrix. This increases the void space and results in a lower strength or lower elasticity value. This in turn lowers the wave speed within the material. Scenario b) in Figure 4.4 shows a scenario where the matrix components have similar thermal expansion coefficients. Here, the material will have an increase in strength or elasticity as the temperature reduces. Finally, scenario c) in Figure 4.4 depicts where individual grains have a lower coefficient of thermal expansion than the rest of the matrix. This will result in micro-cracking and will lower the strength or elasticity to an even greater degree than the decohesive scenario as shown previously by (Tessier-Doyen et al, 2004). In reality, a combination of the three scenarios will occur within any refractory matrix during cooling or heating.

The results for the 90% alumina brick can be explained by the differential thermal expansion coefficient theory. As the temperature increased, the expansion of the specimen began to close the micro-cracks and voids generated during the cooling process. The closing of the voids creates a closer packing of the matrix and reduces the porosity, which increases the strength and elastic properties of the material. From Figure 4.3, the attenuation remains almost the same while the wave speed increases. This is due to the closing of the void spaces and micro-cracks competing with the increase in kinetic energy up to 700°C. Beyond 700°C, most of the matrix packing is completed and the kinetic energy begins to govern which is indicated by the increase in attenuation.

The firebrick wave speed results were also compared with the attenuation coefficient. The behaviour is different than that of the high alumina material mainly due to the high percentage of silica which is common in all fire bricks. Table 4.1 lists

examples of various castables, concretes and fire brick along with their mineralogical components.

Table 4.1: Mineral Constituents for Cement, High Quality Castables and Fire Brick

Compound	High Alumina (% wt)	High Magnesia (% wt)	Fire Brick (% wt)	Portland Cement (Mindess et al.)
Al_2O_3	98	0.2	40.1	6.2
SiO_2	2	1.2	50.7	21.0
CaO	Trace	3.3	0.3	64.7
MgO	Trace	95	0.1	2.6
Fe_2O_3	Trace	0.2	0.7	2.6

Figure 4.5 displays the results for the fire brick specimens. The figure shows both the wave speed with respect to temperature along with the attenuation with respect to temperature. From the figure, the wave speed increases up to approximately 500°C at which point a sudden drop is encountered. The curve then plateaus around 700°C. Values above 900°C were unable to be taken due to the resulting high contact time at these temperatures as a result of the material softening.

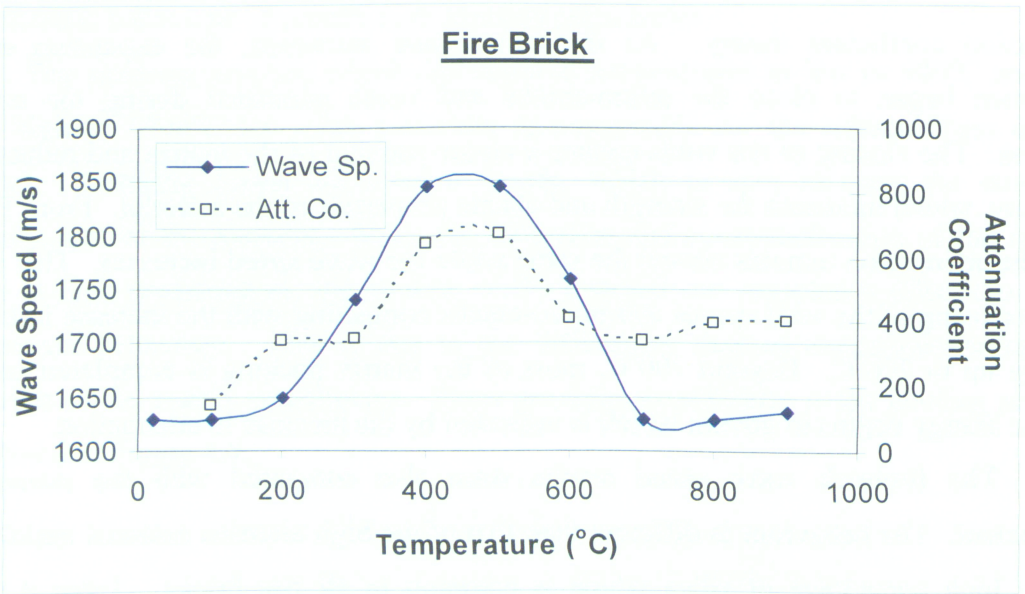

Figure 4.5: Wave Speed and Attenuation vs Temperature for Fire Brick Specimen

The long contact time does not generate frequencies high enough for useful evaluation. This is illustrated by the relationship in Equation 2.14.

The increase in wave speed approaching 500°C in Figure 4.5 is due to a re-crystallization of the silica within the matrix. This is explained using Figure 4.6 detailing polymorphic forms of silica. The common constituent which makes up the high amount of silica in a fire brick is quartz. The exact activation temperature for the transformation from low to high quartz is influenced by other constituents within the matrix but is typically around 573°C. The crystal transformation is displacive in and around 500°C. The transformation from high quartz to high tridymite is a reconstructive transformation of the crystallography and yields no significant volume change. During the manufacturing process, the quartz component may in fact be heated to the tridymite formation temperature. The cooling would result in the formation of medium and low tridymite. The low-medium-high tridymite transformation is displacive but not to the same degree as the low-high quartz transformation.

The increase in wave speed in Figure 4.5 up to 500°C is due to the expansive transformation of the quartz or tridymite filling voids from the cooling process. Once the transformation is complete, the high temperature softening begins to govern and thus lowers the wave speed beyond 500°C.

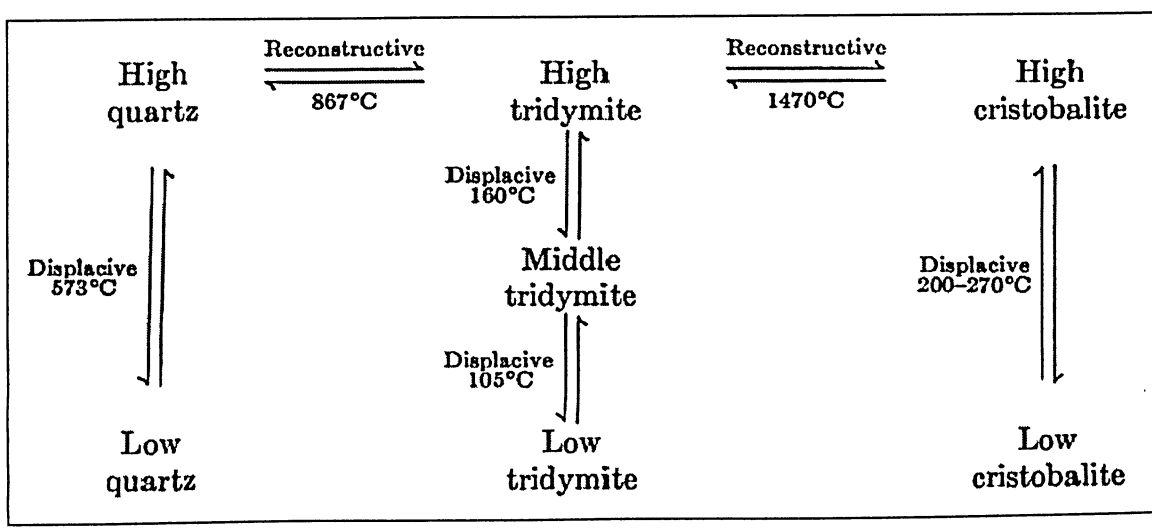

Figure 4.6: Polymorphic Forms of Silica (Kingery et al, 1976)

The explanation for the plateau around 700°C is difficult to explain since any reconstructive crystallographic transformation does not involve a volume change. The reconstruction may however be interfering with the softening mechanism since new bonds are being formed.

Unlike the 90% alumina specimens, the attenuation of the fire brick does increase with the temperature increase. This is due to the relatively low comparative wave speeds of the materials. The fire brick is by definition a weaker and far less dense material compared to the alumina bricks. So the expansive changes in the silica do not govern the behaviour as much as the alumina materials. However, once the expansive changes in the silica are complete, the attenuation does drop beyond 500°C. The plateau around 700°C for the attenuation again may be a result of the reconstruction of the crystallography interfering with energy absorbing tendencies of the high kinetic energy since new bonds are being formed.

Figure 4.7 displays the results for the 70% alumina brick heating trials. The wave speed remained constant up to 400°C at which point it began to increase almost linearly up to 900°C. The increasing wave speed is characteristic of high alumina refractory materials. The plateau and sudden change in slope may be a result of rapid cooling after the sintering process where significant micro-cracking occurred.

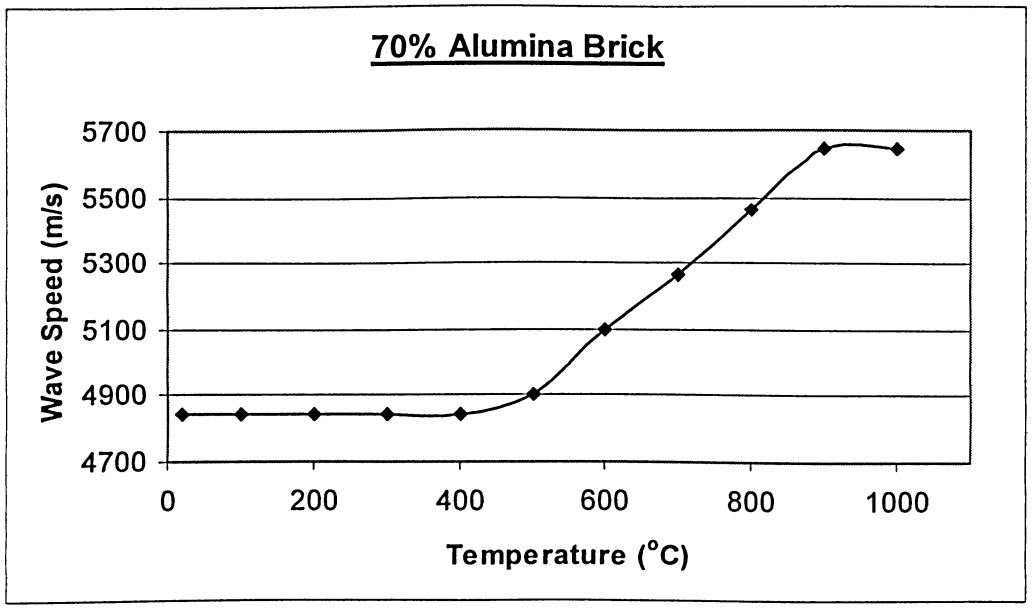

Figure 4.7: Wave Speed vs Temperature for 70% Alumina Brick (Hanger Brick)

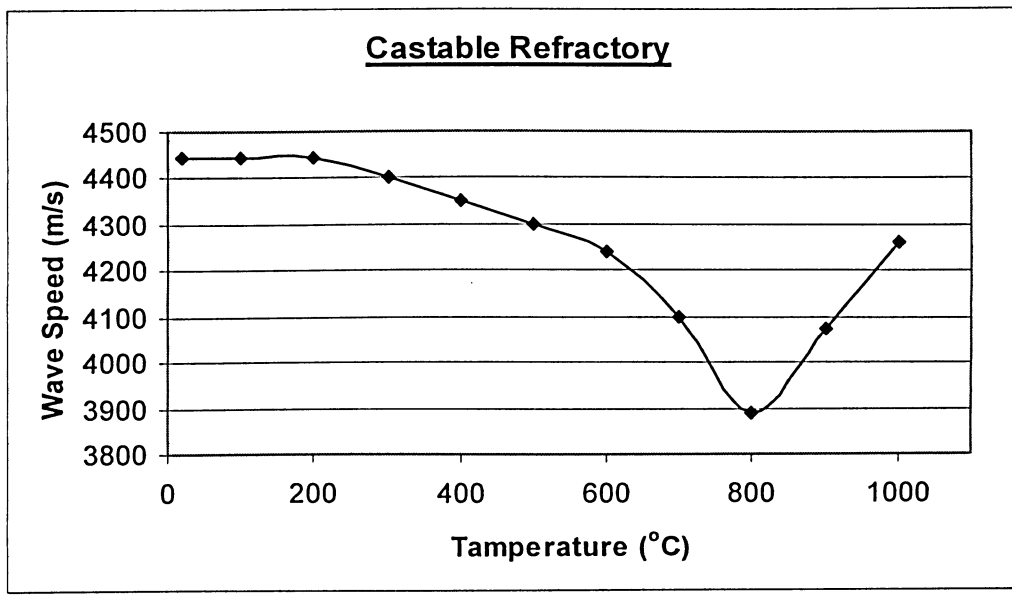

Figure 4.8: Wave Speed vs Temperature for Castable Refractory (Rotary Kiln)

The cast in place material tested in these particular heating trials was an unsintered sample. All castables rely on cementatious materials to bind the matrix together prior to the sintering stage where the ceramic bonds take over. The decrease in wave speed is a result of the dehydration of hydration products in the material matrix. The existing matrix was formed while the material was cool so in this case, the increase in temperature causes differential expansion resulting in micro-cracking which further reduces the wave speed. This reduction continues up to 800°C where the ceramic bonds begin to form. Once ceramic bonding (sintering) begins to form, the elasticity (or wave speed) begins to increase rapidly which is in agreement with Cutard et al, 2004. Example mineralogical constituents for cast-in-place refractories are shown in Table 4.1. To the determent of all cast-in-place refractories, the temperature gradient will inevitably produce a layer of the lining in the industrial application with a low quality material corresponding with the 800°C point in Figure 4.8.

4.2.3 Finite Element Modeling

The purpose of using the finite element method as a tool was to attempt to verify the temperature gradient encountered in the field applications. The software package used

for the simulation analysis was Abaqus. Assumptions made for the heat transfer model are that a steady state condition and a one dimensional heat flow condition are present. The steady state condition is acceptable because the working furnace is kept at a minimum idle temperature above 1200°C. One dimensional heat flow is acceptable based on the geometry of the furnace. The roof, wall, etc. are plate-like having the geometry significantly different in one of the dimensions.

The boundary conditions for the model had specified temperatures at the two ends of the specimen and the four remaining sides of the specimen are insulated forcing the heat flow to propagate in one direction. The end conditions are the measured temperatures at the inspection site. For constant thermal conductivity, the temperature gradient would be linear and a finite element model would not be necessary. However, the material thermal properties change with temperature. So the initial condition has the temperature profile as liner. With successive iterations of the program, the temperature profile changes eventually converging to a unique profile based on the thermal parameters. These parameters are the thermal conductivity, the specific heat and the density of the material. All of these parameters vary with temperature to some extent. The variation in density is minimal and is neglected. The variation in specific heat and thermal conductivity can be substantial. The specific heat is more of a concern when considering transient situations where the time of the heat flow is critical. For the purpose of this model, the amount of time to the convergence of the gradient is not considered critical. The number of time steps in the model is sufficient enough to allow convergence. Therefore, the specific heat of the material is kept at a constant value. Thermal conductivity values at specific temperatures from Figure 1.6 were input into the model. Figure 1.6, shows the material is a better insulator at higher temperatures. This will produce a greater drop in temperature across the gradient boundary. The finite element model will quantify the drop in temperature incrementally through the specimen.

For the heat transfer model, a solid eight noded brick element or hexahedral class element was used in generating the mesh. Other solid elements were considered such as four node tetrahedron element, however the hexahedral element produces more accurate results in this situation for this simple geometry.

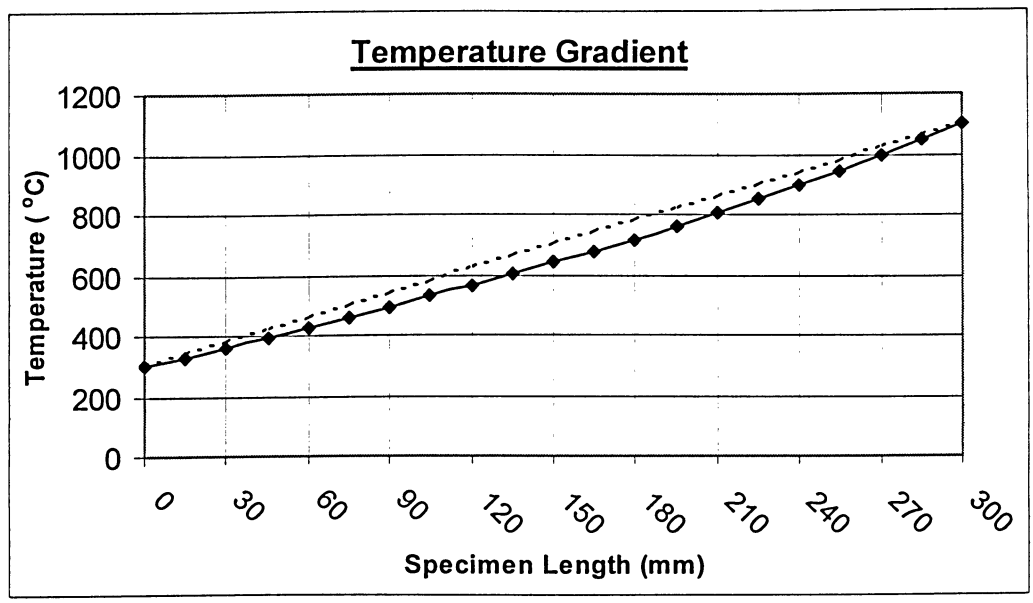

Figure 4.9: Temperature Profile Produced by the Model

The length of the specimen used in the model is 300 mm and a corresponding mesh size producing 10 elements along the length. An output at the corresponding nodes produced a temperature gradient with 20 intervals. The boundary temperature conditions used in the model were 1100°C and 300°C, respectively. The temperature values produced are plotted against the length of the specimen to generate the temperature profile shown in Figure 4.9.

Figure 4.9 illustrates the temperature profile through the model and the dashed line represents a true linear profile. The thermal conductivity data used for the model drops approximately 60% between the boundary temperatures. As the temperature gradient is reduced the nonlinear curve approaches a linear situation. An abrupt change in the thermal conductivity will have a larger bearing on the nonlinearity of the profile. This is either a case where two dissimilar materials have an interface or a case where contact resistance is an issue. As shown by Figure 4.9 the non-linearity of the temperature gradient is slight. For this reason, the assumption of a linear profile in general does not introduce a significant error.

4.2.4 Heat Treatment of Concrete Samples

To complement the evaluation of cast in place refractories, the deterioration of concrete specimens at high temperatures provides information of the transition or unsintered layer. The hydration of dicalcium silicate and tricalcium silicate in Portland cement produces calcium-silicate-hydrates and calcium hydroxide. During the heating process, the chemically bonded water is liberated from these hydration products. The activation temperature for the release of chemically bound water in the calcium hydroxide varies from 300°C to 400°C but can be explained by the interaction of other matrix constituents such as calcium-silicate-hydrate (Williams et al, 2003). However, most of the water in the calcium hydroxide is released by 550°C. The liberation of chemically bound water from calcium-silicate-hydrates is progressive up to 800°C where most of the water has been released (Handoo et al, 2002). The volume content of the calcium hydroxide in a normal strength concrete paste is 20-25%. The sudden decomposition of calcium hydroxide produces considerable damage. The interfacial zones are comprised mostly of calcium hydroxide. This causes the decohesion effect with an increase in temperature as *outlined in the previous section.*

The pozzolanic reactions found in high strength concrete tend to consume calcium hydroxide and produce more calcium-silicate-hydrates. The calcium-silicate-hydrates are still susceptible to high temperature damage but the effect may be more spread out up to 800°C as apposed to 550°C. The varying thermal expansion coefficients produce cracking of the matrix as outlined by (Culfik and Ozturan, 2002). By adding fines containing graphite, the specific heat of the material is reduced and the thermal conductivity is increased. This lowers the effect of differential thermal expansion and therefore reduces the amount of cracking caused by expansive forces in the matrix (Culfik and Ozturan, 2002). Aggregates have an effect on the performance of concretes at high temperature. Aggregates with a high amount of quartz will exhibit the expansive characteristics discussed in the previous section. The crystallographic transformation occurs in and around the same temperatures where the calcium hydroxide is liberating a significant amount of water. Due to the localized positions of aggregates, the expansive characteristics of the quartz will not be compensating in this case and will be more deleterious.

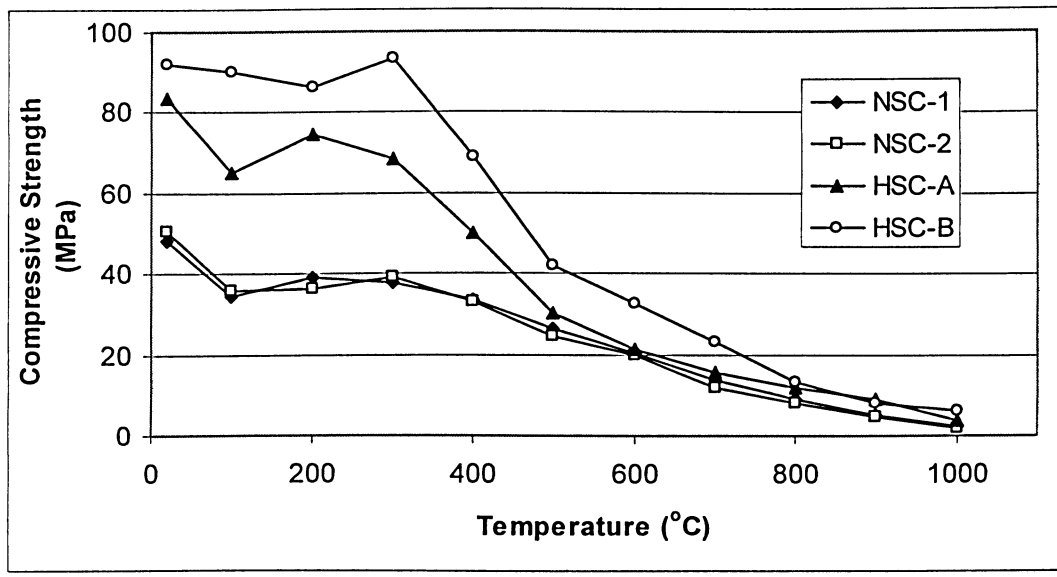

Figure 4.10: Residual Compressive Strength versus Exposure Temperature

The results for the residual compressive strength are displayed in Figure 4.10 for the various concrete samples tested in the laboratory. As expected, the residual compressive strength decreased as the exposure temperature increased. The normal strength concretes (NSC-1 and NSC-2) showed similar results. The high strength concrete mixes (HSC-A and HSC-B) varied slightly in strength due to the differences in the initial mix. All materials show a slight reduction followed by a slight return in strength. The loss of free water at the early stages of heating produces drying shrinkage causing some micro-cracking. This strength loss is then compensated for by the closer packing of the matrix increasing Vander Waal forces (Mindess et al, 2003). The low porosity of the HSC mix allows some of the free water vapour to be contained within the specimen producing a localized autoclave effect. This allows some of the unhydrated cement to react forming some new hydration products at the higher temperatures in essence repairing some of the high temperature damage (Xu et al, 2001). This accounts for the maximum compressive strength of HSC-B occurring at 300°C. This localized autoclave effect is only possible due to the extremely low heating regime used for these particular tests.

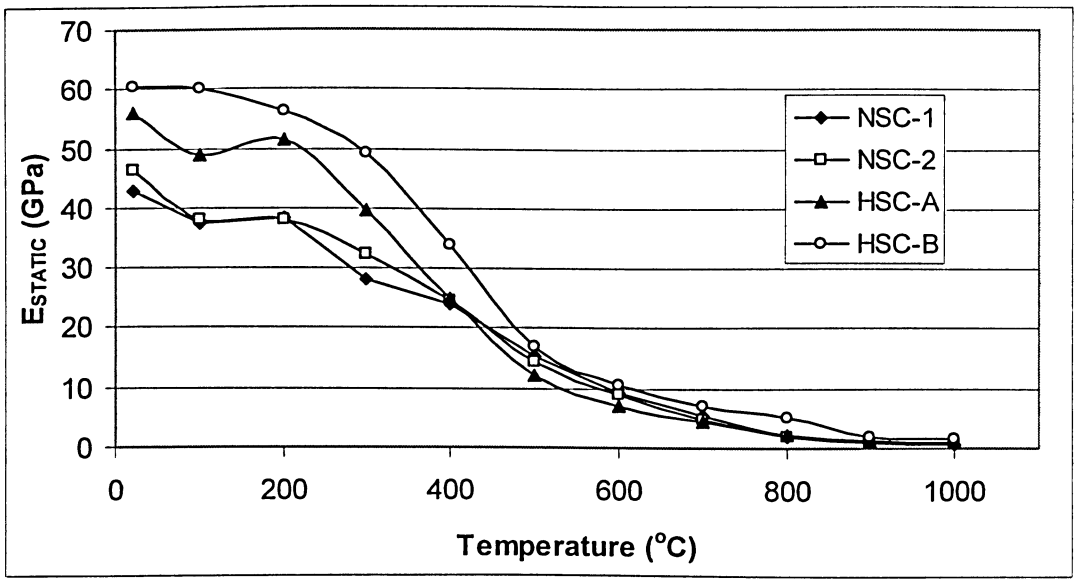

Figure 4.11: Residual Static Modulus of Elasticity versus Exposure Temperature

The residual static modulus of elasticity results are displayed in Figure 4.11 for the concrete samples tested in the heating trials. In general, the static elastic modulus values decrease with increasing temperatures. Although there is a relationship between the elasticity and strength, the increase in compressive strength is not mimicked by the static elastic values. The HSC performed slightly better up to 500°C where the values tend to match in behaviour up to full disintegration of the matrix.

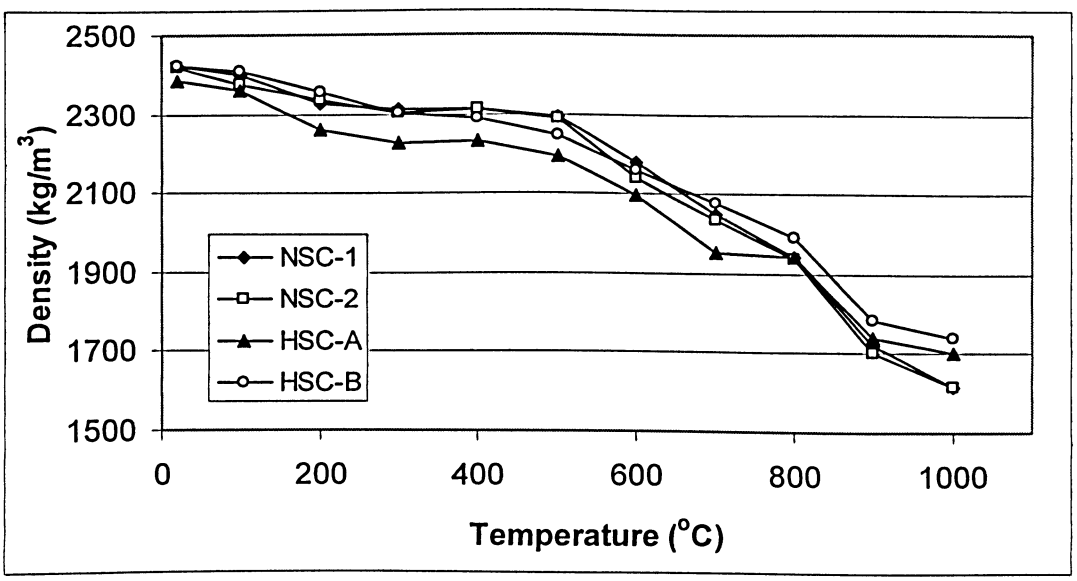

Figure 4.12: Residual Density versus Exposure Temperature

Figure 4.12 displays the evolution of the mass loss for the various mixes during the heating trials. The density of the various mixes does not vary significantly. The abrupt change in the curves occurs at 500°C indicating a sudden loss of mass. This is due to the decomposition of the calcium hydroxide.

The residual wave speed decreases almost linearly as the exposure temperature increases. The mechanism for the reduction in wave speed is due to the disintegration of the matrix. The results for the residual wave speed versus the exposure temperature are shown in Figure 4.13. The residual dynamic elastic values are shown in Figure 4.14 are determined using Equation 2.2. Both the wave speed and density are used to generate the dynamic elastic values. There is significant reduction of the dynamic elastic values up to 700°C.

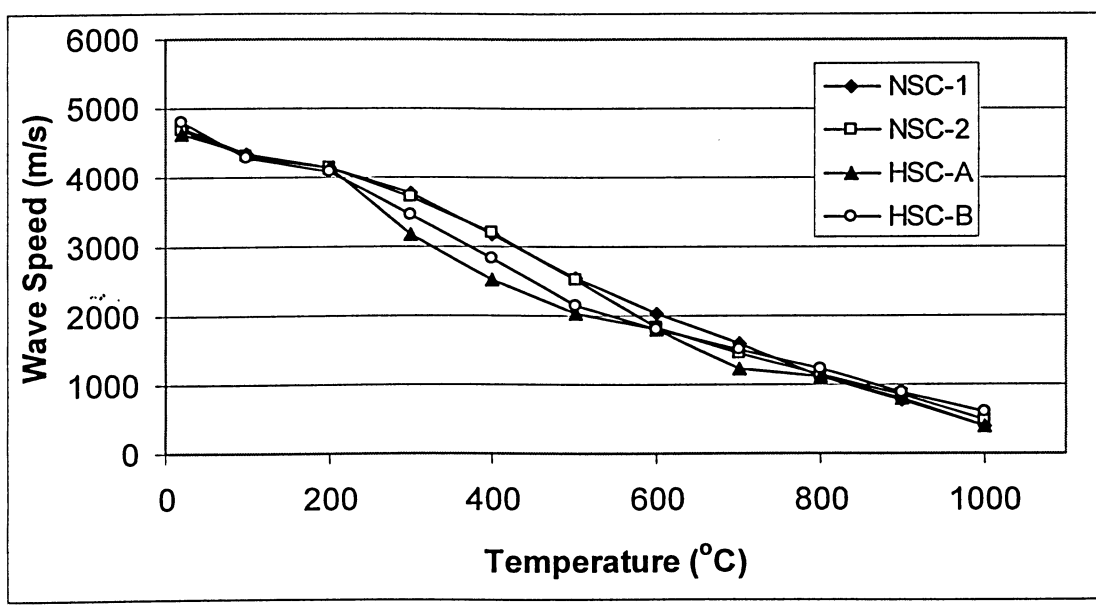

Figure 4.13: Residual Wave Velocity versus Exposure Temperature

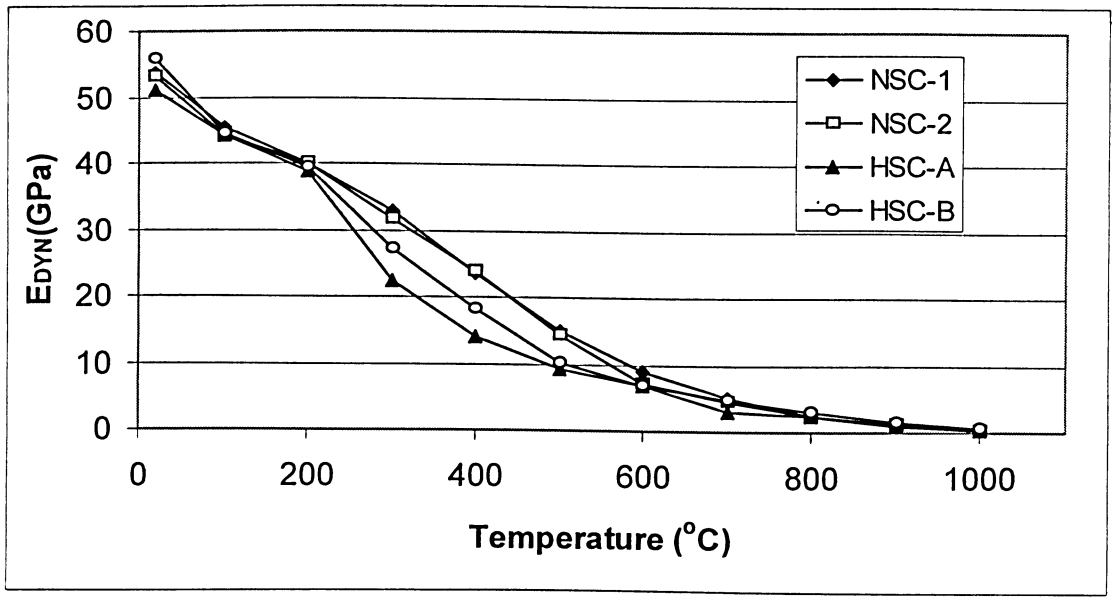

Figure 4.14: Residual Dynamic Modulus of Elasticity versus Exposure Temperature

Figure 4.15 displays the results for the wave speed in the concrete specimens while at the exposure temperature. This differs from the residual properties where up to this point the specimens were exposed to various temperatures and allowed to cool back to room temperature.

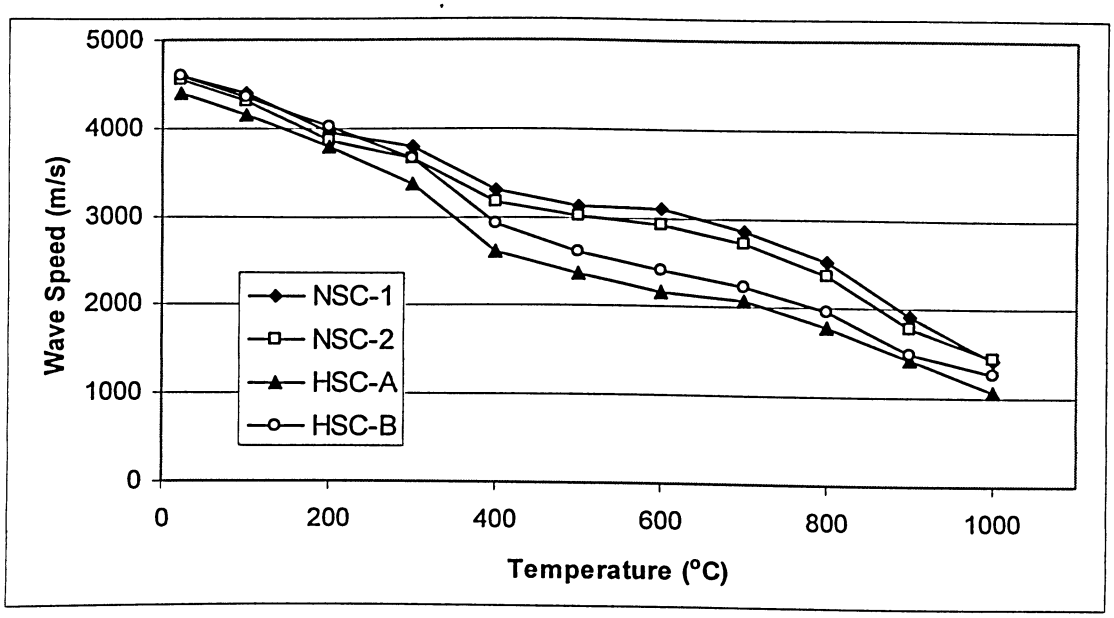

Figure 4.15: Wave Speed at Exposure Temperatures

This data provides some insight into the behaviour of a concrete during a fire for example as apposed to after a fire. The wave speeds are slightly higher at the actual exposure temperatures compared to the room temperature values.

For a comparison of the residual wave speeds and the high temperature wave speeds, Figure 4.16 displays the ratio of the hot wave speed to the residual wave speed with changing temperatures. The wave speeds match up to 400°C where the "hot" wave speeds begin to diverge from the residual values. This is due to two factors. First, some of the thermal damage is a result of the heating and cooling cycles. While at the high temperature, the material has only been affected by the heating portion of the cycle only. The cooling half of the cycle will produce some further micro-cracking. The second factor is the reintroduction of moisture into the cooled concrete matrix. This creates wedge action within the newly generated pore voids, weakening the cohesive forces in the matrix. In addition, some dissociated calcium hydroxide in samples with a 400°C exposure temperature or higher is re-hydrated producing a 44% volume increase (Xu et al, 2001). This will cause sever damage and the phenomena increases with maximum exposure temperature.

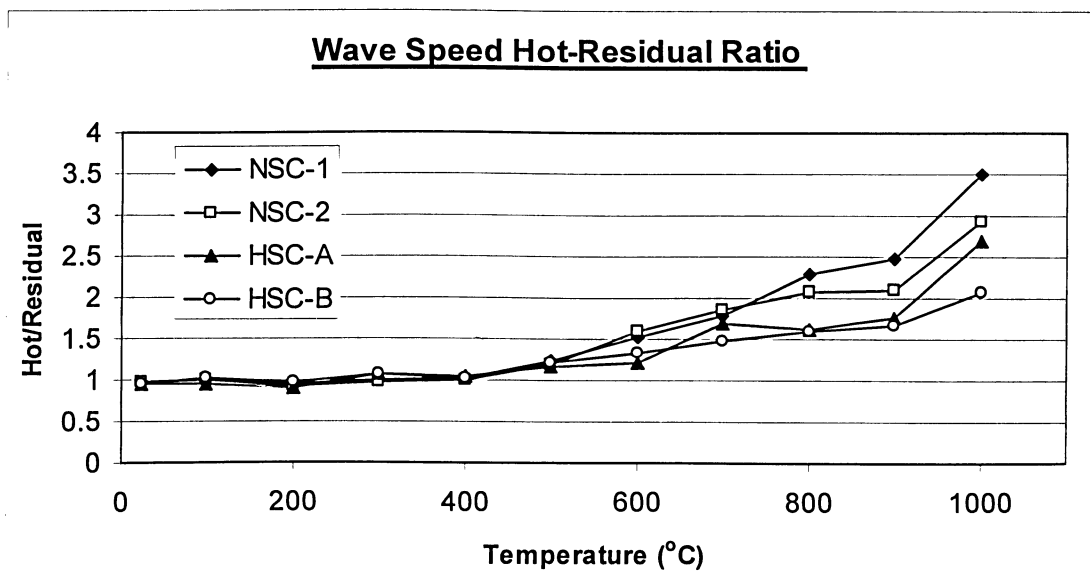

Figure 4.16: Wave Speed at Exposure Temperatures to Residual Wave Speed Ratio

Figure 4.16, shows that the HSC samples will actually perform comparatively better while at high temperatures. NSC-1 performs 3.5 times poorer to values of the same specimen once cooled and exposed to a moisture rich environment. This would suggest that a concrete structure subjected to a fire would be more susceptible to collapse after the fire compared to during.

Figure 4.17 shows samples exposed to 1000°C which were allowed to cool in air with 80% relative humidity. Wedge action of the water has disintegrated the NSC samples in the picture.

Figure 4.17: Re-hydration of Specimens Exposed to 1000°C

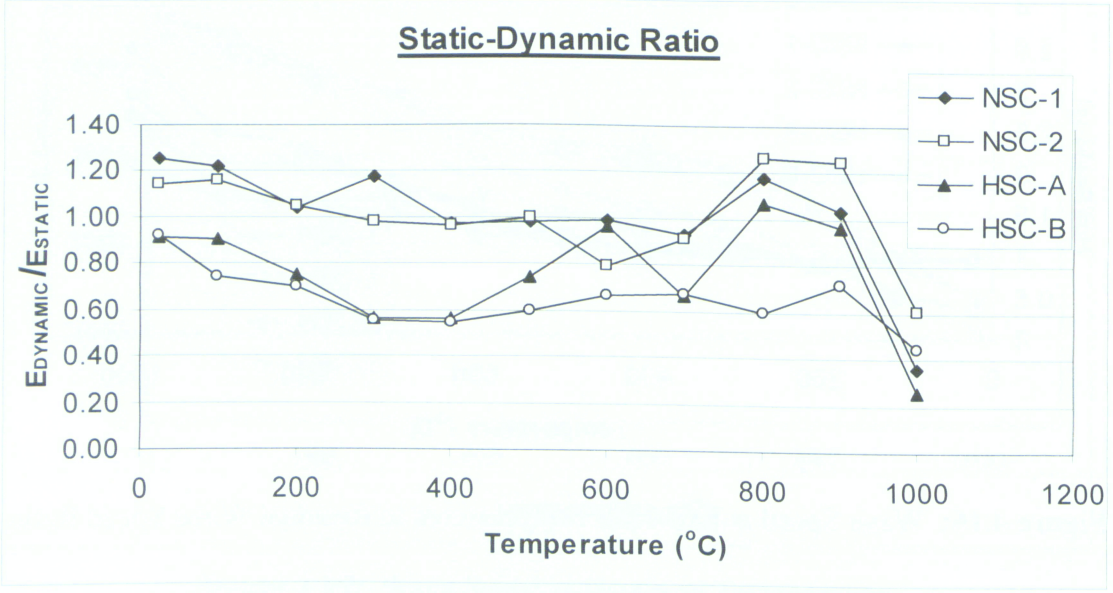

Figure 4.18: Static-Dynamic Elasticity Ratio

Figure 4.18 displays the ratio of static elasticity to dynamic elasticity versus temperature. The sudden drop in the ratio at the high temperature is due to the wedge action of the water rehydrating the matrix. In general, the ratio decreases up to 400°C after which the rehydration of the matrix produces unpredictable results.

The heating rate used for the concrete heat trials was 5°C/min. As outlined in Chapter 3, the slow heating rate was to avoid thermal shock in order to study the change in the microstructure without any significant structural cracking. Typically in the event of a fire, the heating rate is extremely high. The sudden rise in temperature will cause spalling of the concrete. High strength concrete is more susceptible to spalling due to the trapping and accumulation of vapour pressure associated with the low permeability under a large heating regime (Hernandez-Olivares and Barluenga, 2004). Polypropylene fibres are added to high strength concrete mixes to increase the fire resistance of the material (Bilodeau et al, 2004). The polypropylene fibres begin to melt at a temperature of 125°C. This increases the pore voids creating canals for the water vapour to escape. Shorter and finer fibres are more effective at the same %weight due to a better distribution within the cement matrix. The addition of fibres is also common in castable refractory applications.

High strength concrete samples containing polypropylene fibres and steel fibres were compared to the specimens without fibres in order to determine if the addition contributed to the protection of the concrete matrix. The results indicated no significant bearing on the residual material properties of the high strength concrete. The specimens containing the metal fibres showed an increase in micro-cracking compared to those without that particular fibre. The high temperatures caused oxidation of the metal. The expansive volume change of the oxidation process increased the degree of micro-cracking. The specimens containing polypropylene fibres did not show any benefit of this addition in the event of a high temperature exposure. This is likely due to the low rate of heating making the polypropylene fibres redundant. However, if the heating rate were higher, possible benefits would be more evident.

Comparatively, a concrete matrix has a significantly higher amount of hydration products within the matrix compared to a castable refractory. At high exposure temperatures a concrete will begin to develop some ceramic bonding due to sintering. The ceramic portion of the matrix is however overwhelmed by the void space created by

the loss of chemically bound water yielding the sintering effect negligible. The effect of sintering is also to reduce the free energy of closely packed grains (Kingery et al, 1976). This is not the case in a voided concrete matrix where high temperature exposure damage reduces the tendency of the sintering process.

4.3 Fieldwork Results

Using the results obtained from the experimental work, field investigations were conducted to apply the results. The industrial applications were the testing of two furnace roof structures and a rotary kiln lining. The AU-E technique was used as the evaluation method for all the industrial site investigations.

4.3.1 Results of Furnace Roof #1

The objective of the AU-E inspection was to determine the condition of roof anchor bricks in order to provide a structural assessment of the insulating system. For ease of the data representation, a critical crack depth had to be established. Considerations included the shear strength of the materials, the number of surrounding damaged bricks and the results from the study involving the variability of the manufactured bricks. Figure 4.19 illustrates the anatomy of the anchor brick along with the critical crack depth. The temperature of the hot face under normal operating conditions is 1400°C. Temperature measurements were taken on the outer face and were 300°C on average. This produced an 1100°C temperature gradient. The α-factor varies with depth due to the temperature variation along the gradient.

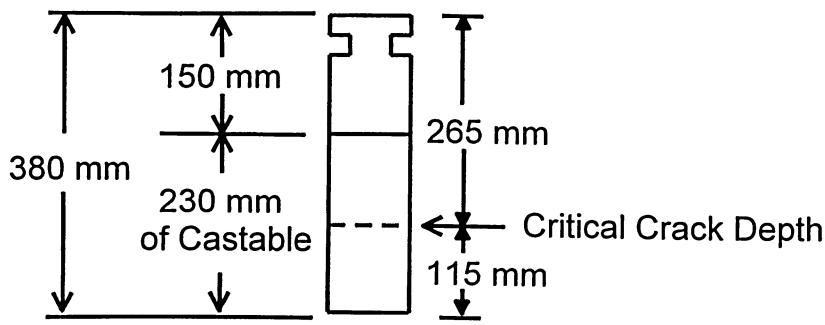

Figure 4.19: Dimensional Sketch of the Hanger Brick Showing Critical Crack Depth

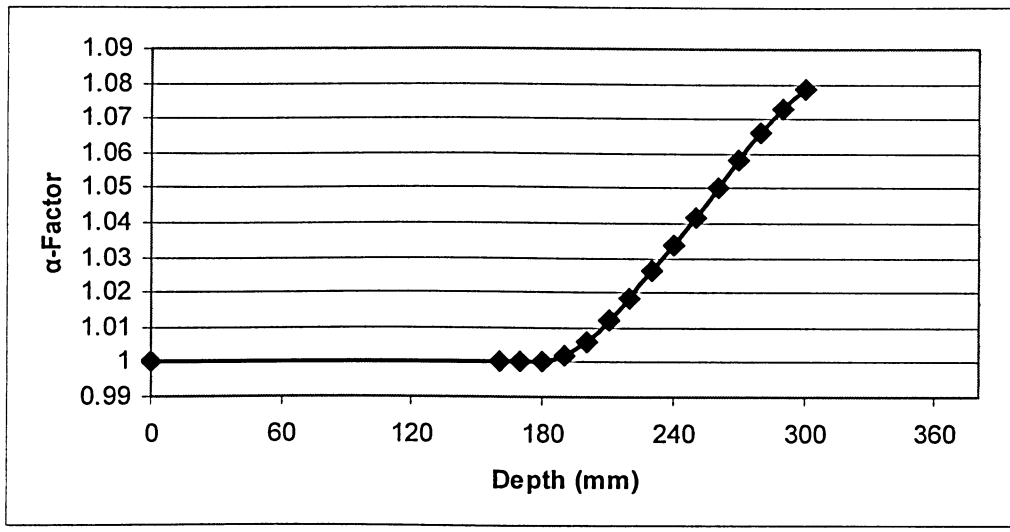

Figure 4.20: Dependence of α on the Depth for Hanger Brick Specimen

A stepwise procedure was used with the results obtained in the heating trials of the 70% alumina brick. The information was used in conjunction with Equations 2.20 and 2.21 to produce the α-factor with respect to the depth of the hanger brick. This is shown in Figure 4.20.

The evaluation of the signals is slightly iterative. Using Equation 2.19, an initial depth can be calculated. Once the depth is established, Figure 4.20 can be used to estimate the α-factor. Two or three iterations quickly produce converged results. Figure 4.20 is only valid for a specific temperature gradient. If other gradients exist as indicated by thermal measurements, different α-factor graphs should be produced for these areas.

There were three classes for the hanger brick evaluation. These classes are illustrated by the example spectrums in Figure 4.21. The first class is the case where the brick indicated full thickness and is shown in the first example spectrum. The second class is where the full thickness of the brick is detected but a secondary peak is indicating a crack. The third case is where the brick is cracked and the crack is significant enough to not allow the transmission of the signal beyond this point. This is shown in the third example spectrum.

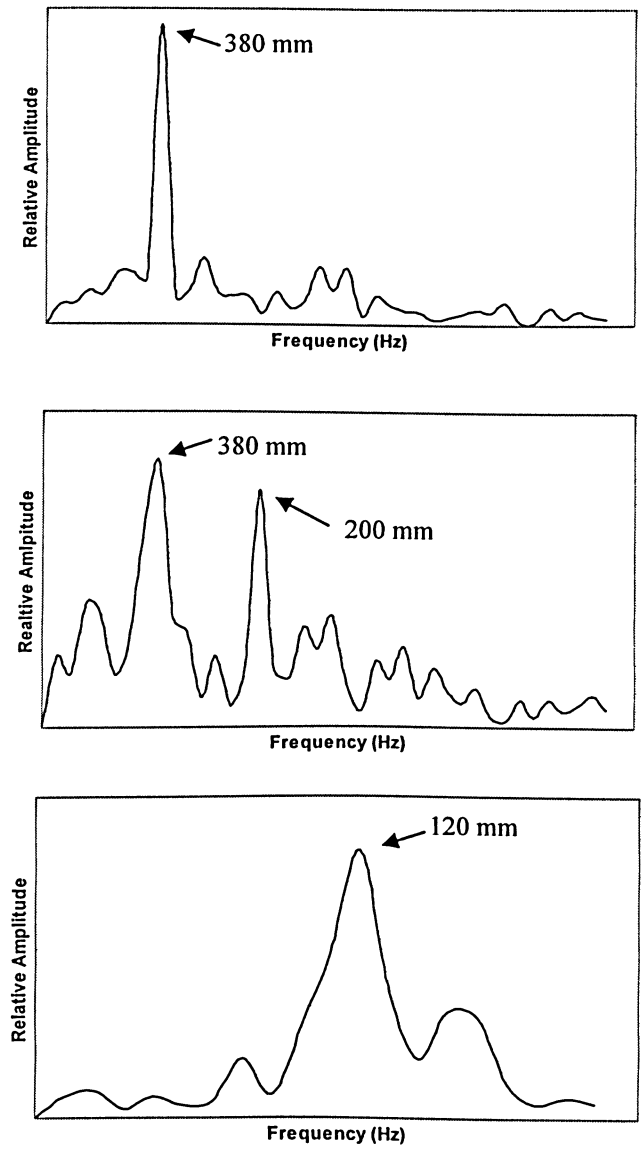

Figure 4.21: Example Spectrums Generated from the AU-E Signals

A small section of the roof was tested during a shut down in order to directly quantify the α-factor. The results varied slightly from those calculated form the laboratory findings. In some cases the discrepancy was from the new cracks forming between surveys. The hot values were taken initially followed by the cold. The cooling rate affects the degree of micro-cracking and the formation of new cracks produces difficulty establishing and shift in the frequency due to temperature. A further source of the discrepancy is from the spalled areas.

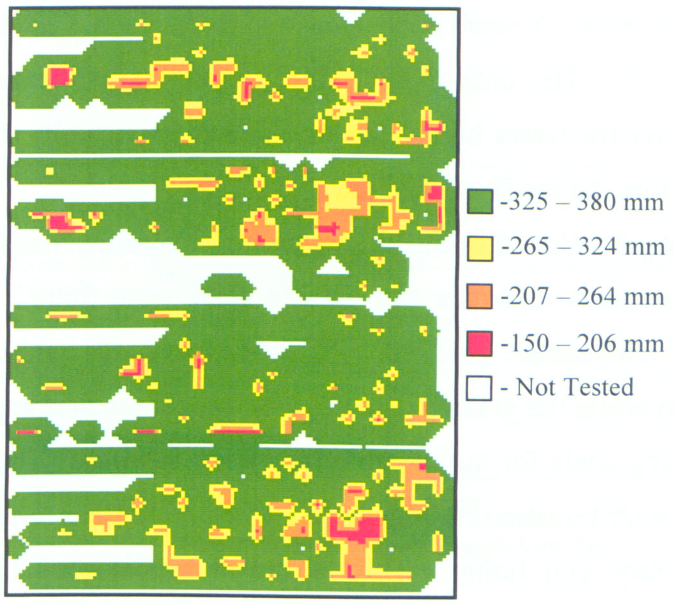

Figure 4.22: Contour Diagram Showing AU-E Results

The spalling dramatically changes the temperature gradient (as does the formation of new cracks) and renders the comparison impossible at these locations.

The results of the inspection are displayed in Figure 4.22 using the α-factor contribution. A contour diagram shows the areas of comparative damage. The green areas indicate sufficient brick thickness. Areas showing yellow, orange and red are progressively poorer areas. The white areas were not tested. The information provided by the AU-E survey emphasised critical areas which were selected for repair during a shutdown of the furnace. Less damaged area were left for future repairs.

The errors that would have existed without the application of the α-factor would have been an underestimation in thickness for this particular material which would have shown the lining to be in a much poorer state than what actually existed.

4.3.2 Investigation of a Rotary Kiln

The procedure for investigating the rotary kiln lining is similar to the furnace roof investigation. The lining in the rotary kiln is subjected to cyclic loading due to the turning action and fatigues the lining over time. During the sintering process, shrinkage occurs which is restrained by anchoring rods on the shell. The shrinkage causes cracking

of the lining in some areas. A small correction was made for the steel shell in this case by using Equation 2.23. The time of the AU-E inspection was conducted close to a scheduled shutdown for the rotary kiln. This provided an opportunity to check the results using a covermetre from the inside of the kiln.

The temperature inside the kiln under normal operating conditions is 1500°C. Temperature measurements taken on the outside shell were 300°C on average. This produced a 1200°C temperature gradient. The α-factor varies with depth due to the temperature variation along the gradient. A stepwise procedure was used with the results obtained in the heating trials for the castable refractory samples. The information was used in conjunction with Equations 2.20 and 2.21 to produce the α-factor with respect to the depth of the rotary kiln lining. This is shown in Figure 4.23 for the 1200°C temperature gradient.

Figure 4.24 displays the results comparing the AU-E signals to the covermeter data using the temperature correction data in Figure 4.23. In general, the signals matched. Approximately 70% of the readings matched within 15 mm. There are two types of discrepancies in the data. The first is where the AU-E signals are indicating thicknesses greater than the covermetre and second, where the AU-E signals are indicating thicknesses less than shown by the covermetre.

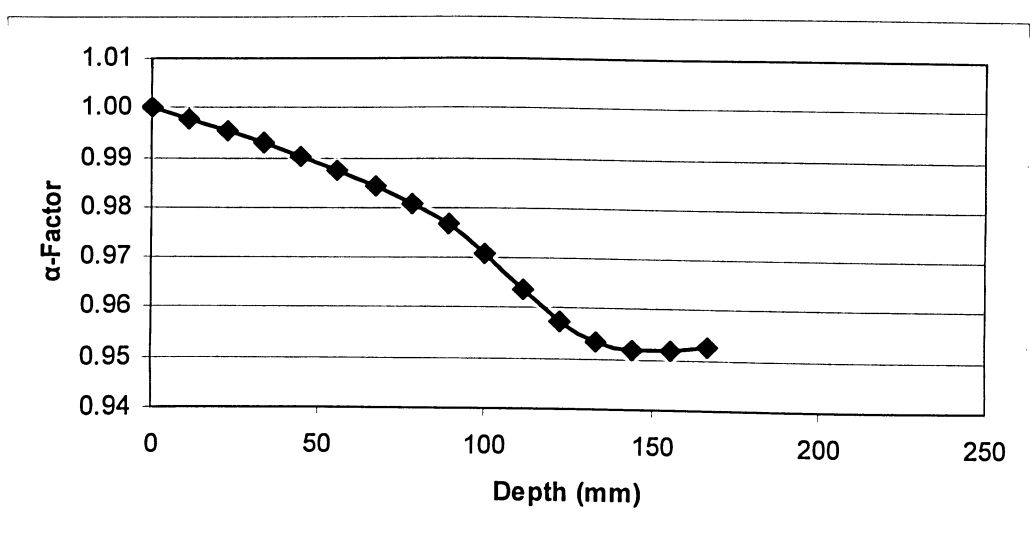

Figure 4.23: Dependence of α on the Depth for Rotary Kiln Castable

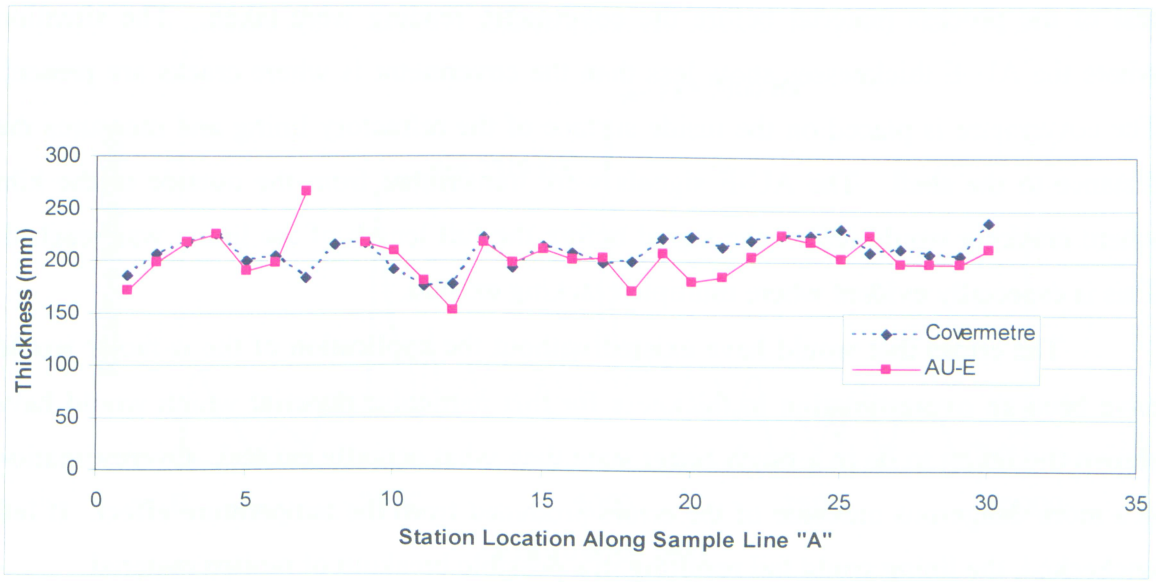

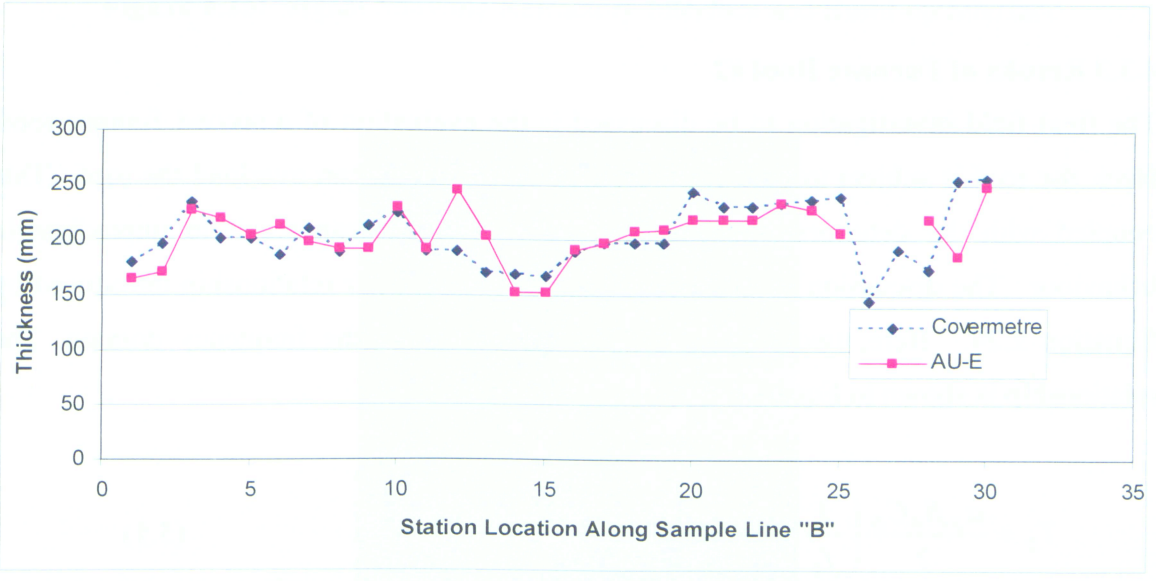

Figure 4.24: AU-E and Covermeter Comparison Along Sample Lines "A" and "B"

Under normal operating conditions, build-up material adheres to the inside face of the refractory lining. If the build-up material is well bonded to the lining face, then the AU-E signal can detect this and is incorporated into the thickness readings. Plant personnel use the build-up information from the AU-E technique to monitor the process conditions and can adjust the temperature accordingly to add or remove build-up. This information provides insight which can allow adjustments being made to yield greater production output. The discrepancy arises from the removal of the build-up material along with the

rest of the process material before the covermetre reading were taken. The situation where the AU-E thicknesses show less than the covermetre is where cracks are present. The covermetre is placed on the inside surface of the refractory lining and measures the distance to the shell. The AU-E signals were transmitted from the outside of the kiln where cracking would reflect the signal before the full length of the lining was reached. This is especially evident where multiple cracking existed.

The errors that would have existed without the application of the α-factor would have been an overestimation in thickness for this particular material which would have shown the lining to be in a much better state than what actually existed. Overestimation is a more dangerous outcome of the errors produced from the temperature effect. If left unchecked, the lining could fail resulting in a possible breakout of molten material

4.3.3 Results of Furnace Roof #2

The final field investigation to be discussed is the evaluation of a second furnace roof. Here, the roof is subject to accumulation of build-up which can overload the roof. This coupled with the deterioration of the refractory material can result in unpredictable behaviour. The discussion illustrates the use of the multilayer relationship introduced by Equation 2.24. Here, two frequencies are selected from the frequency domain. The relationship is shown in Equation 5.2.

$$T_B = \frac{\alpha_B \beta_B C_B}{2}\left(\frac{1}{f_T} - \frac{1}{f_R}\right) \tag{5.1}$$

where T_B is the build-up thickness, f_T and f_R are the frequencies of the total thickness and refractory thickness respectively. The α-factors for each material at the corresponding depths are α_B and α_R. The α-factor used for the refractory is very close to 1.0 due to the build-up interfering with the heat transfer and is omitted from Equation 5.1. The refractory thickness can be evaluated independently from the build-up which is the single layer equation. A sample signal is shown in Figure 4.25 showing a frequency corresponding with the refractory interface and a signal corresponding with the build-up interface. The results for the roof were verified during demolition.

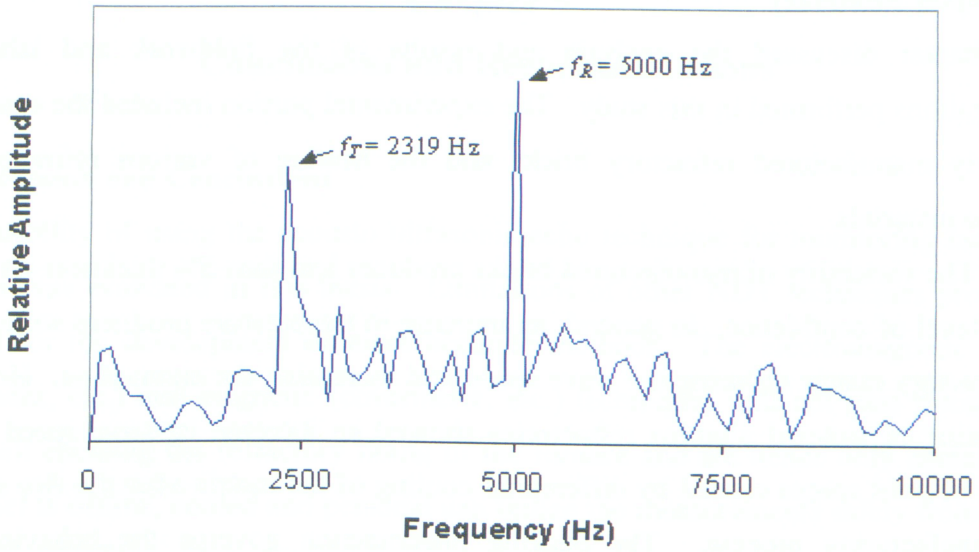

Figure 4.25: Signal Showing Refractory Interface and Build-up Interface

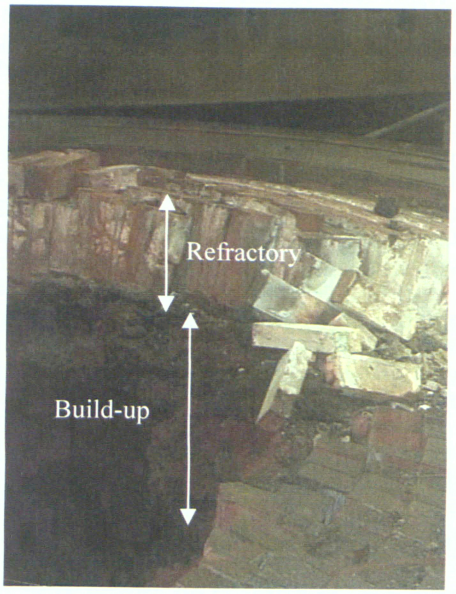

Figure 4.26: Refractory Thickness and Build-up

Once the thickness of the build-up approached a critical thickness, the furnace was shut down and repaired to avoid an unexpected failure. Figure 4.26 shows a picture of the demolition of the roof which shows the refractory thickness along with the build-up.

4.4 Chapter Summary

This chapter discussed the analysis and results of the fieldwork and laboratory investigations performed in this study. The experimental portion included the evaluation of newly manufactured refractory bricks and the heating of various refractory and concrete materials.

The variability of manufactured bricks produces less than 5% thickness error with a 95% level of confidence. In general, an increase in temperature produces softening of the refractory matrix reducing the wave speed and increasing the attenuation. However, the heating of sintered alumina refractories showed an increase in wave speed due to closing of void spaces caused by differential cooling of the matrix after the fire stage of the manufacturing process. The packing phenomenon governs the behaviour and produces an apparent increase in wave speed or elasticity. Castable refractories typically have a week zone where the hydration products have been lost and the temperature was not adequate for sintering from the vessel. The finite element models quantified the effect of temperature dependent thermal conductivity which produced a non-linear temperature gradient.

The results of the concrete testing indicated a decrease in strength, elasticity, mass and wave speed with an increase in temperature. The concrete performed comparatively better at high temperature versus being cooled to room temperature where reintroduction of moisture back into the matrix seems to produce further damage. The exact quantity of moisture and the time in which the moisture was able to migrate into each specimen is unknown.

The field work included the investigation of two furnace roof structures and a rotary kiln. The α-factor for the field work applications was produced using a stepwise solution based on the experimental results. The application of the α-factor prevented an underestimation of lining thickness in the cases where the wave speed increased and prevented an overestimation of lining thickness where the wave speed decreased. The stepwise correction factor allowed an assessment of the lining based on the depth of the detected flaw. The α-factor can be used in a multi-layer situation with each material layer having a unique factor. A more detailed discussion of the results is presented in Chapter 5.

Chapter 5
Conclusions and Recommendations

5.1 Discussion and Conclusions

The feasibility of using the acousto ultrasonic-echo technique for monitoring industrial furnaces was evaluated in this thesis. Limitations of other NDT techniques produce a demand for the development of more accurate methods. The electromagnetic (short-pulse radar, etc.) and magnetic (covermetre, etc.) techniques will not pass through the steel shell encasing the refractory lining of the furnace and are hence only useful when the vessel is offline, cooled and personal can utilize the measurements safely from inside of the vessel. Thermal evaluation is subject to large errors if a discontinuity such as a crack or an interface between bricks is present. In addition, a steady state condition must be present in order for certain relationships to be valid for analysis. Ultrasonic techniques are not suitable due to the comparatively high frequencies and narrow bandwidth used as compared to the AU-E technique. The high frequencies signals will not penetrate to an adequate enough depth needed in order to produce useful data. In addition, some ultrasonic techniques require two surfaces in order to transmit and receive a signal. Industrial furnaces yield an extremely large amount of interference or noise due to the high temperatures and the properties of moving metal.

Furnace failures can be catastrophic. The release of molten metal into the work environment can be extremely hazardous from high temperatures along with the gasses that are released. Lost production is commonly on the order of millions of dollars per day while a furnace is off-line. The AU-E technique proves to be the most suited technique for evaluations furnace structures due to the usable frequency of the technique and the temperature correction factor.

Various laboratory investigations were conducted for this project. The testing of newly manufactured bricks illustrated the degree of variability that can exist in a given the number of samples. The AU-E evaluation can provide quality control by identifying poor quality samples before they are put into service and allowed to fail. For field measurements using the AU-E technique an average value for the properties of the refractories is used.

The heat treatment of the various refractories provided a significant amount of information for refractory materials in general and on specific materials used for industrial applications. Multiple factors were the caused changes in the elasticity, strength, wave speed, etc. with increasing temperature. The porosity tended to be the most significant factor. The porosity changes were cause by differential thermal expansion coefficients causing micro-cracking or decohesion to occur. Abrupt mechano-physical changes were attributed to phase changes in the microstructure or recrystallization of the matrix. The softening mechanism, which is mainly due to thermal expansion, also had an impact. The thermal expansion therefore had two conflicting effects. The effect of separating particles locally competed with the packing of material on a larger scale. These effects would compete to either increase or decrease the mechanical properties of the material.

The AU-E signal attenuation increased as the temperature increased in general. This was due to the higher kinetic energy interfering with the stress wave transmission. An increase in micro-cracking tends to also increase the signal attenuation. The cooling rate after sintering tends to create characteristic properties of some refractory materials

Finite element modelling was used in order to quantify the non-linearity of a temperature gradient on temperature dependent thermal conductivity. The results of the model yielded only a slight non-linear temperature profile for a large change in thermal conductivity. Therefore with a lack of data, the assumption of a linear temperature gradient would not produce a significant error. The non-linearity of the temperature gradient is influenced more by contact resistance or by an abrupt change in thermal conductivity.

The effects of high temperature exposure on concrete specimens were investigated using the AU-E technique. In general, the residual properties such as dynamic elasticity, static elasticity, compressive strength, etc. decreased with an increase in exposure temperature. This was due to the liberation of chemically bound water from calcium hydroxide and calcium-silicate-hydrate as the exposure temperature increased. Concrete samples were also tested while at the actual exposure temperatures. The concrete performed better while at the exposure temperatures versus cooling back to room temperature where reintroduction of moisture into the matrix caused further

damage. This was only evident beyond exposure temperatures of 400°C where the onset of dehydration would commence within the calcium hydroxide. The wedge action of the water and the rehydration of dissociated calcium hydroxide produce an extremely large volume change destroying the weakened matrix. The water is reintroduced from the relative humidity in the air and does take time for the moisture to infiltrate into successive layers of the damaged concrete.

In this study, high strength concrete performed better than the normal strength concrete when exposed to high temperatures. The low heating rate allowed the high strength concrete to cope slightly better than if exposed to a high heating regime. Typically, high strength concrete exhibits explosive spalling when exposed to fire due to high vapour pressure build-up from the liberated water. To counteract this, fibres are added to provide an artificial pore system to aid in the release vapour. Polypropylene and steel fibres were added to the high strength concrete mixes in order to evaluate the effect of the fibre additions. The samples containing fibres did not exhibit any benefit due to the low heating rate used in this study. The metal fibres were actually detrimental by adding addition stress to the matrix due to oxidation after high temperature exposure. These specimens exhibited a higher degree of micro-cracking as indicated by the AU-E evaluation and would likely provide little benefit regarding vapour pressure release under a more rapid heating regime.

The experimental findings from the refractory heating trials using the AU-E technique were applied to three industrial applications. A temperature correction factor (α) for the AU-E P-wave speed versus depth was derived for specific temperature gradients. The actual depth of the crack or discontinuity was arrived at by a small number of iterations for each point evaluated by the AU-E technique. The evaluation of Furnace Roof #1 provided valuable information, which was used in a repair strategy during a shutdown. Areas of comparatively greater damage were targeted for repair while leaving comparatively less damaged areas for future repair campaigns. The added speed of the repair by identifying problem areas lowered the production losses.

The investigation of the rotary kiln provided an opportunity to confirm the AU-E signals with a covermetre after shutdown. Approximately 70% of the results matched within 15-mm with differences arising from crack interfaces and build-up adhesion. The

AU-E inspection was conducted while the kiln was in full operation from the outer surface and did not interrupt the production schedule. The build-up information provides process specialists with feedback, which can be applied to the process conditions to yield a greater output of the manufactured product.

Furnace Roof #2 roof provided an illustration of the multilayer considerations of the AU-E technique. The roof is subject to a large accumulation of build-up coupled with deterioration of the refractory lining can produce sever structural compromises. The α-factor in this case was very close to 1.0 due to the large amount of build-up interfering with the heat transfer. For this analysis, two frequencies were used from the AU-E signals to simultaneously provide refractory deterioration and build-up thickness.

The evolution of this study has produced a procedure for evaluating refractory linings in industrial furnaces. The following main points are outlined:

- Identify the refractory material used in the furnace lining.
- Evaluate samples of the refractory material using the AU-E technique at various temperatures in order to obtain behaviour at these temperatures.
- Evaluate the temperature gradient involved via thermocouples and control room processes.
- Produce α- factor versus depth relationship for the given temperature gradient.
- Survey the furnace using AU-E technique and analyse using the above information and multilayer considerations if necessary.

The information used in the evaluation is temperature dependent. Knowledge of the temperature gradient is crucial which is arrived at by heat transfer calculations. Using the AU-E technique to evaluate the condition of a furnace lining provides information regarding cracks or discontinuities, which provided information regarding contact resistance. Therefore, the techniques should be used hand-in-hand in an iterative process to converge on accurate results. If limited information is available, the AU-E technique should be used as apposed to heat transfer evaluation alone since the AU-E technique is less sensitive to errors in the temperature gradient.

5.2 Suggestions for Further Research

From the information provided in this study the following areas are suggested for future research:

- Hysteresis effects can alter the material properties of a refractory considerably. Efforts should be made to quantify the effect of heating rates and number of heating and cooling cycles on refractory and concrete materials regarding hysteresis. The AU-E technique would be the ideal tool for this study.
- The dynamic modeling of stress wave propagation using finite element methods could provide insight by creating models, which are difficult to duplicate in the laboratory.
- The areas of high temperature damage in concrete that can be investigated further are quantifying the effects of the heating rates on both high strength concrete and normal strength concrete. Here the benefits of polypropylene fibres would be more evident. In addition, %wt, fibre diameter and length could be studied in order to quantify the effects. The concrete specimens in this study were evaluated comparatively using the AU-E technique. Porosity testing was not performed on any of the samples. A large amount of data can be produced using porosity relationships (porosity vs. MOE, compressive strength, etc.) of concrete subjected to high temperatures.
- Finally, combination heat transfer/AU-E techniques can be used to attempt to quantify the contact resistance. The contact resistance is the source of the greatest error in heat transfer calculations when determining temperature gradients.

REFERENCES:

Abaqus User's Manual Volume I, version 6.4.1 (2004), Hibbitt, Karlsson & Sorensen, Inc., 1080 Main Street, Pawtucket, R.I. 02860-4847, USA, http://www.abaqus.com.

Achenbach, J. D., (1973), *"Wave Propagation In Elastic Solids"*, North-Holland Publishing Company.

Agosta, D.S., Hightower, J.E., Foster, K., Leisure, R.G. and Gavra, Z. (2002), *"Elastic Moduli of Polycrystalline ZrCo as a Function of Temperature"*, Journal of Alloys and Compounds, Volume 346, Issue 1-2, November, pp 1-5.

Aston, S.D., Challis, R.E. and Yiasemides, G.P. (2001), *"The Dependence of the Elastic Properties of Silica/Alumina Materials on the Conditions used for Firing"*, Journal of European Ceramic Society, Volume 22, Issue 7, July, pp1119-1127.

ASTM Designation C469-94, (1994), *"Standard Test Method for Static Modulus of Elasticity and Poisson's Ratio of Concrete in Compression"*, ASTM, West Conshohocken, PA.

Bayley, F. J., Owen, J. M and Turner, A. B., (1972), *"Heat Transfer"*, Nelson, London.

Bilodeau, A., Kodur, V.K.R. and Hoff, G.C., (2004), *"Optimization of the Type and Amount of Polypropylene Fibres for Preventing the Spalling of Light Weight Concrete Subjected to Hydrocarbon Fire"*, Cement and Concrete Research, Volume 26, Issue 2, February, pp163-174.

Boctor, S. A., Ryff, P. F., Hiscocks, P. D., Ghorab, M. T. and Holmes, M. R., (1997), *"Electrical Concepts and Applications"*, West Publishing Company.

Culfik, M.S. and Ozturan, T., (2002), *"Effect of Elevated Temperatures on the Residual Mechanical Properties of High Performance Mortar"*, Cement and Concrete Research, Volume 32, Issue 2, May, pp-809-816.

Cutard, T., Marzagui, H., Roosefield, M., Ouedraogo, E., Prompt, N. and Deteuf, C., (2004), *"Room Temperature Mechanical Behavior of Two Refractory Castables"*, Advances in Refractory Research for the Metalurgical Industries IV Fourth International Symposium, Hamilton.

Cutard, T., Marzagui, H., Fogaing, E., Huger, M., Gault, C., Prompt, N. and Deteuf, C., (2004), *"Microstructural Changes and High TemperatureMechanical Behaviour of an andelusite BasedLow Cement Refractory Castable"*, Advances in Refractory Research for the Metalurgical Industries IV Fourth International Symposium, Hamilton.

Daughton, D.R., MacDonald, J. and Mulders, N., (2003), *"Acoustic Properties of Silica Aerogels Between 400 mK and 400 K"*, Journal of Non-Crystalline Solids, Volume 319, Issue 3, May, pp297-303.

Davis, J. L., (1988), *"Wave Proagation In Solids and Fluids"*, Spinger-Verlag, N.Y.

Doyle, J. F., (1997), *"Wave Propagation In Structures"*, Spinger, N.Y.

Fraizier, E., Nadal, M.H. and Oltra, R., (2002), *"Evaluation of Viscoelastic Constants of Metalic Materials by Lazer-ultrasonics at Elevated Temperatures"*, Ultrasonics, Volume 40, Issue 1-8, May, pp543-547.

Gadaud, P. and Pautrot, S., (2002), *"Characterization of the Elasticity and Anelasticity of Bulk Glass by Dynamical Subresonant and Resonant Techniques"*, Journal of Non-Crystalline Solids, Volume 316, Issue 1, February, pp 146-152.

Gandhi, A.S. and Jayaram, V., (2002), *"Plastically Deforming Amorphous ZrO_2-$Al2O_3$"*, Acta Materials, Volume 51, Issue 6, April, pp 1641-1649.

Graff, K. F., (1991), *"Wave Motion In Elastic Solids"*, Dover Publications, N.Y.

Handoo, S.K., Agarwal, S. and Agarwal, S.K., (2002), *"Physicochemical, Mineralogical and Morphological Characteristics of Concrete Exposed to Elevated Temperatures"*, Cement and Concrete Research, Volume 32, Issue 7, July, pp 1009-1018.

Hemrick, J.G., Kistler, C.W., Wereszczak, A.A. and Feber, M.K., (2003), *"Thermal Conductivity of Alumina Measured with Three Techniques"*, Journal of Testing and Evaluation, Volume 31, Issue 5, September, pp 438-442.

Hernandez-Olivares, F. and Barluenga, G., (2003), *"Fire Performance of Recycled Rubber Filled High Strength Concrete"*, Cement and Concrete Research, Volume 34, Issue 1, January, pp 109-117.

Incropera, F. and DeWitt, D., (1990), *"Introduction to Heat Transfer"*, Wiley, NY

Kingery, W.D., Bowen, H.K. and Uhlmann, D.R., (1976), *"Introduction to Ceramics"*, John Wiley and Sons, NY

Kolsky, H., (1963), *"Stress Waves In Solids"*, Dover Publications, New York.

Libby, H. L., (1971), *"Introduction to Electromagnetic Nondestructive Test Methods"*, John Wiley & Sons Inc., New York.

Malhotra, V. M. and Carnio, N. J., (1991), *"CRC Handbook On Nondestructive Testing Of Concrete"*, Boca Raton, CRC Press.

Mindess, S., Young, J. F. and Darwin, D., (2003), *"Concrete"*, Prentice Hall. Upper Saddle River, NJ.

Pollard, H. F., (1977), *"Sound Waves In Solids"*, Pion Limited, London.

Roebben, G., Duan, R.G., Sciti, D. and Van der Biest, O., (2002), *"Assessment of the High Temperature Elastic and Damping Properties of Silicon Nitrides and Carbides with the Impulse Excitation Technique"*, Journal of European Ceramic Society, Volume 22, Issue14-15, pp 2501-2509.

Rouxel, T., Sangleboeuf, J.C., Huger, M., Gault, C., Besson, J.L. and Testu, S., (2001), *"Temperature Dependence of Young's Modulus in Si3N4 Based Ceramics: Roles of Sintering Additives and of SiC Particle Content"*, Acta Materials, Volume 50, Issue 7, April, pp 1669-1682

Sadri, A., (1996), *"Development of the MSR System for NDE of Concrete Shaft and Tunnel Linings"*,. PhD Thesis, Department of Mining and Metallurgical Engineering, M^{c}Gill University.

Sadri, A., (1997), *"Evaluation of Refractory Lining"*, Report, ANDEC International Services, Toronto.

Sansalone, M. J., and Streett, W. B., (1997), *"Impact Echo: Nondestructive Evaluation of Concrete and Masonry"*, Bullbrier Press, N.Y.

Serway, R. A., (1996), *"Physics For Scientists and Engineers"*, Saunders College Publishing, New York.

Tedesco, J. D., McDougal, W. G. and Ross, C. A., (1999), *"Structural Dynamics"*, Addison Wesley Longman Inc, Menlo Park, California.

Tessier-Doyen, N., Huger, M. and Glandus, J.C., (2004), *"Experimental Study of Elastic Behavior of Model Refractory Materials"*, Advances in Refractory Research for the Metalurgical Industries IV Fourth International Symposium, Hamilton.

Thomas, M.D.A., Tesfamariam, S. and Sadri, A., (1999), *"The Use of Stress Waves for Evaluating AAR Affected Concrete"*, Proceedings of Creating with Concrete, Ed. R.K. Dhir, Dundee, UK, September, pp 270.

Williams, P.J., Biernacki, J.J, Bai, J. and Rawn, C., (2003), *"Assessment of a Synchrotron X-Ray Method for Quantitative Analysis of Calcium Hydroxide"*, Cement and Concrete Research, Volume 33, Issue 10, October, pp 1553-1559

Xu, Y., Wong, Y.L., Poon, C.S. and Anson, M., (2001), *"Impact of High Temperature on PFA Concrete"*, Cement and Concrete Research, Volume 31, Issue 7, July, pp 1065-1073

Appendix - A

Sample Time And Frequency Domains

For Refractory Heating Trials

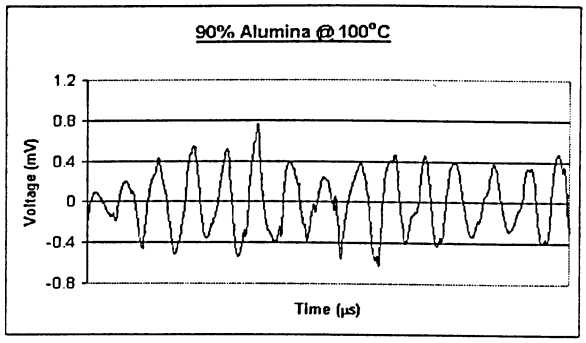
90% Alumina @ 100°C
1.2
0.8
0.4
0
-0.4
-0.8
Voltage (mV)
Time (μs)

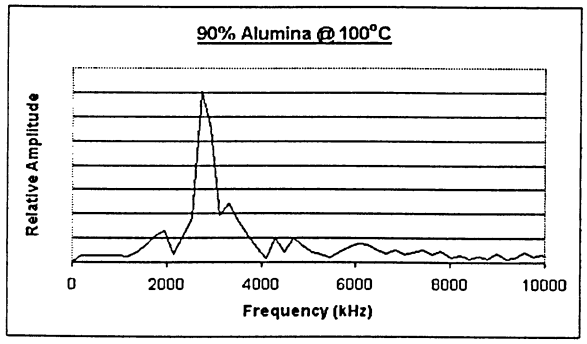
90% Alumina @ 100°C
Relative Amplitude
0
2000
4000
6000
8000
10000
Frequency (kHz)

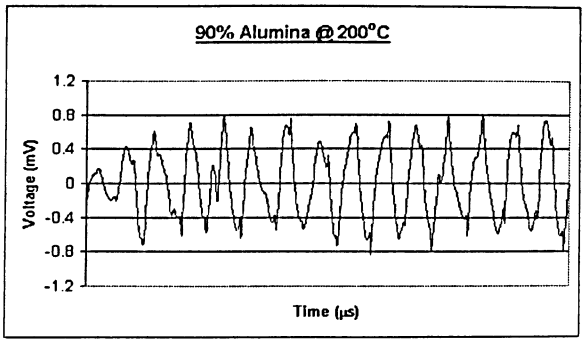
90% Alumina @ 200°C
1.2
0.8
0.4
0
-0.4
-0.8
-1.2
Voltage (mV)
Time (μs)

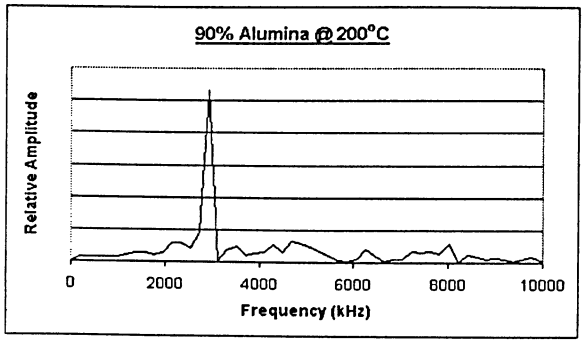
90% Alumina @ 200°C
Relative Amplitude
0
2000
4000
6000
8000
10000
Frequency (kHz)

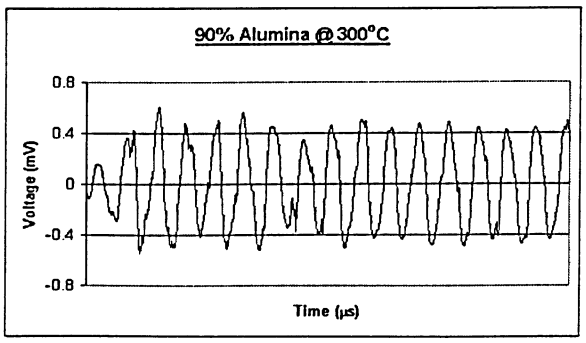
90% Alumina @ 300°C
0.8
0.4
0
-0.4
-0.8
Voltage (mV)
Time (μs)

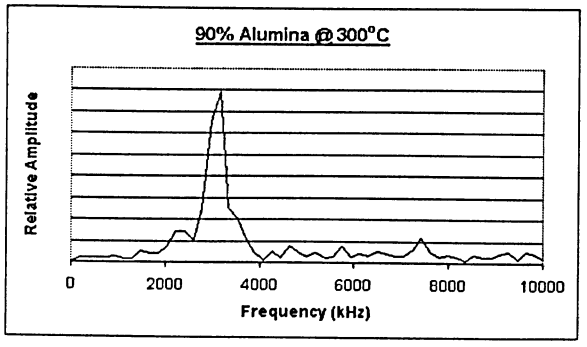
90% Alumina @ 300°C
Relative Amplitude
0
2000
4000
6000
8000
10000
Frequency (kHz)

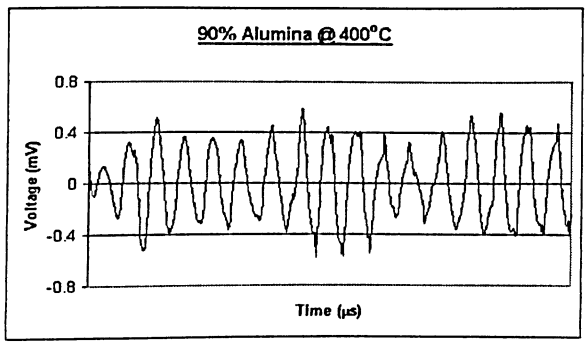
90% Alumina @ 400°C
0.8
0.4
0
-0.4
-0.8
Voltage (mV)
Time (μs)

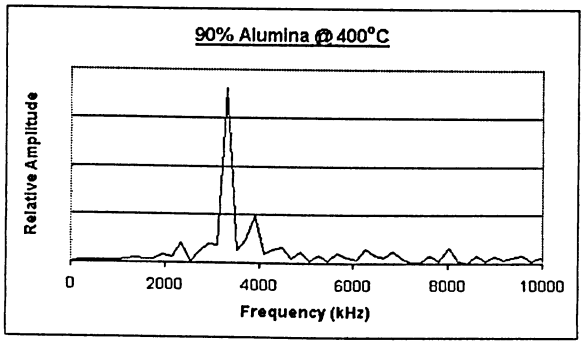
90% Alumina @ 400°C
Relative Amplitude
0
2000
4000
6000
8000
10000
Frequency (kHz)

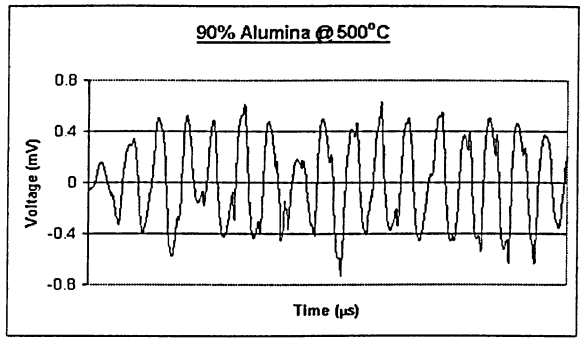
90% Alumina @ 500°C
0.8
0.4
0
-0.4
-0.8
Voltage (mV)
Time (μs)

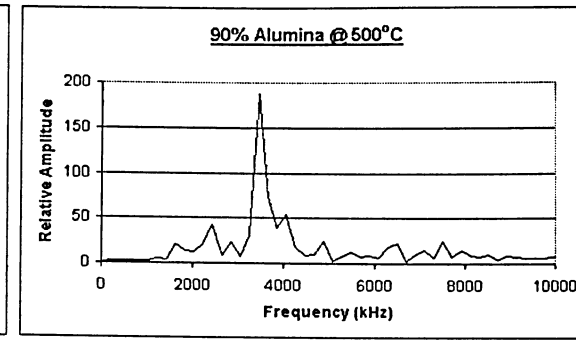
90% Alumina @ 500°C
200
150
100
50
0
Relative Amplitude
0
2000
4000
6000
8000
10000
Frequency (kHz)

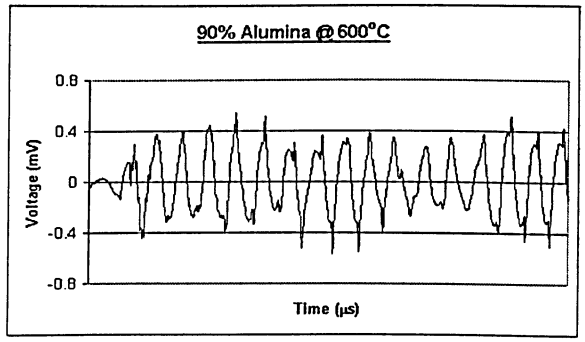
90% Alumina @ 600°C
0.8
0.4
0
-0.4
-0.8
Voltage (mV)
Time (μs)

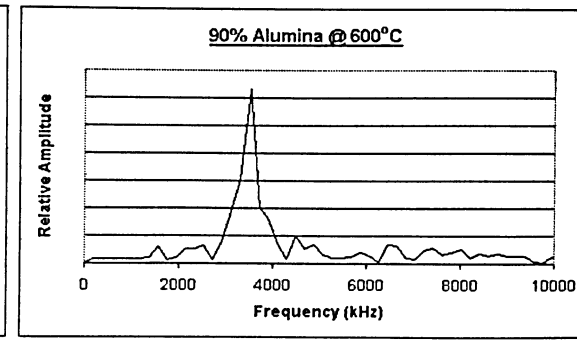
90% Alumina @ 600°C
Relative Amplitude
0
2000
4000
6000
8000
10000
Frequency (kHz)

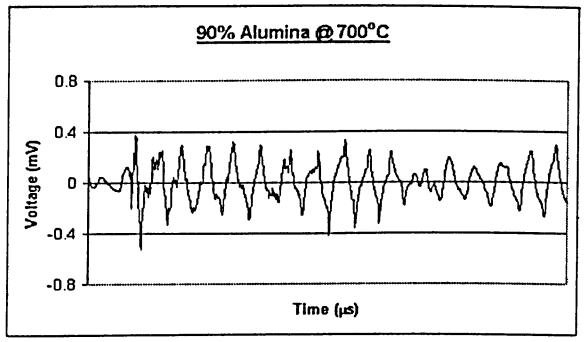
90% Alumina @ 700°C
0.8
0.4
0
-0.4
-0.8
Voltage (mV)
Time (μs)

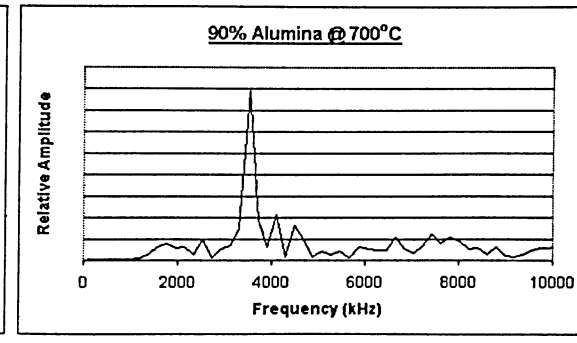
90% Alumina @ 700°C
Relative Amplitude
0
2000
4000
6000
8000
10000
Frequency (kHz)

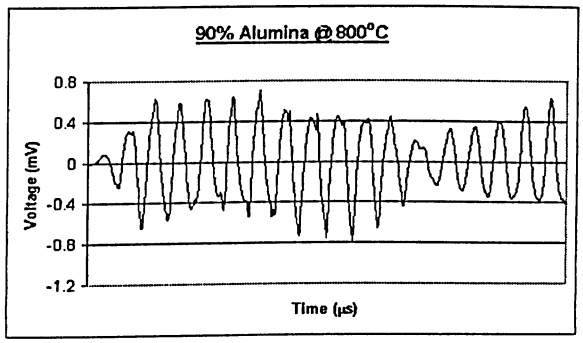
90% Alumina @ 800°C
0.8
0.4
0
-0.4
-0.8
-1.2
Voltage (mV)
Time (μs)

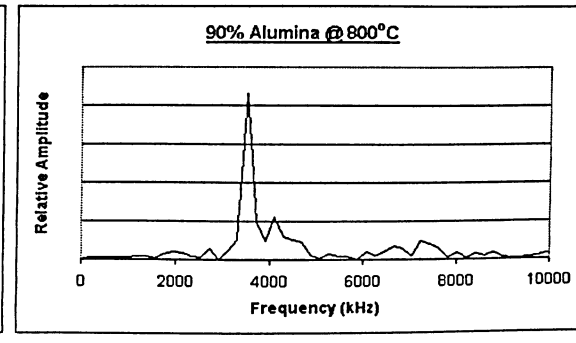
90% Alumina @ 800°C
Relative Amplitude
0
2000
4000
6000
8000
10000
Frequency (kHz)

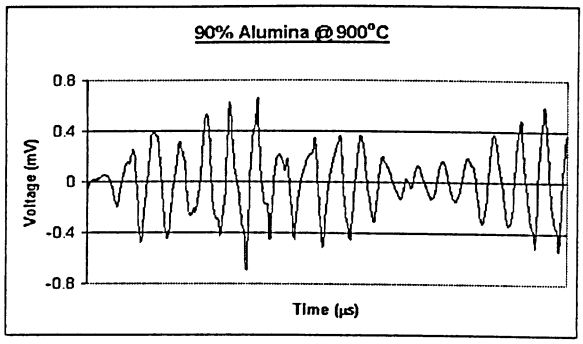
90% Alumina @ 900°C
0.8
0.4
0
-0.4
-0.8
Voltage (mV)
Time (μs)

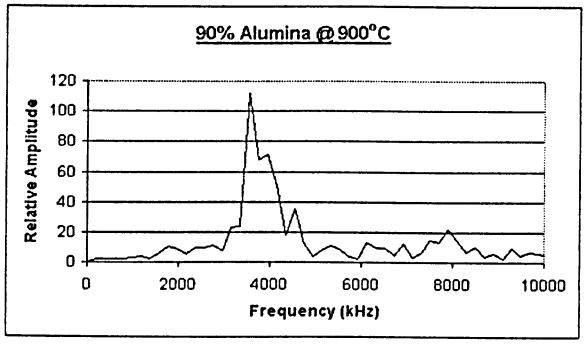
90% Alumina @ 900°C
120
100
80
60
40
20
0
Relative Amplitude
0
2000
4000
6000
8000
10000
Frequency (kHz)

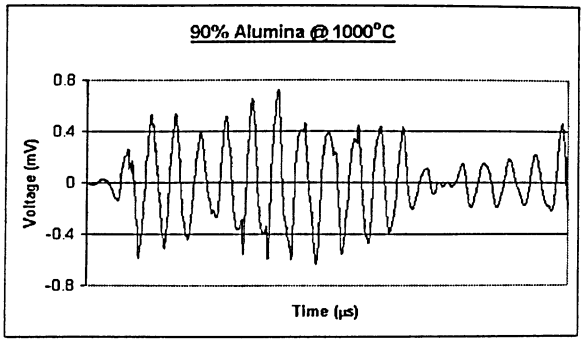
90% Alumina @ 1000°C
0.8
0.4
0
-0.4
-0.8
Voltage (mV)
Time (μs)

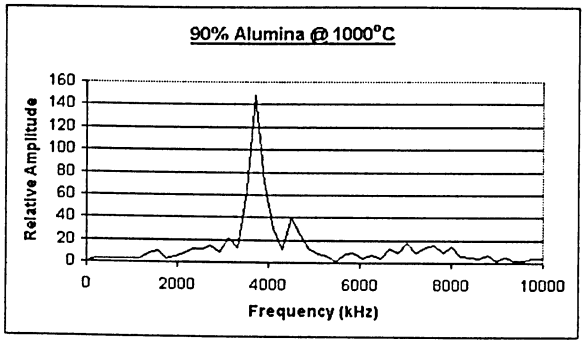
90% Alumina @ 1000°C
160
140
120
100
80
60
40
20
0
Relative Amplitude
0
2000
4000
6000
8000
10000
Frequency (kHz)

Appendix - B

Sample Stress-Strain Curves For Concrete Samples

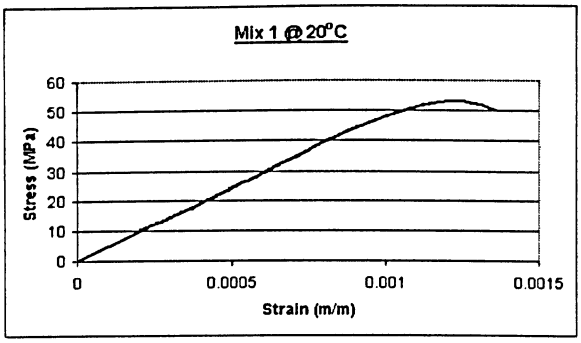
Mix 1 @ 20°C
Stress (MPa)
60
50
40
30
20
10
0
0
0.0005
0.001
0.0015
Strain (m/m)

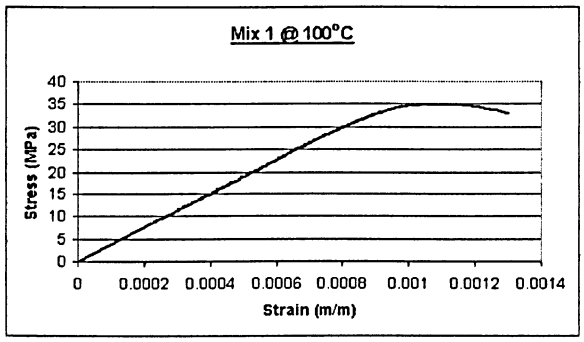
Mix 1 @ 100°C
Stress (MPa)
40
35
30
25
20
15
10
5
0
0
0.0002
0.0004
0.0006
0.0008
0.001
0.0012
0.0014
Strain (m/m)

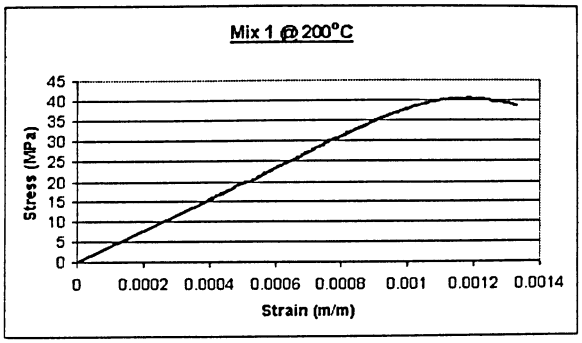
Mix 1 @ 200°C
Stress (MPa)
45
40
35
30
25
20
15
10
5
0
0
0.0002
0.0004
0.0006
0.0008
0.001
0.0012
0.0014
Strain (m/m)

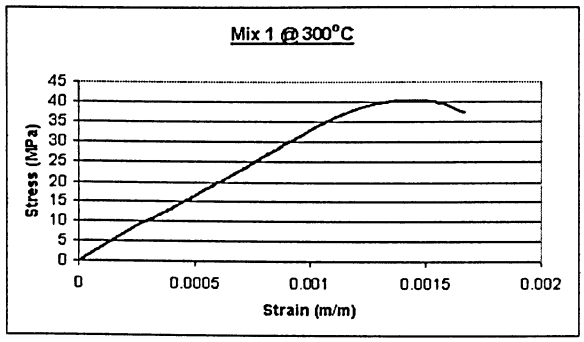
Mix 1 @ 300°C
Stress (MPa)
45
40
35
30
25
20
15
10
5
0
0
0.0005
0.001
0.0015
0.002
Strain (m/m)

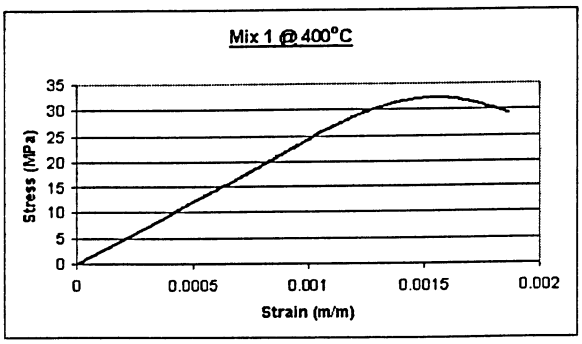
Mix 1 @ 400°C
Stress (MPa)
35
30
25
20
15
10
5
0
0
0.0005
0.001
0.0015
0.002
Strain (m/m)

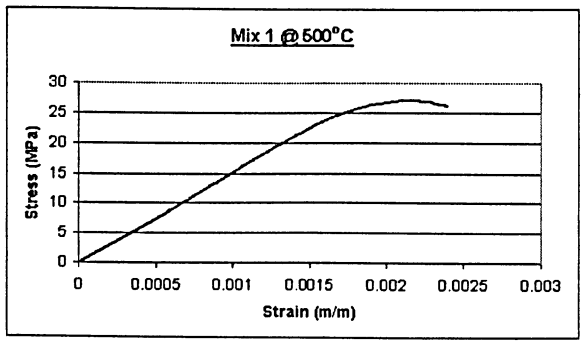
Mix 1 @ 500°C
Stress (MPa)
30
25
20
15
10
5
0
0
0.0005
0.001
0.0015
0.002
0.0025
0.003
Strain (m/m)

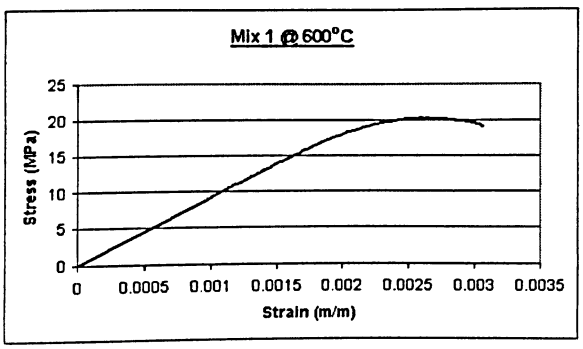
Mix 1 @ 600°C
Stress (MPa)
25
20
15
10
5
0
0
0.0005
0.001
0.0015
0.002
0.0025
0.003
0.0035
Strain (m/m)

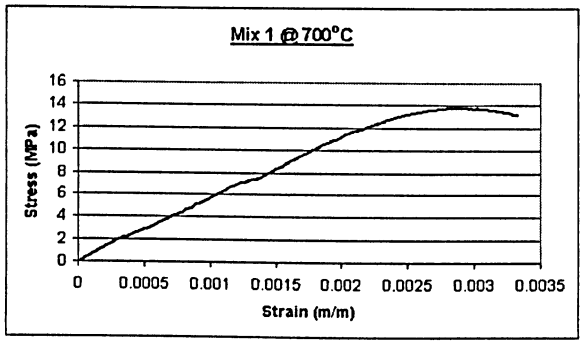
Mix 1 @ 700°C
Stress (MPa)
16
14
12
10
8
6
4
2
0
0
0.0005
0.001
0.0015
0.002
0.0025
0.003
0.0035
Strain (m/m)

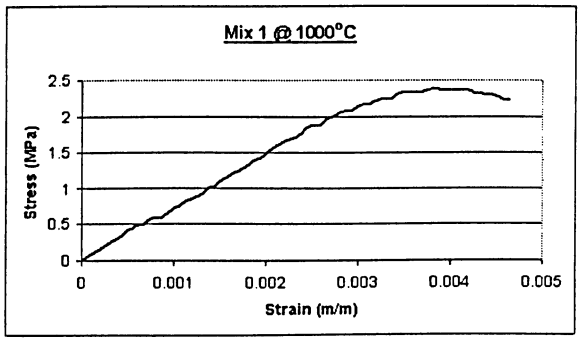
Mix 1 @ 1000°C
Stress (MPa)
2.5
2
1.5
1
0.5
0
0
0.001
0.002
0.003
0.004
0.005
Strain (m/m)

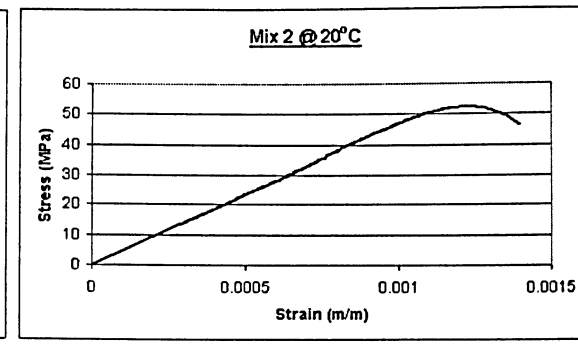
Mix 2 @ 20°C
Stress (MPa)
60
50
40
30
20
10
0
0
0.0005
0.001
0.0015
Strain (m/m)

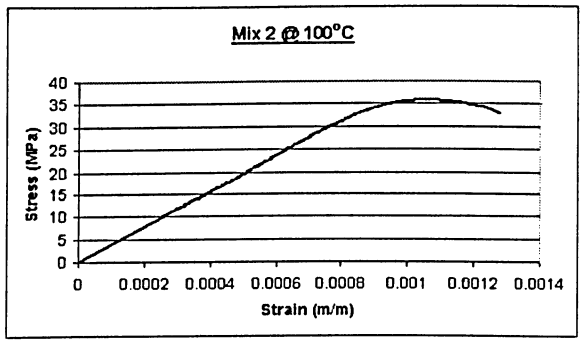
Mix 2 @ 100°C
Stress (MPa)
40
35
30
25
20
15
10
5
0
0
0.0002
0.0004
0.0006
0.0008
0.001
0.0012
0.0014
Strain (m/m)

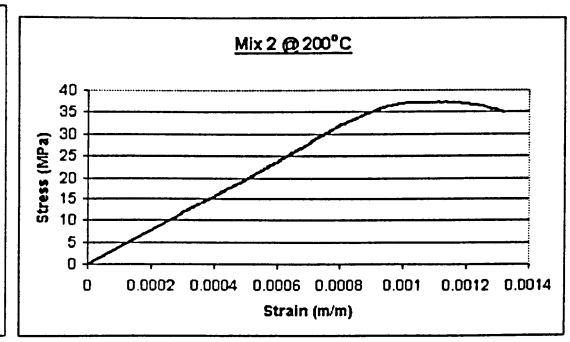
Mix 2 @ 200°C
Stress (MPa)
40
35
30
25
20
15
10
5
0
0
0.0002
0.0004
0.0006
0.0008
0.001
0.0012
0.0014
Strain (m/m)

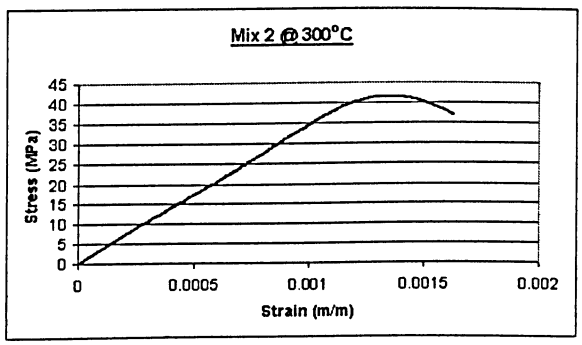
Mix 2 @ 300°C
Stress (MPa)
45
40
35
30
25
20
15
10
5
0
0
0.0005
0.001
0.0015
0.002
Strain (m/m)

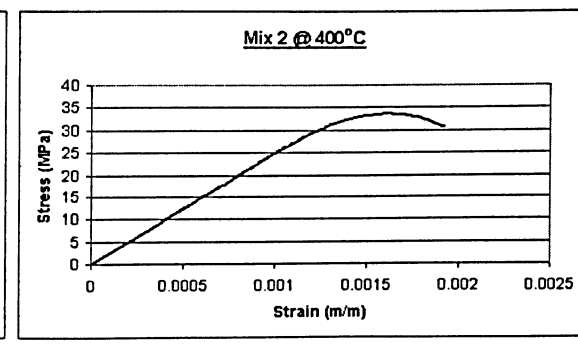
Mix 2 @ 400°C
Stress (MPa)
40
35
30
25
20
15
10
5
0
0
0.0005
0.001
0.0015
0.002
0.0025
Strain (m/m)

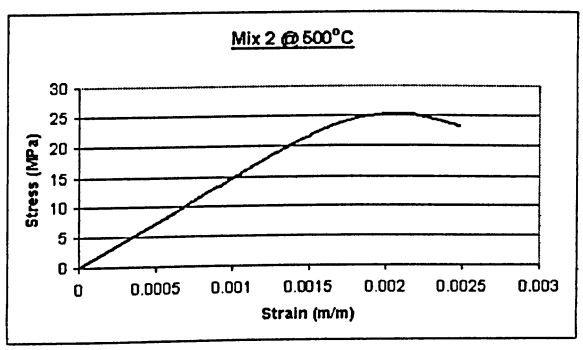
Mix 2 @ 500°C
Stress (MPa)
30
25
20
15
10
5
0
0
0.0005
0.001
0.0015
0.002
0.0025
0.003
Strain (m/m)

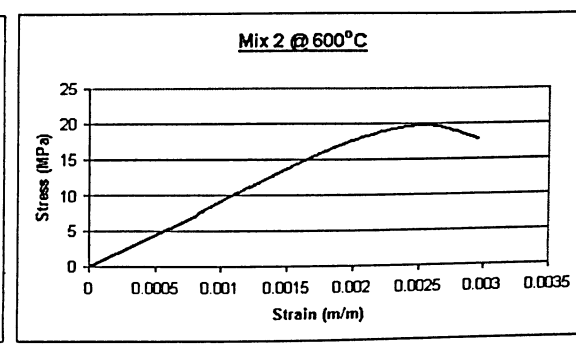
Mix 2 @ 600°C
Stress (MPa)
25
20
15
10
5
0
0
0.0005
0.001
0.0015
0.002
0.0025
0.003
0.0035
Strain (m/m)

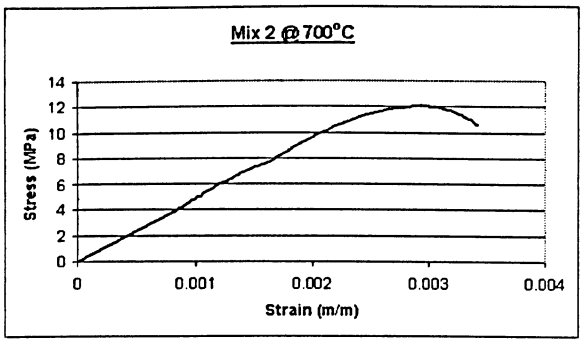
Mix 2 @ 700°C
Stress (MPa)
14
12
10
8
6
4
2
0
0
0.001
0.002
0.003
0.004
Strain (m/m)

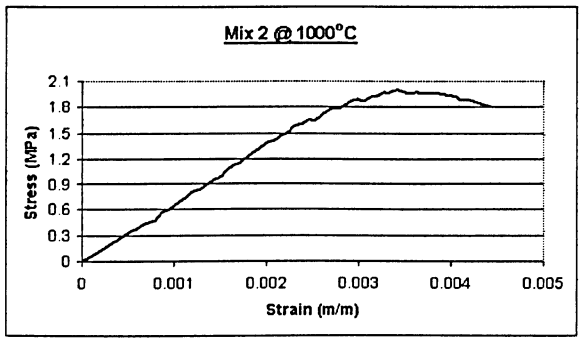
Mix 2 @ 1000°C
Stress (MPa)
2.1
1.8
1.5
1.2
0.9
0.6
0.3
0
0
0.001
0.002
0.003
0.004
0.005
Strain (m/m)

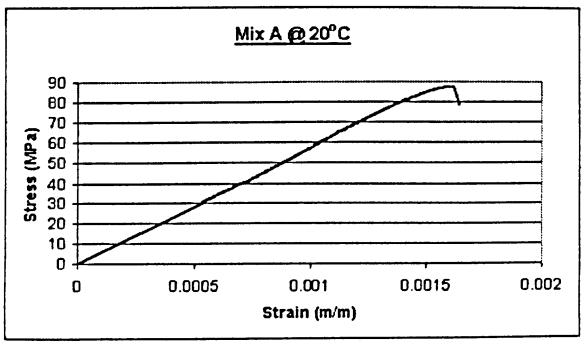
Mix A @ 20°C
Stress (MPa)
90
80
70
60
50
40
30
20
10
0
0
0.0005
0.001
0.0015
0.002
Strain (m/m)

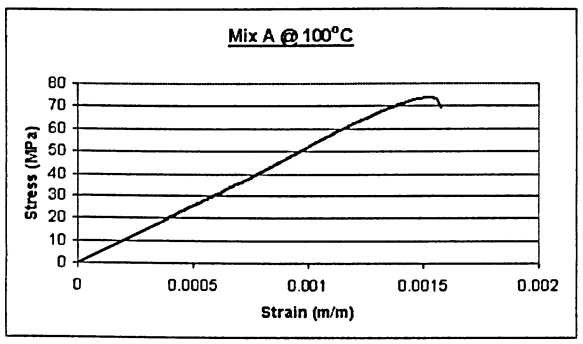
Mix A @ 100°C
Stress (MPa)
80
70
60
50
40
30
20
10
0
0
0.0005
0.001
0.0015
0.002
Strain (m/m)

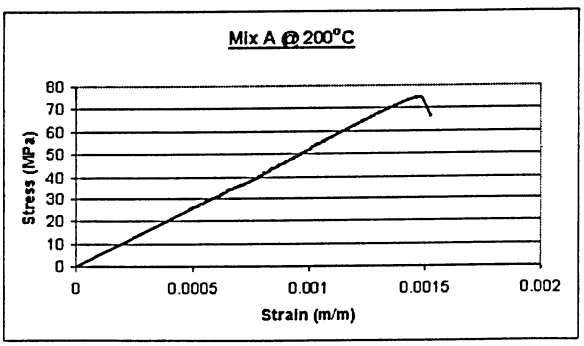
Mix A @ 200°C
Stress (MPa)
80
70
60
50
40
30
20
10
0
0
0.0005
0.001
0.0015
0.002
Strain (m/m)

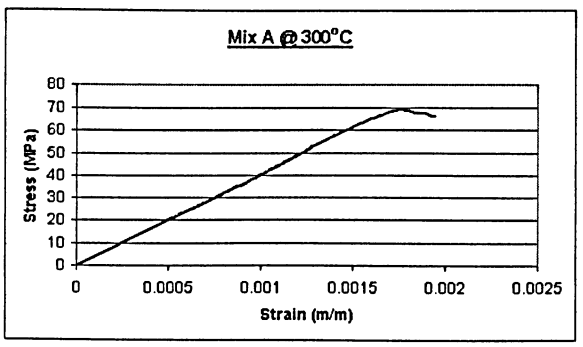
Mix A @ 300°C
Stress (MPa)
80
70
60
50
40
30
20
10
0
0
0.0005
0.001
0.0015
0.002
0.0025
Strain (m/m)

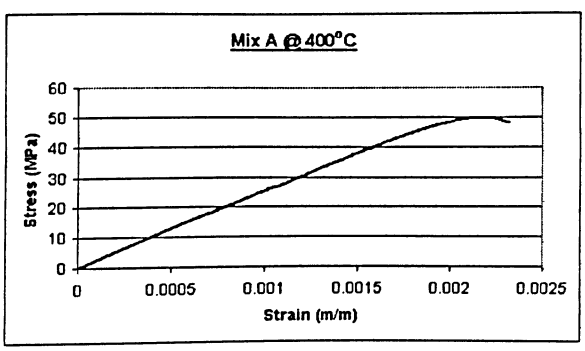
Mix A @ 400°C
Stress (MPa)
60
50
40
30
20
10
0
0
0.0005
0.001
0.0015
0.002
0.0025
Strain (m/m)

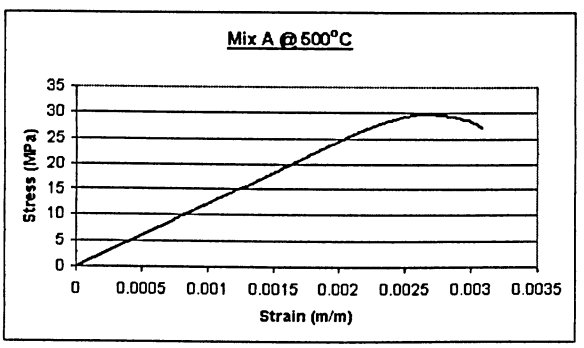
Mix A @ 500°C
Stress (MPa)
35
30
25
20
15
10
5
0
0
0.0005
0.001
0.0015
0.002
0.0025
0.003
0.0035
Strain (m/m)

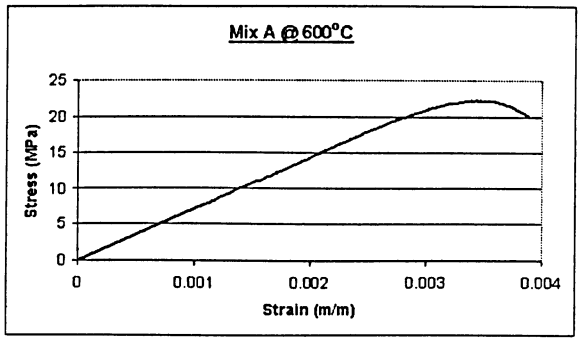
Mix A @ 600°C
Stress (MPa)
25
20
15
10
5
0
0
0.001
0.002
0.003
0.004
Strain (m/m)

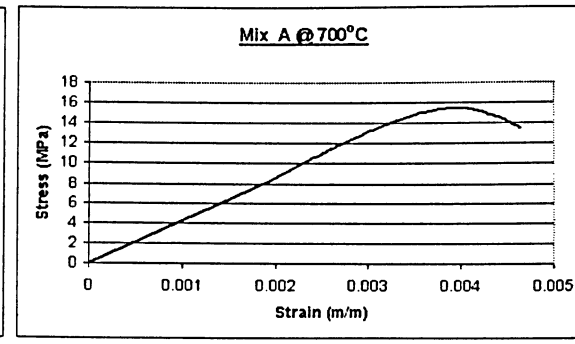
Mix A @ 700°C
Stress (MPa)
18
16
14
12
10
8
6
4
2
0
0
0.001
0.002
0.003
0.004
0.005
Strain (m/m)

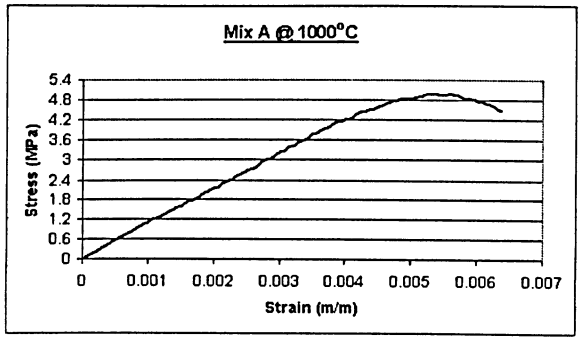
Mix A @ 1000°C
Stress (MPa)
5.4
4.8
4.2
3.6
3
2.4
1.8
1.2
0.6
0
0
0.001
0.002
0.003
0.004
0.005
0.006
0.007
Strain (m/m)

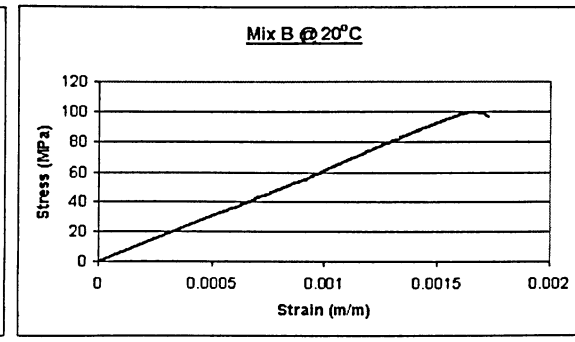
Mix B @ 20°C
Stress (MPa)
120
100
80
60
40
20
0
0
0.0005
0.001
0.0015
0.002
Strain (m/m)

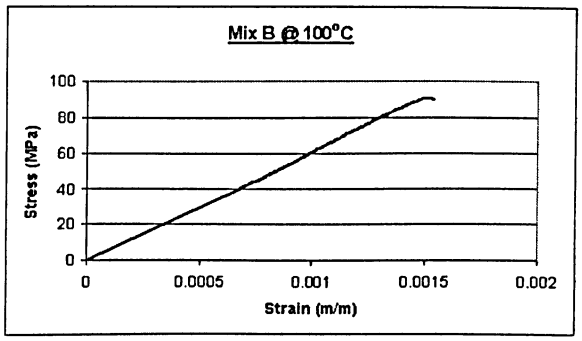
Mix B @ 100°C
Stress (MPa)
100
80
60
40
20
0
0
0.0005
0.001
0.0015
0.002
Strain (m/m)

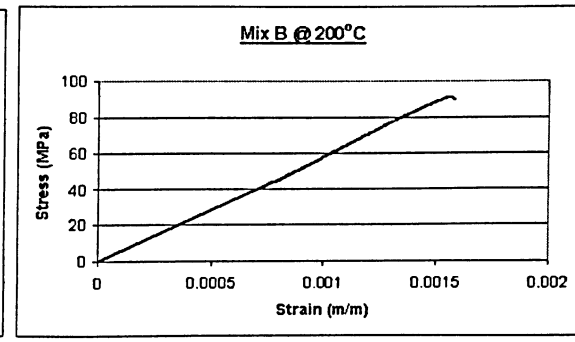
Mix B @ 200°C
Stress (MPa)
100
80
60
40
20
0
0
0.0005
0.001
0.0015
0.002
Strain (m/m)

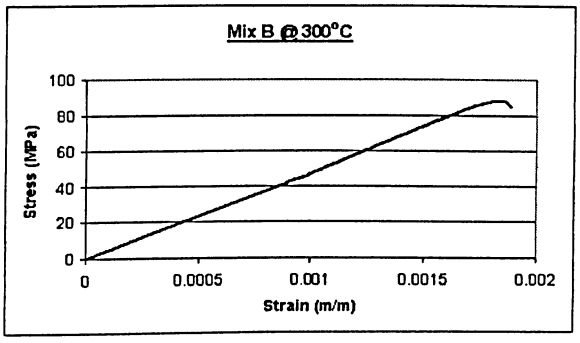
Mix B @ 300°C
Stress (MPa)
100
80
60
40
20
0
0
0.0005
0.001
0.0015
0.002
Strain (m/m)

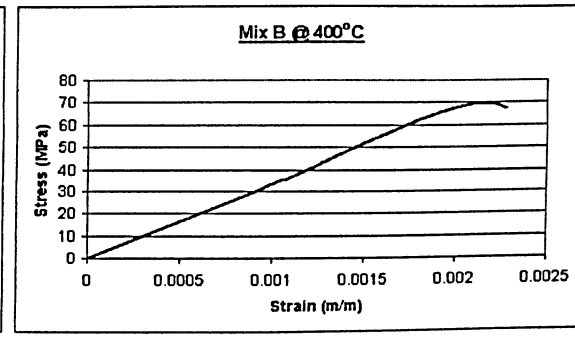
Mix B @ 400°C
Stress (MPa)
80
70
60
50
40
30
20
10
0
0
0.0005
0.001
0.0015
0.002
0.0025
Strain (m/m)

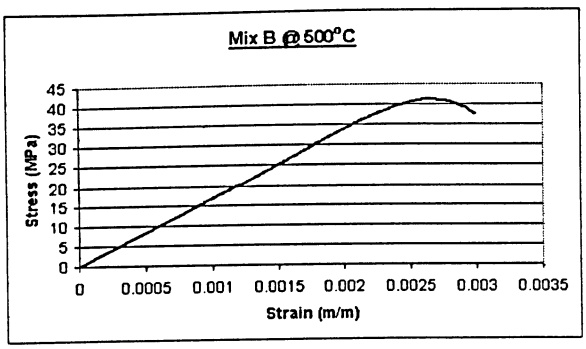
Mix B @ 500°C
Stress (MPa)
45
40
35
30
25
20
15
10
5
0
0
0.0005
0.001
0.0015
0.002
0.0025
0.003
0.0035
Strain (m/m)

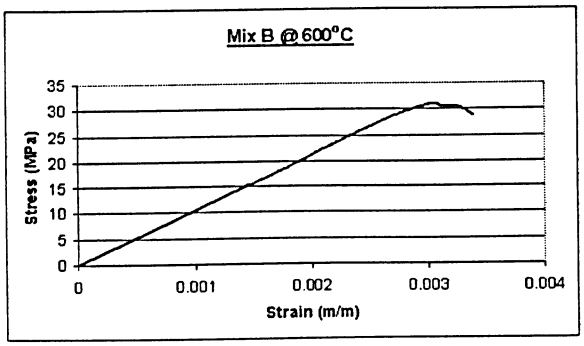
Mix B @ 600°C
Stress (MPa)
35
30
25
20
15
10
5
0
0
0.001
0.002
0.003
0.004
Strain (m/m)

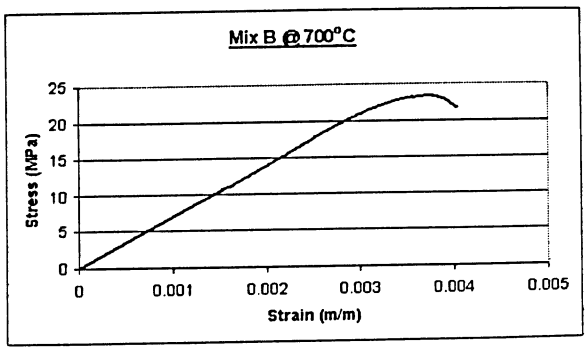
Mix B @ 700°C
Stress (MPa)
25
20
15
10
5
0
0
0.001
0.002
0.003
0.004
0.005
Strain (m/m)

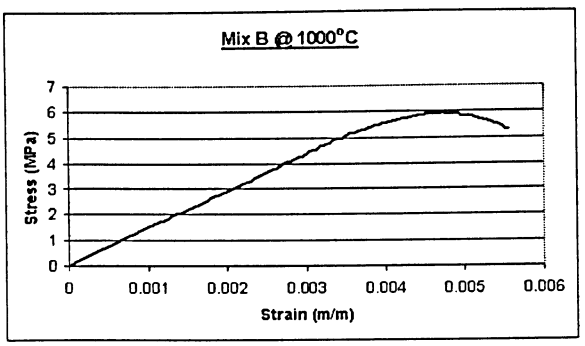
Mix B @ 1000°C
Stress (MPa)
7
6
5
4
3
2
1
0
0
0.001
0.002
0.003
0.004
0.005
0.006
Strain (m/m)

Appendix - C

Sample Time And Frequency Domains

For Concrete Heating

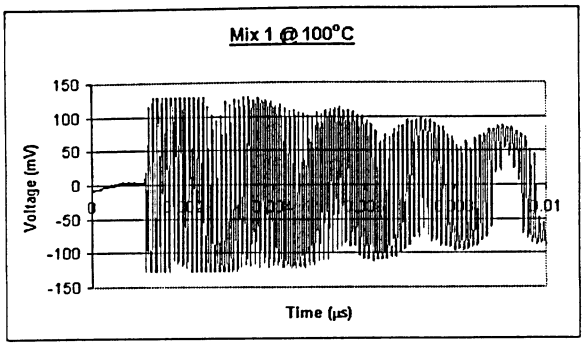
Mix 1 @ 100°C
Voltage (mV)
150
100
50
0
-50
-100
-150
0
0.01
Time (µs)

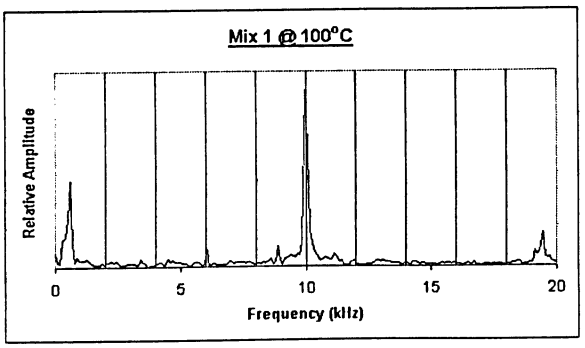
Mix 1 @ 100°C
Relative Amplitude
0
5
10
15
20
Frequency (kHz)

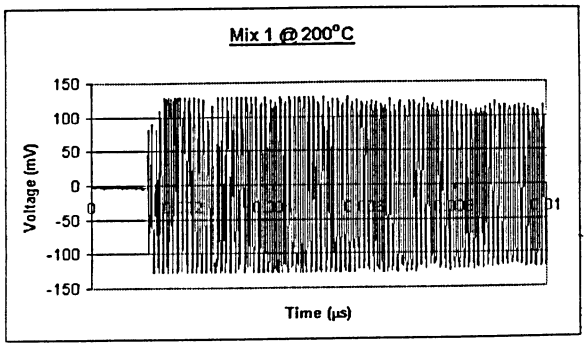
Mix 1 @ 200°C
Voltage (mV)
150
100
50
0
-50
-100
-150
0
0.01
Time (µs)

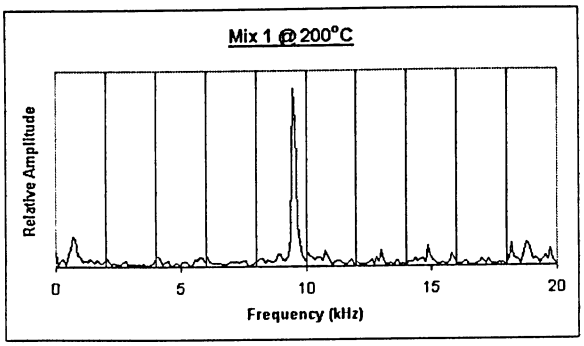
Mix 1 @ 200°C
Relative Amplitude
0
5
10
15
20
Frequency (kHz)

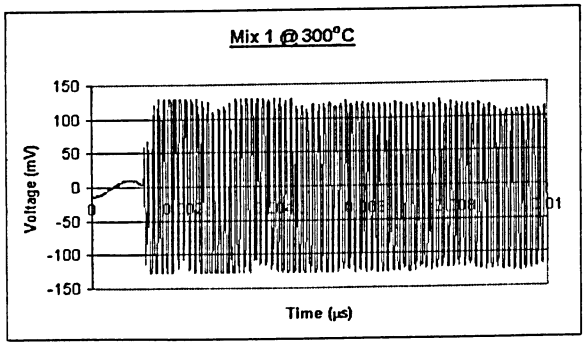
Mix 1 @ 300°C
Voltage (mV)
150
100
50
0
-50
-100
-150
0
0.01
Time (µs)

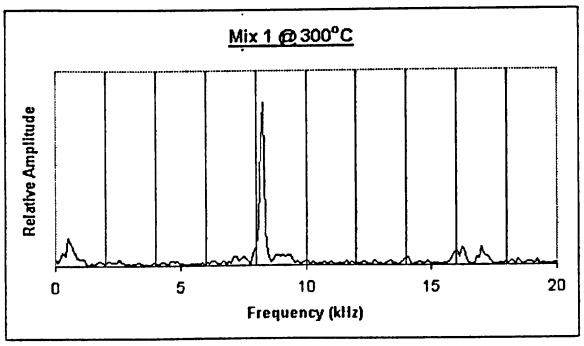
Mix 1 @ 300°C
Relative Amplitude
0
5
10
15
20
Frequency (kHz)

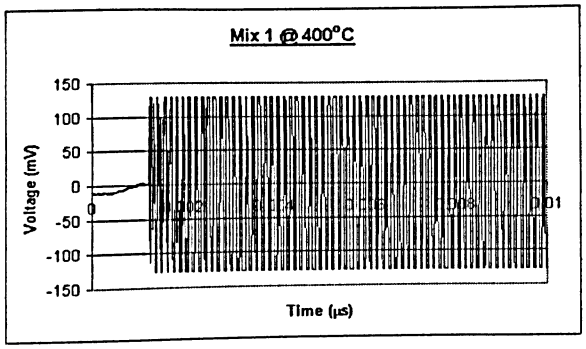
Mix 1 @ 400°C
Voltage (mV)
150
100
50
0
-50
-100
-150
0
0.01
Time (µs)

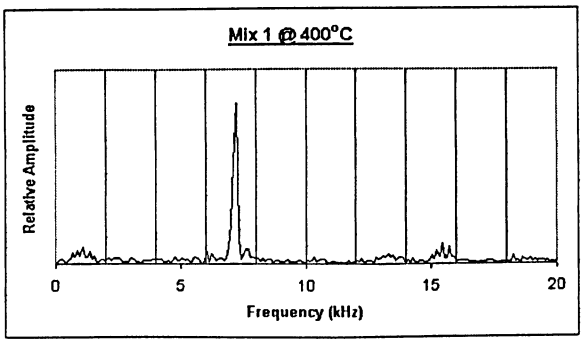
Mix 1 @ 400°C
Relative Amplitude
0
5
10
15
20
Frequency (kHz)

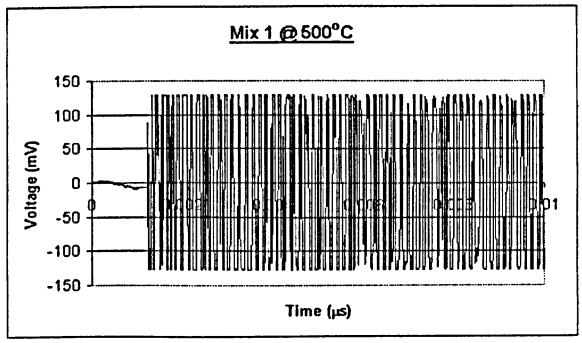
Mix 1 @ 500°C
Voltage (mV)
150
100
50
0
-50
-100
-150
0
0.01
Time (µs)

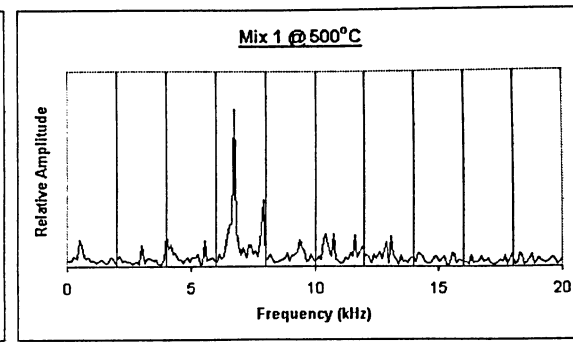
Mix 1 @ 500°C
Relative Amplitude
0
5
10
15
20
Frequency (kHz)

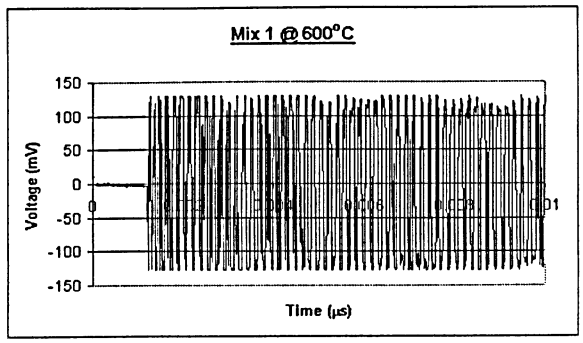
Mix 1 @ 600°C
Voltage (mV)
150
100
50
0
-50
-100
-150
0
0.01
Time (µs)

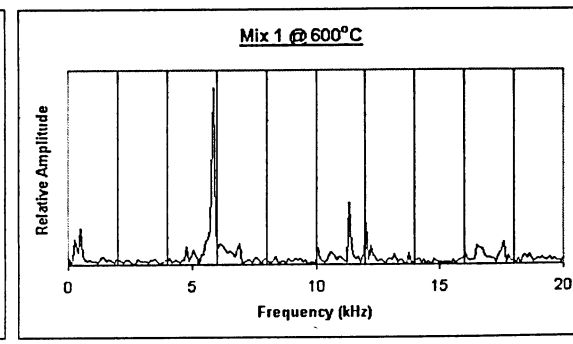
Mix 1 @ 600°C
Relative Amplitude
0
5
10
15
20
Frequency (kHz)

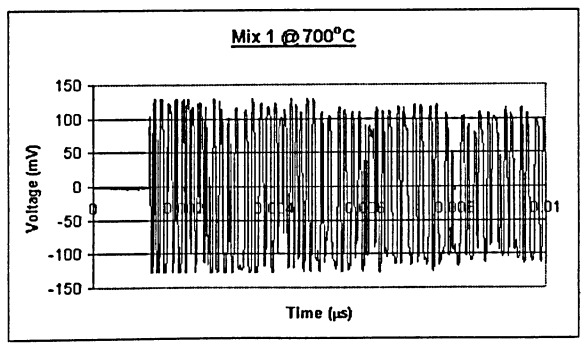
Mix 1 @ 700°C
Voltage (mV)
150
100
50
0
-50
-100
-150
0
0.01
Time (µs)

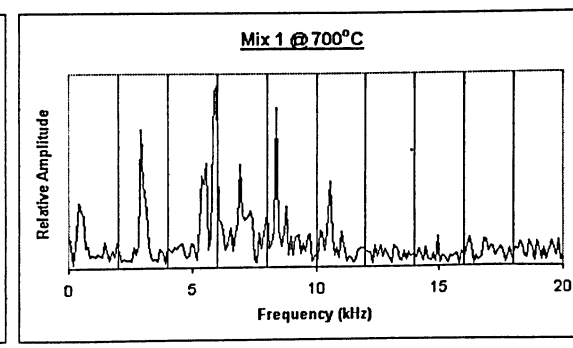
Mix 1 @ 700°C
Relative Amplitude
0
5
10
15
20
Frequency (kHz)

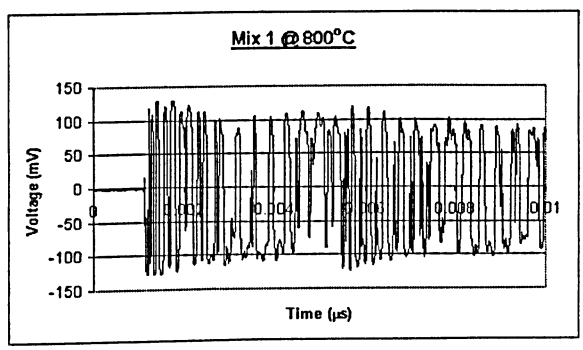
Mix 1 @ 800°C
Voltage (mV)
150
100
50
0
-50
-100
-150
0
0.01
Time (µs)

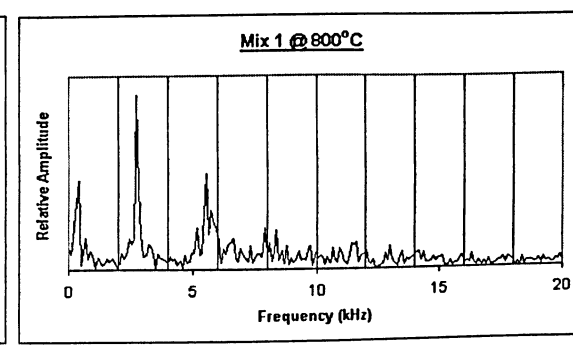
Mix 1 @ 800°C
Relative Amplitude
0
5
10
15
20
Frequency (kHz)

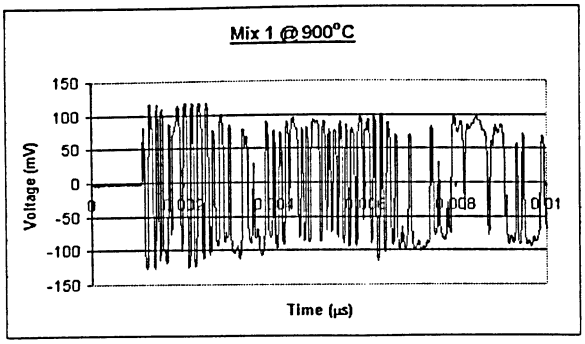
Mix 1 @ 900°C
Voltage (mV)
150
100
50
0
-50
-100
-150
0
0.002
0.004
0.006
0.008
0.01
Time (µs)

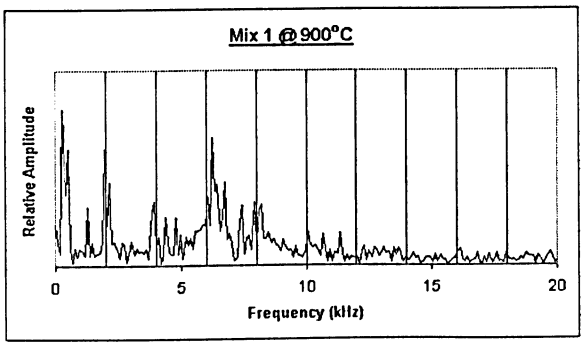
Mix 1 @ 900°C
Relative Amplitude
0
5
10
15
20
Frequency (kHz)

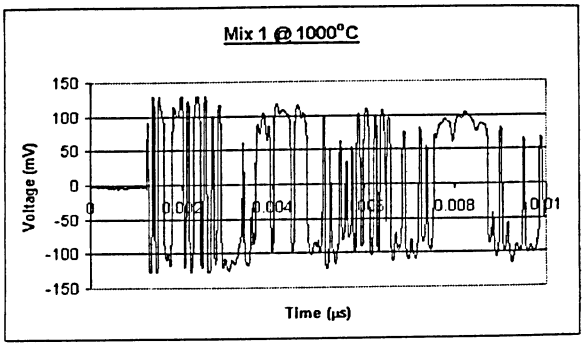
Mix 1 @ 1000°C
Voltage (mV)
150
100
50
0
-50
-100
-150
0
0.002
0.004
0.006
0.008
0.01
Time (µs)

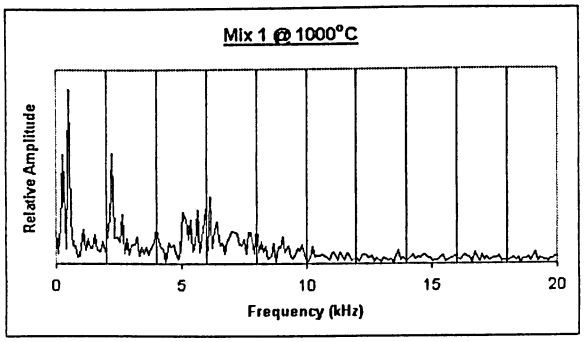
Mix 1 @ 1000°C
Relative Amplitude
0
5
10
15
20
Frequency (kHz)